

## PUBLISHER :



### Address of Publisher & Editor's Office :

GDAŃSK UNIVERSITY  
OF TECHNOLOGY

Faculty  
of Ocean Engineering  
& Ship Technology

ul. Narutowicza 11/12  
80-952 Gdańsk, POLAND  
tel.: +48 58 347 13 66  
fax : +48 58 341 13 66  
e-mail : office.pmr@pg.gda.pl

### Account number :

**BANK ZACHODNI WBK S.A.**  
I Oddział w Gdańsku  
41 1090 1098 0000 0000 0901 5569

### Editorial Staff :

**Tadeusz Borzęcki** Editor in Chief  
e-mail : tadb@pg.gda.pl

**Przemysław Wierzchowski** Scientific Editor  
e-mail : e.wierzchowski@chello.pl

**Jan Michalski** Editor for review matters  
e-mail : janmi@pg.gda.pl

**Aleksander Kniat** Editor for international relations  
e-mail : olek@pg.gda.pl

**Kazimierz Kempa** Technical Editor  
e-mail : kkempa@pg.gda.pl

**Piotr Bzura** Managing Editor  
e-mail : pbzura@pg.gda.pl

**Cezary Spigarski** Computer Design  
e-mail : biuro@oficynamorska.pl

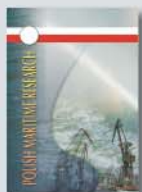
### Domestic price :

single issue : 20 zł

### Prices for abroad :

single issue :  
- in Europe EURO 15  
- overseas US\$ 20

ISSN 1233-2585



## POLISH MARITIME RESEARCH

*in internet*

[www.bg.pg.gda.pl/pmr/pmr.php](http://www.bg.pg.gda.pl/pmr/pmr.php)



## POLISH MARITIME RESEARCH

No 1(68) 2011 Vol 18

## CONTENTS

- 3 **ZYGMUNT PASZOTA**  
*Hydrostatic drives as safe and energy saving machines.  
The drive investigation method compatible with the diagram  
of power increase opposite to the direction of power flow*
- 10 **LAMAS M. I., RODRÍGUEZ J. D.,  
RODRÍGUEZ C. G., GONZÁLEZ P. B.**  
*Three-dimensional cfd analysis to study the thrust  
and efficiency of a biologically-inspired marine propulsor*
- 17 **HASSAN GHASSEMI, EHSAN YARI**  
*The Added Mass Coefficient Computation of sphere,  
ellipsoid and marine propellers  
using Boundary Element Method*
- 27 **PIOTR BZURA**  
*A method for evaluating durability of porous slide bearings*
- 32 **WOJCIECH LITWIN**  
*Influence of local bush wear on properties  
of water lubricated marine stern tube bearings*
- 37 **ANNA MAJCHRZYCKA**  
*Model of thermal comfort in the hyperbaric facility*

# Editorial

---

POLISH MARITIME RESEARCH is a scientific journal of worldwide circulation. The journal appears as a quarterly four times a year. The first issue of it was published in September 1994. Its main aim is to present original, innovative scientific ideas and Research & Development achievements in the field of :

## **Engineering, Computing & Technology, Mechanical Engineering,**

which could find applications in the broad domain of maritime economy. Hence there are published papers which concern methods of the designing, manufacturing and operating processes of such technical objects and devices as : ships, port equipment, ocean engineering units, underwater vehicles and equipment as well as harbour facilities, with accounting for marine environment protection.

The Editors of POLISH MARITIME RESEARCH make also efforts to present problems dealing with education of engineers and scientific and teaching personnel. As a rule, the basic papers are supplemented by information on conferences , important scientific events as well as cooperation in carrying out international scientific research projects.

## Scientific Board

---

Chairman : Prof. **JERZY GIRTLEK** - Gdańsk University of Technology, Poland

Vice-chairman : Prof. **ANTONI JANKOWSKI** - Institute of Aeronautics, Poland

Vice-chairman : Prof. **MIROSLAW L. WYSZYŃSKI** - University of Birmingham, United Kingdom

---

Dr **POUL ANDERSEN**  
Technical University  
of Denmark  
Denmark

Prof. **STANISŁAW GUCMA**  
Maritime University of Szczecin  
Poland

Dr **YOSHIO SATO**  
National Traffic Safety  
and Environment Laboratory  
Japan

Dr **MEHMET ATLAR**  
University of Newcastle  
United Kingdom

Prof. **ANTONI ISKRA**  
Poznań University  
of Technology  
Poland

Prof. **KLAUS SCHIER**  
University of Applied Sciences  
Germany

Prof. **GÖRAN BARK**  
Chalmers University  
of Technology  
Sweden

Prof. **JAN KICIŃSKI**  
Institute of Fluid-Flow Machinery  
of PASci  
Poland

Prof. **FREDERICK STERN**  
University of Iowa,  
IA, USA

Prof. **SERGEY BARSUKOV**  
Army Institute of Odessa  
Ukraine

Prof. **ZYGMUNT KITOWSKI**  
Naval University  
Poland

Prof. **JÓZEF SZALA**  
Bydgoszcz University  
of Technology and Agriculture  
Poland

Prof. **MUSTAFA BAYHAN**  
Süleyman Demirel University  
Turkey

Prof. **JAN KULCZYK**  
Wrocław University of Technology  
Poland

Prof. **TADEUSZ SZELANGIEWICZ**  
Technical University  
of Szczecin  
Poland

Prof. **MAREK DZIDA**  
Gdańsk University  
of Technology  
Poland

Prof. **NICOS LADOMMATOS**  
University College London  
United Kingdom

Prof. **WITALIJ SZCZAGIN**  
State Technical University  
of Kaliningrad  
Russia

Prof. **ODD M. FALTINSEN**  
Norwegian University  
of Science and Technology  
Norway

Prof. **JÓZEF LISOWSKI**  
Gdynia Maritime University  
Poland

Prof. **BORIS TIKHOMIROV**  
State Marine University  
of St. Petersburg  
Russia

Prof. **PATRICK V. FARRELL**  
University of Wisconsin  
Madison, WI  
USA

Prof. **JERZY MATUSIAK**  
Helsinki University  
of Technology  
Finland

Prof. **DRACOS VASSALOS**  
University of Glasgow  
and Strathclyde  
United Kingdom

Prof. **WOLFGANG FRICKE**  
Technical University  
Hamburg-Harburg  
Germany

Prof. **EUGEN NEGRUS**  
University of Bucharest  
Romania

Prof. **YASUHIKO OHTA**  
Nagoya Institute of Technology  
Japan

# Hydrostatic drives as safe and energy saving machines

## The drive investigation method compatible with the diagram of power increase opposite to the direction of power flow

Zygmunt Paszota, Prof.  
Gdansk University of Technology

### ABSTRACT



*Designers and manufacturers of hydrostatic drives have not a tool for precise determination of their energy efficiency, changing in a wide range in the driven device operating field, i.e. in the full range of the hydraulic motor speed and load and the working medium viscosity. This applies both to determining of losses and energy efficiency of displacement machines (pump and hydraulic motor) used in the drive system, and to losses and energy efficiency of the motor control system structure. A method is proposed compatible with the diagram of power increase opposite to the direction of power flow. That diagram replaces the Sankey diagram of power decrease in the direction of power flow.*

**Key words:** hydrostatic drive and control; evaluation of energy losses; method of the energy efficiency investigation; search for the energy saving solutions

### INTRODUCTION

Hydrostatic drive and control system have been in use for decades in ships and ocean technology objects, mainly because they are safe.

For instance, in tankers, because of the danger of explosion, the deck equipment – anchor windlass, automatic mooring winches etc. – are equipped with the hydrostatic drive. Cargo valves along the ship have hydrostatic remote control from the central console. The transport (impeller) pump system for oil unloading is often driven by displacement hydraulic motors submerged in the tanks.

In bulk carriers the hydrostatic drive is used for large hatch covers, deck cranes and other deck equipment.

Tankers and bulk carriers (and also other ships) have the hydrostatic drive and control systems for steering gear, bilge, ballast and fuel valves, cranes, hull opening covers and also the hydrostatic control of controllable pitch propellers in the ship main propulsion system.

In tankers and bulk carriers the central hydrostatic systems are used of simultaneous drive and control of many devices with total power of several megawatts.

A specific feature of the roll on – roll off ships are hydrostatically driven transport devices. A typical example is the stern ramp, 50 m long and 22 m wide close to the hull, and also internal ramps between decks.

In the container carriers a typical example are deck cranes with 450kN lift capacity and 30 m or more outreach, with separate hydrostatic drive in three independent closed circuits of hoisting, turning and change of outreach.

Fishing ships of up to 30 m in length are equipped with hydrostatically driven trawl, net and auxiliary winches. Multitask trawlers of up to 50 m in length, seiners up to 80 m long for catching fish in shoals in the ocean depth have hydrostatically driven winches; the hydrostatic drive is also used in cranes, auxiliary winches, hatch covers and other centrally controlled devices.

On the platforms, drilling, production and auxiliary ships, e.g. ocean tugs, the deck and technological equipment has most often the hydrostatic drive and control because of the danger of explosion.

However, the above given examples of the use of hydrostatic drive in floating units do not suggest that the hydrostatically driven ship and ocean object equipment will be dominating also in the future.

In 2006, the MacGREGOR company introduced, apart from deck cranes with hydrostatic drive, the first deck crane with electric drive [1]. In 2010 that company equipped only with 30t electric cranes 8 bulk carriers of 16 900 DWT capacity ordered in China by the Polish Polsteam owner [2]. The advantages, pointed out by the manufacturer, compared with hydrostatically driven cranes, are the following:

- faster and more precise positioning of the hook, reducing the loading time by 20% and shortening the port time,
- the drive power smaller by 30 ÷ 35%.

Also proposed is the use of electric drive and control of hatch covers in bulk carriers as well as full electric control of the ro – ro ship equipment.

The manufacturers of electrically driven ship equipment consider the energy efficiency of electric drive definitely higher than the hydrostatic drive efficiency.

The above quoted comparison of the installed power and energy efficiency of electric and hydrostatic drive is made in the situation when **designer of a hydrostatically driven device has no tool for precise determination of the drive energy efficiency** changing in a wide range in the driven device operating field. Therefore, there is no possibility of precise determining of the required power and in consequence of a reliable comparison of the two drives. This applies to the losses and energy efficiency of displacement machines (pump and hydraulic motor) used in the drive system and also to the energy efficiency of the whole system as a consequence of the used motor speed control structure.

In a hydrostatic drive system the mechanical energy is converted in the displacement pump into pressure energy of viscous fluid and the fluid pressure energy is converted into mechanical energy in the hydraulic motor. These two energy conversions in the displacement machines are connected with energy losses; the losses occur also in the conduits and in the motor speed throttling control assembly with a determined structure.

The only way is correct assessment of the level and proportion of energy losses, allowing also to search for energy saving solutions of the pump and motor as well as the whole hydrostatic drive system.

## **DETERMINING OF THE ENERGY LOSSES WITH THE ROTATIONAL HYDRAULIC MOTOR INVESTIGATION AS AN EXAMPLE**

The excerpts of the reference [19] will be quoted and supplemented in chapter 3 with significant findings.

Correct evaluation of the energy behaviour of a hydraulic motor is an evaluation of its overall efficiency  $\eta_M = f(n_M, M_M, \nu)$ , i.e. evaluation of the overall efficiency  $\eta_M$  as a function of the motor shaft speed  $n_M$  and load  $M_M$  and of the working fluid viscosity  $\nu$ . This is also assessment of the value and proportions of the motor mechanical, volumetric and pressure losses deciding of the motor mechanical  $\eta_{Mm}$ , volumetric  $\eta_{Mv}$  and pressure  $\eta_{Mp}$  efficiency, where the product  $\eta_M = \eta_{Mm} \eta_{Mv} \eta_{Mp}$  determines the motor overall efficiency  $\eta_M$ . The energy losses and the corresponding efficiencies  $\eta_{Mm}$ ,  $\eta_{Mv}$ , and  $\eta_{Mp}$  should be determined as a function of parameters having a direct impact on the particular losses and efficiencies.

However, designers and makers of rotational hydraulic motors and hydrostatic systems have not had so far a tool to determine their energy behaviour in the  $(0 \leq \bar{\omega}_M / \bar{\omega}_{Mmax}, 0 \leq \bar{M}_M / \bar{M}_{Mmax})$  field of change of the hydraulic motor shaft speed and load coefficients and in the  $v_{min} \leq \nu \leq v_{max}$  field of change of the hydraulic oil viscosity.

The rotational motor producers make erroneous routine evaluations of the following energy efficiencies and work parameters:

- the motor overall efficiency  $\eta_M$  as a function of the shaft speed  $n_M$  and motor pressure decrease  $\Delta p_M$  (e.g. [11 ÷ 14]),

- the motor overall efficiency  $\eta_M$  as a product of the volumetric efficiency  $\eta_{Mv}$  and the so called motor „mechanical – hydraulic efficiency”  $\eta_{Mmh}$ , all the three determined as a function of the same parameters (e.g. [11, 12]),
- motor shaft speed  $n_M$  as a function of the motor capacity  $Q_M$  and volumetric efficiency  $\eta_{Mv}$ , determined in turn as a function of the motor pressure decrease  $\Delta p_M$  (e.g. [11, 13]),
- motor shaft torque  $M_M$  as a function of pressure decrease  $\Delta p_M$  and the so called „mechanical – hydraulic efficiency”  $\eta_{Mmh}$  of the motor (e.g. [11 ÷ 14]),
- motor capacity  $Q_M$  as a function of the shaft speed  $n_M$  and volumetric efficiency  $\eta_{Mv}$ , determined in turn as a function of the motor pressure decrease  $\Delta p_M$  (e.g. [11 ÷ 13]),
- motor shaft useful power  $P_{Mu}$  as a function of the motor capacity  $Q_M$  and pressure decrease  $\Delta p_M$  and as a function of the motor overall efficiency  $\eta_M$  determined in turn as a function of the motor shaft speed  $n_M$  and pressure decrease  $\Delta p_M$  (e.g. [11 ÷ 13]).

The hydraulic motor researchers evaluate in a wrong way the losses arising in the motor:

- the motor torque  $M_{Mm}$  of mechanical losses as a function of the motor pressure decrease  $\Delta p_M$  and shaft speed  $n_M$ ,
- a sum of torque  $M_{Mm}$  of mechanical losses and the so called „torque of pressure losses” (resulting from the pressure losses  $\Delta p_{Mp}$  in the motor) – as a function of motor pressure decrease  $\Delta p_M$  and the shaft speed  $n_M$ ,
- the intensity  $Q_{Mv}$  of volumetric losses in the motor as a function of the motor pressure decrease  $\Delta p_M$  (or as a function of the motor shaft torque  $M_M$ ) and as a function of the motor shaft speed  $n_M$ .

**The evaluation methods of the energy losses and efficiency of the rotational hydraulic motors, used so far in the scientific research and in the industrial practice, give wrong results because the parameters that the losses and efficiencies are a function of are themselves dependent of those losses.**

There is very little information of the motor makers presenting properly the motor overall efficiency  $\eta_M = f(n_M, M_M)$  as a function of the motor shaft speed  $n_M$  and torque  $M_M$  at a specified fluid viscosity  $\nu$  and presenting the impact of viscosity  $\nu$  on the overall efficiency  $\eta_M$  (e.g. [10]).

It is a common deficiency that no information is given about the dependence of the motor mechanical, volumetric and pressure losses on the kinematic viscosity  $\nu$  of the working fluid used in the hydrostatic drive system.

The fundamental reason of the erroneous evaluations are commonly accepted views on the research methodology and on the method of determining the energy losses in pumps and in hydraulic motors. That method is based, among others, on the traditional reading of the energy balance of a hydrostatic drive system from the Sankey diagram [3 ÷ 9]. The present unsatisfactory state is also an effect of using simplified evaluations of the relations of particular losses to the motor or pump working parameters and to the working fluid viscosity.

In reference [19] the work parameters, power, losses and energy efficiencies in a rotational hydraulic motor are defined and described by means of 46 expressions and also their complex interrelations are shown.

The end formula (46) presents the motor efficiency  $\eta_M$  as a product of efficiencies described by means of losses and parameters deciding about those efficiencies, and the pressure decrease  $\Delta p_{Mi}$  indicated in the motor working chambers and capacity  $Q_M$  in the motor chambers are also functions of the losses:

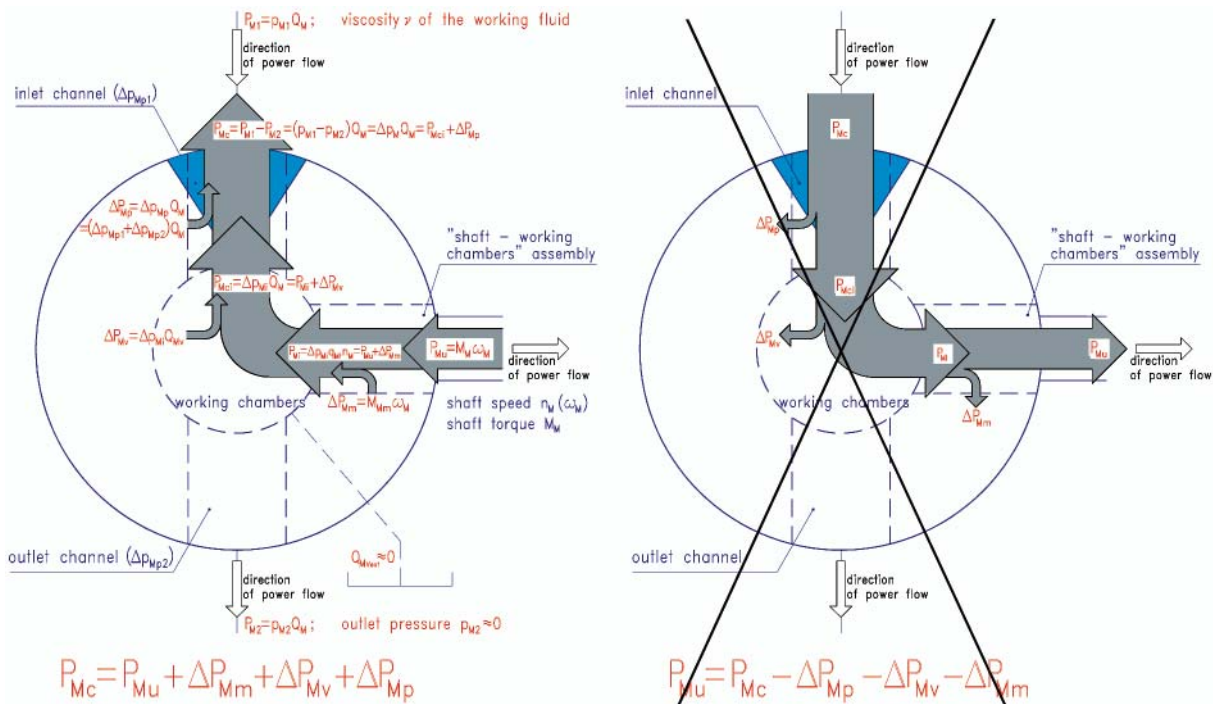


Fig. 1. Diagram of power increase in a hydraulic motor opposite to the direction of power flow, replacing the Sankey diagram of power decrease in the direction of power flow

$$\eta_M = f(M_M, n_M, v) = \eta_{Mm} \eta_{Mv} \eta_{Mp} = \frac{M_M}{M_M + M_{Mm}} \frac{q_{Mt} n_M}{q_{Mt} n_M + Q_{Mv}} \frac{\Delta p_{Mi}}{\Delta p_{Mi} + \Delta p_{Mp}} \quad (46)$$

where:

$$\begin{aligned} M_{Mm} &= f(M_M, n_M, v) \quad [\text{equation (2)}], \\ Q_{Mv} &= f(\Delta p_{Mi}, n_M, v) \quad [\text{equation (14)}], \\ \Delta p_{Mp} &= f(Q_M, v) \quad [\text{equation (25)}], \end{aligned}$$

with:

$$\Delta p_{Mi} = \frac{2\Pi(M_M + M_{Mm})}{q_{Mt}} \quad [\text{equation (6)}]$$

and

$$Q_M = q_{Mt} n_M + Q_{Mv} \quad [\text{equation (16)}].$$

Decrease  $\Delta p_{Mi}$  of pressure indicated in the working chambers (equation (6)) is a function of the loading torque  $M_M$  and torque  $M_{Mm}$  of mechanical losses in the „shaft – working chambers” assembly. Capacity  $Q_M$  in the motor channels (equation (16)) is a function of the motor shaft speed  $n_M$  and the intensity  $Q_{Mv}$  of volumetric losses in the working chambers.

## POWER IN THE DRIVE SYSTEM, LOSSES AND ENERGY EFFICIENCY, SYSTEM OPERATING FIELD

**Diagram of power increase in a power transmission system opposite to the direction of power flow replaces the Sankey diagram of power decrease in the direction of power flow.**

The Sankey diagram is the fundamental cause of incorrect evaluation of losses in a drive system.

The Sankey diagram connected with a drive system suggests an evaluation defining the output power of the system as

a difference between the system input power and sum of the powers of losses occurring in the system. Therefore the energy losses in the system are evaluated as a function of parameters describing the input power.

In accordance with the proposed diagram of power increase in a power transmission system opposite to the direction of power flow, **the system input power is a sum of the system output power and powers of losses occurring in the system. The energy losses in the system are evaluated as a function of parameters describing the system output power.**

Fig. 1 illustrates this principle by an example of power flow in a hydraulic motor.

The power  $P_{Mc}$  consumed by the hydraulic motor is a sum of motor shaft useful power  $P_{Mu}$  and powers of three different energy losses in the motor. The losses occur in series increasing power in the opposite direction to the direction of power flow. In effect, the power in the motor increases from the shaft useful power  $P_{Mu}$  to the working fluid power  $P_{Mc}$  consumed by the motor:

$$P_{Mc} = P_{Mu} + \Delta P_{Mm} + \Delta P_{Mv} + \Delta P_{Mp}$$

Mechanical losses (and power  $\Delta P_{Mm}$  of mechanical losses) occur in the „shaft – working chambers” assembly.

Volumetric losses (and power  $\Delta P_{Mv}$  of volumetric losses) occur in the working chambers.

Pressure losses (and power  $\Delta P_{Mp}$  of pressure losses) occur in the motor channels.

Formula (46) (equation (2)) shows a direct dependence of the torque  $M_{Mm}$  of mechanical losses in the „shaft – working chambers” assembly on the torque  $M_M$  and on the motor shaft rotational speed  $n_M$  as well as on the working fluid viscosity  $v$ .

Formula (46) (equations (14), (6)) presents a complex dependence of the intensity  $Q_{Mv}$  of volumetric losses in the working chambers on the shaft loading torque  $M_M$  and on the torque  $M_{Mm}$  of mechanical losses in the „shaft – working chambers” assembly (decrease  $\Delta p_{Mi}$  of pressure indicated in the working chambers depends on  $M_M$  and  $M_{Mm}$  and has direct impact on  $Q_{Mv}$ ) and also on the shaft speed  $n_M$  (influencing in a diversified way the torque  $M_{Mm}$  of mechanical losses (2) and

intensity  $Q_{Mv}$  of volumetric losses (14)). The intensity  $Q_{Mv}$  of volumetric losses depends on a diversified impact of the working fluid viscosity  $v$ : indirectly by impact of  $v$  on the torque  $M_{Mm}$  of mechanical losses in the „shaft – working chambers” assembly (2) and directly by impact of  $v$  on the intensity  $Q_{Mv}$  of losses in the working chambers (14).

Formula (46) (equations (25, 16, 14, 6)) presents also a complex dependence of losses  $\Delta p_{Mp}$  of pressure in the motor channels on the motor shaft rotational speed  $n_M$  and on intensity  $Q_{Mv}$  of volumetric losses in the motor working chambers. The intensity  $Q_{Mv}$  of volumetric losses influences the motor capacity  $Q_M$  (equation (16)) and at the same time  $Q_{Mv}$  depends in a complex way on the shaft loading torque  $M_M$  and on the torque  $M_{Mm}$  of mechanical losses in the motor „shaft – working chambers” assembly. Pressure losses  $\Delta p_{Mp}$  in the motor channels are also dependent on the diversified impact of the working fluid viscosity  $v$ : indirectly by impact of  $v$  on the torque  $M_{Mm}$  of mechanical losses in the „shaft – working chambers” assembly (2) and by impact of  $v$  on the intensity  $Q_{Mv}$  of volumetric losses in the working chambers (14) and directly by impact of  $v$  on the losses  $\Delta p_{Mp}$  of pressure in the channels (25).

Contrary to the commonly used, both by manufacturers and researchers, methods of evaluation of the hydraulic motor losses, it is unacceptable to create a „sum” of the torque  $M_{Mm}$  of mechanical losses in the „shaft – working chambers” assembly and the „torque” of pressure losses  $\Delta p_{Mp}$  in the motor channels, and also such a „sum” must not be evaluated as directly dependent on the same chosen parameters, because those losses are of different character and depend on different parameters:

$$M_{Mm} = f(M_M, n_M, v)$$

$$\Delta p_{Mp} = f(Q_M, v)$$

**The impact of hydraulic oil viscosity  $v$  on the energy losses in a hydraulic motor, i.e. on:**

- torque  $M_{Mm}$  of mechanical losses in a „shaft – working chambers” assembly,
- intensity  $Q_{Mv}$  of volumetric losses in the working chambers,
- pressure losses  $\Delta p_{Mp}$  in the conduits, is diversified.

Dependence of the motor losses on the hydraulic oil viscosity  $v$  should be presented in expressions describing also the dependence of those losses on other parameters which influence them directly:

$$M_{Mm} = f(M_M, n_M, v)$$

$$Q_{Mv} = f(\Delta p_{Mi}, n_M, v)$$

$$\Delta p_{Mp} = f(Q_M, v)$$

**The motor overall efficiency  $\eta_M$** , as a function of  $M_M$ ,  $n_M$  and  $v$ , is a product of  $\eta_{Mm}$ ,  $\eta_{Mv}$  and  $\eta_{Mp}$  efficiencies:

$$\eta_M = f(M_M, n_M, v) =$$

$$= \frac{P_{Mu}}{P_{Mc}} = \frac{M_M \omega_M}{\Delta p_M Q_M} = \frac{2\Pi M_M n_M}{\Delta p_M Q_M} = \eta_{Mm} \eta_{Mv} \eta_{Mp}$$

where:

- $P_{Mu}$  – the motor useful power,
- $P_{Mc}$  – the motor consumed power.

Each of the three efficiencies as a factor in the product describing the overall efficiency, is evaluated as a function

of parameters directly influencing the respective losses and a function of parameter to which the losses are „added”:

– **motor mechanical efficiency  $\eta_{Mm}$** :

$$\eta_{Mm} = \frac{P_{Mu}}{P_{Mi}} = \frac{M_M \omega_M}{(M_M + M_{Mm}) \omega_M} =$$

$$= \frac{2\Pi M_M n_M}{2\Pi (M_M + M_{Mm}) n_M} = \frac{M_M}{M_M + M_{Mm}} = f(M_M, n_M, v)$$

where:

$P_{Mi}$  – the power indicated in the motor working chambers:

$$P_{Mi} = \Delta p_{Mi} q_{Mt} n_{Mt} =$$

$$= (M_M + M_{Mm}) \omega_M = 2\Pi (M_M + M_{Mm}) n_M$$

– **motor volumetric efficiency  $\eta_{Mv}$** :

$$\eta_{Mv} = \frac{P_{Mi}}{P_{Mci}} = \frac{\Delta p_{Mi} q_{Mt} n_M}{\Delta p_{Mi} (q_{Mt} n_M + Q_{Mv})} = \frac{\Delta p_{Mi} q_{Mt} n_M}{\Delta p_{Mi} Q_M} =$$

$$= \frac{q_{Mt} n_M}{q_{Mt} n_M + Q_{Mv}} = \frac{q_{Mt} n_M}{Q_M} = f(\Delta p_{Mi}, n_M, v)$$

where

$P_{Mci}$  – the power consumed in the motor working chambers:

$$P_{Mci} = \Delta p_{Mi} (q_{Mt} n_M + Q_{Mv}) = \Delta p_{Mi} Q_M$$

– **motor pressure efficiency  $\eta_{Mp}$** :

$$\eta_{Mp} = \frac{P_{Mci}}{P_{Mc}} = \frac{\Delta p_{Mi} (q_{Mt} n_M + Q_{Mv})}{(\Delta p_{Mi} + \Delta p_{Mp}) (q_{Mt} n_M + Q_{Mv})} = \frac{\Delta p_{Mi} Q_M}{\Delta p_M Q_M} =$$

$$= \frac{\Delta p_{Mi}}{\Delta p_{Mi} + \Delta p_{Mp}} = \frac{\Delta p_{Mi}}{\Delta p_M} = f(\Delta p_{Mi}, Q_M, v)$$

In order to present the motor volumetric efficiency  $\eta_{Mv}$  as a factor in the  $\eta_{Mm} \eta_{Mv} \eta_{Mp}$  product describing  $\eta_M$ , i.e. to present  $\eta_{Mv}$  as a complex dependence on the  $(M_M, n_M, v)$  parameters describing  $\eta_M$  and dependent on the mechanical losses, the intensity  $Q_{Mv} = f(\Delta p_{Mi}, n_M, v)$  of volumetric losses in the working chambers should be determined with:

$$\Delta p_{Mi} = \frac{2\Pi (M_M + M_{Mm})}{q_{Mt}}$$

and with torque  $M_{Mm}$  of mechanical losses in the „shaft – working chambers” assembly as an  $M_{Mm} = f(M_M, n_M, v)$  function.

In order to present the motor pressure efficiency  $\eta_{Mp}$  as a factor in the  $\eta_{Mm} \eta_{Mv} \eta_{Mp}$  product describing  $\eta_M$ , i.e. to present  $\eta_{Mp}$  as a complex dependence on the  $(M_M, n_M, v)$  parameters describing  $\eta_M$  and dependent on the mechanical and volumetric losses in the motor, the pressure losses  $\Delta p_{Mp} = f(Q_M, v)$  in the channels must be determined with:

$$Q_M = q_{Mt} n_M + Q_{Mv}$$

then intensity  $Q_{Mv} = f(\Delta p_{Mi}, n_M, v)$  of volumetric losses in the working chambers must be determined with:

$$\Delta p_{Mi} = \frac{2\Pi (M_M + M_{Mm})}{q_{Mt}}$$

and the torque  $M_{Mm}$  of mechanical losses in the „shaft – working chambers” assembly must be determined as an  $M_{Mm} = f(M_M, n_M, v)$  function.

The characteristic of the hydraulic motor overall efficiency  $\eta_M = f(M_M, n_M, \nu)$  presents a complex picture as a product  $\eta_{Mm} \eta_{Mv} \eta_{Mp}$  of three efficiencies correctly described by:

- mechanical efficiency  $\eta_{Mm} = f(M_M, n_M, \nu)$ ,
- volumetric efficiency  $\eta_{Mv} = f(\Delta p_{Mi}, n_M, \nu)$ ,
- and pressure efficiency  $\eta_{Mp} = f(\Delta p_{Mi}, Q_M, \nu)$ .

The picture of the hydraulic motor overall efficiency  $\eta_M = f(M_M, n_M, \nu)$  must be supplemented by assessment of the **motor operating field** ( $0 \leq \bar{\omega}_M \langle \bar{\omega}_{Mmax}, 0 \leq \bar{M}_M \langle \bar{M}_{Mmax}$ ) in the **hydrostatic drive system**, i.e. assessment of the range of  $n_M$  and  $M_M$  ( $\bar{\omega}_M$  and  $\bar{M}_M$ ) parameters.

In the motor (and the drive system) ( $0 \leq \bar{\omega}_M \langle \bar{\omega}_{Mmax}, 0 \leq \bar{M}_M \langle \bar{M}_{Mmax}$ ) operating field its **current speed  $n_M$  ( $\bar{\omega}_M$ ) and load  $M_M$  ( $\bar{M}_M$ )** are an effect of the demand of the motor (system) driven machine (device) **and are independent of the losses in the hydraulic motor and in the motor driving hydrostatic system**.

However, the hydraulic motor (system) operating field limit values  $n_{Mmax}$  ( $\bar{\omega}_{Mmax}$ ) and  $M_{Mmax}$  ( $\bar{M}_{Mmax}$ ) depend on the maximum capacity of the motor driving system. The values  $n_{Mmax}$  ( $\bar{\omega}_{Mmax}$ ) and  $M_{Mmax}$  ( $\bar{M}_{Mmax}$ ) determine simultaneously the corresponding motor energy efficiency  $\eta_M$  and the overall system efficiency  $\eta$ .

The limit parameters of the hydrostatic drive system operation result from the pump theoretical capacity  $Q_{pt}$  and the system nominal working pressure  $p_n$  as well as from the energy losses in the hydraulic motor, pump and conduits and also losses in the motor speed throttling control assembly (if it is installed). Therefore, the limit values  $n_{Mmax}$  ( $\bar{\omega}_{Mmax}$ ) and  $M_{Mmax}$  ( $\bar{M}_{Mmax}$ ) are also dependent on the working fluid viscosity  $\nu$  changing in the  $\nu_{min} \leq \nu \leq \nu_{max}$  range. The hydrostatically driven hydraulic motor operating field is also influenced by the  $\eta_p = f(M_p)$  characteristic of the electric or combustion motor in the pump driving system.

**Evaluation of the hydraulic motor overall efficiency  $\eta_M = f(M_M, n_M, \nu)$  as a product  $\eta_{Mm} \eta_{Mv} \eta_{Mp}$  of three motor efficiencies should be performed by means of the mathematical models of losses and efficiencies, where the defined coefficients  $k_i$  of energy losses in the motor and in the motor drive system are used.**

**Evaluation of the hydraulic motor energy efficiency is performed together with evaluation of the efficiency of a hydrostatic drive system where the motor is used [including also the energy efficiency of pump, conduits and the motor speed throttling control assembly (if it is used)].**

In the proposed method, based on the mathematical models of losses, **each kind of energy losses is a function of parameters directly influencing the losses and independent of those losses.**

Evaluated are the values of the  $k_i$  coefficients of losses, relating the mechanical, volumetric and pressure losses in the hydraulic motor, pump and other system elements to the reference values of driving system nominal pressure  $p_n$ , theoretical capacity  $Q_{pt}$  of the system driving pump, theoretical speed  $n_{Mt}$  and theoretical torque  $M_{Mt}$  of the motor shaft as well as the theoretical speed  $n_{pt}$  and theoretical torque  $M_{pt}$  of the pump shaft. The  $k_i$  coefficients are determined at the hydraulic oil reference viscosity  $\nu_n$ . At the same time the impact is determined of the viscosity ratio  $\nu/\nu_n$  in the  $\nu_{min} \leq \nu \leq \nu_{max}$  range on the  $k_i$  coefficient values.

The method allows to evaluate the values and proportions of mechanical, volumetric and pressure losses in the motor, pump, conduits and in the throttling assembly (if installed), as well as the dependence on the hydraulic oil viscosity  $\nu$ .

**The energy investigations of a pump and hydraulic motor as independent machines are limited to determination of the  $k_i$  coefficients of losses in them. The energy efficiency characteristics of those machines are determined in parallel with efficiency evaluation of the system where they are used.**

The knowledge of  $k_i$  coefficients of the mechanical, volumetric and pressure losses in the drive system elements allows to obtain, with the **numerical method**, the characteristics of the hydrostatic drive system overall efficiency, pump efficiency, hydraulic motor efficiency, conduit efficiency and the motor speed throttling control assembly (if it is used) efficiency in the motor (system) ( $0 \leq \bar{\omega}_M \langle \bar{\omega}_{Mmax}, 0 \leq \bar{M}_M \langle \bar{M}_{Mmax}$ ) operating field at a selected ratio  $\nu/\nu_n$  of the hydraulic oil viscosity and the reference viscosity.

Characteristics of energy efficiency of the pump and hydraulic motor with the determined constant coefficients  $k_i$  of losses and also of efficiency of the conduits are different in hydrostatic systems with different motor speed control structures.

**Characteristics of the overall efficiency of elements used in a hydrostatic drive system: pump  $\eta_p$ , hydraulic motor  $\eta_M$ , conduits  $\eta_C$  and throttling control assembly (if it is used) structural efficiency  $\eta_{st}$  are defined as functions of the hydraulic motor (system) speed coefficient  $\bar{\omega}_M$  and load coefficient  $\bar{M}_M$  and the hydraulic oil viscosity ratio  $\nu/\nu_n$ .**

**At the same time the hydraulic motor ( $0 \leq \bar{\omega}_M \langle \bar{\omega}_{Mmax}, 0 \leq \bar{M}_M \langle \bar{M}_{Mmax}$ ) operating field in the hydrostatic drive system is determined at the selected ratio  $\nu/\nu_n$  of the hydraulic oil viscosity to the reference viscosity.**

**The method is precise by definition and simple in use.** It simplifies the laboratory investigation of pumps, hydraulic motors and hydrostatic drive systems. It allows to seek for energy saving solutions of pumps and hydraulic motors. It allows also to evaluate the overall energy efficiency of the drive and finding energy saving hydrostatic drive system structures.

## CONCLUSIONS

1. The methods of investigating the rotational hydraulic motor losses and energy efficiency, used in scientific research and industrial practice, give incorrect evaluations, because:
  - the losses and efficiencies are evaluated as functions of parameters which depend on those losses or as functions of parameters, which have no direct impact on the losses,
  - the mechanical, volumetric and pressure losses and the corresponding energy efficiencies are presented as dependent on the same parameters, although in fact each of those losses is a function of different parameters and is a different function of the hydraulic oil viscosity  $\nu$ .
2. The basic reason for the incorrect evaluation are common views on the methods of carrying out the investigations and on the method of defining the energy losses in pumps and hydraulic motors. The method is based on the traditional understanding of the hydrostatic drive system energy balance illustrated by the Sankey diagram of the power decrease in the system in the direction of power flow [3 ÷ 6, 15, 17, 19, 21, 22].
3. **Diagram of power increase in a power transmission system opposite to the direction of power flow replaces the Sankey diagram of power decrease in the direction of power flow.**
4. The characteristic of the hydraulic motor overall efficiency  $\eta_M = f(M_M, n_M, \nu)$  as a product  $\eta_{Mm} \eta_{Mv} \eta_{Mp}$  of three efficiencies correctly described by the characteristics of the mechanical

- efficiency  $\eta_{Mm} = f(M_M, n_M, v)$ , volumetric efficiency  $\eta_{Mv} = f(\Delta p_{Mi}, n_M, v)$  and pressure efficiency  $\eta_{Mp} = f(\Delta p_{Mi}, Q_M, v)$ , is very complex.
- Picture of the hydraulic motor overall efficiency  $\eta_M = f(M_M, n_M, v)$  must be supplemented by evaluation of the motor ( $0 \leq \bar{\omega}_M < \bar{\omega}_{Mmax}$ ,  $0 \leq \bar{M}_M < \bar{M}_{Mmax}$ ) operating field in the hydrostatic drive system, i.e. of the  $n_M$  and  $M_M$  ( $\bar{\omega}_M$  and  $\bar{M}_M$ ) range. The hydraulic motor operating field limit values  $n_{Mmax}$  ( $\bar{\omega}_{Mmax}$ ) and  $M_{Mmax}$  ( $\bar{M}_{Mmax}$ ) depend on the maximum capacity of the motor driving hydrostatic system. That capacity is a result of the pump theoretical capacity  $Q_{pt}$ , system nominal pressure  $p_n$  and energy losses in all the system elements, which depend also on the used motor speed control structure.
  - Evaluation of the hydraulic motor overall efficiency  $\eta_M = f(M_M, n_M, v)$  as a product  $\eta_{Mm} \eta_{Mv} \eta_{Mp}$  of the three motor efficiency should be based on the mathematical models of losses and efficiencies where coefficients  $k_i$  of the energy losses in the motor and in the motor driving system are used. Proposed evaluation of the hydraulic motor efficiency is performed together with evaluation of the energy efficiency of pump, efficiency of conduits and efficiency of the throttling control assembly (if it is used) as well as the overall efficiency of the hydrostatic drive system, where the pump, motor, conduits and control system assembly are applied.
  - Evaluated are the values of  $k_i$  coefficients of losses relating the mechanical, volumetric and pressure losses in the hydraulic motor, pump and the whole system to the reference values: theoretical capacity  $Q_{pt}$  of the system driving pump, system nominal pressure  $p_n$ , motor shaft theoretical speed  $n_{Mt}$  and theoretical torque  $M_{Mt}$  as well as the theoretical speed  $n_{pt}$  and theoretical torque  $M_{pt}$  of the pump shaft. The  $k_i$  coefficients of losses are determined at the hydraulic oil reference viscosity. At the same time the impact of the oil viscosity ratio  $v/v_n$  (viscosity in the  $v_{min} \leq v \leq v_{max}$  range) impact on the values of  $k_i$  coefficients of losses is determined.
  - The method allows to evaluate the values and proportions of the mechanical, volumetric and pressure losses in the hydraulic motor, pump and the system and also their dependence on the hydraulic oil viscosity  $v$ .
  - Energy investigations of the pump and hydraulic motor as independent machines are limited to determination of the  $k_i$  coefficients of losses. The energy efficiency characteristics of those machines are determined in parallel with evaluation of efficiency of a hydrostatic system where the machines are used.
  - Knowledge of the values of  $k_i$  coefficients of losses allows to obtain, by a numerical method, of the hydraulic motor efficiency  $\eta_M = f(\bar{\omega}_M, \bar{M}_M, v/v_n)$ , pump efficiency  $\eta_p = f(\bar{\omega}_M, \bar{M}_M, v/v_n)$ , conduit efficiency  $\eta_c = f(\bar{\omega}_M, \bar{M}_M, v/v_n)$ , throttling control assembly (if used) structural efficiency  $\eta_{st} = f(\bar{\omega}_M, \bar{M}_M, v/v_n)$  and the hydrostatic drive system overall efficiency  $\eta = f(\bar{\omega}_M, \bar{M}_M, v/v_n)$  in the hydraulic motor (system) ( $0 \leq \bar{\omega}_M < \bar{\omega}_{Mmax}$ ,  $0 \leq \bar{M}_M < \bar{M}_{Mmax}$ ) operating field and at the selected ratio  $v/v_n$  of hydraulic oil viscosity.
  - The method is precise by definition and simple in use. It simplifies the laboratory investigations of pumps, hydraulic motors and hydrostatic drive systems. It allows to evaluate the characteristics of the system overall energy efficiency as well as to seek for the energy saving hydrostatic drive structures.
  - The method is a proposition for the pump, hydraulic motor, hydrostatic drive and control system designers and manufacturers. It is in the process of development.

## BIBLIOGRAPHY

- Electric drives improve load cycle performance.* MacGREGOR News 154 Autumn 2006
- Electric drives advantages are available to all ship types.* MacGREGOR News 161 Autumn 2010
- Paszota Z.: *Direction of increase of power stream in the hydrostatic drive and control system. Graphical presentation of the power of energy losses and power developed in the elements of hydrostatic drive and control system. Part I – Rotational hydraulic motor speed series throttling control systems.* (in Polish), Napędy i sterowanie, scientific monthly, No 10 (114), October 2008
- Paszota Z.: *Direction of increase of power stream in the hydrostatic drive and control system. Graphical presentation of the power of energy losses and power developed in the elements of hydrostatic drive and control system. Part II – Rotational hydraulic motor speed parallel throttling control and volumetric control systems.* (in Polish), Napędy i sterowanie, scientific monthly, No 11 (115), November 2008
- Paszota Z.: *Graphical presentation of the power of energy losses and power developed in the elements of hydrostatic drive and control system. Part I – Rotational hydraulic motor speed series throttling control systems.* Polish Maritime Research 03/2008
- Paszota Z.: *Graphical presentation of the power of energy losses and power developed in the elements of hydrostatic drive and control system. Part II – Rotational hydraulic motor speed parallel throttling control and volumetric control systems.* Polish Maritime Research 04/2008
- Paszota Z.: *The operating field of a hydrostatic drive system.* Chapter in the monograph: „Research, design, production and operation of hydraulic systems” (in Polish), Adam Klich, Antoni Kozieł and Edward Palczak editors. „Cylinder” Library. Komag Mining Mechanisation Centre, Gliwice 2009
- Paszota Z.: *Parameters of the energy efficiency investigations of pumps and hydraulic motors. The operating field of a hydrostatic drive system.* (in Polish), Napędy i sterowanie, scientific monthly, No 11 (127), November 2009
- Paszota Z.: *The operating field of a hydrostatic drive system parameters of the energy efficiency investigations of pumps and hydraulic motors.* Polish Maritime Research 04 / 2009
- Technical matter of the Hägglunds Company: Product Manual VIKING EN397-3a 1999
- Technical matter of the Bosch Rexroth AG Company: RE 91 604/06.03 I AGVM
- Technical matter of the Parker Hannifin Company: Catalogue HY30-8223/UK
- Technical matter of the SAUER DANFOSS Company: Technical Information 520L0440·Rev AD·Dec 2009
- Technical matter of the LABORATOIRE HYDRO LEDUC Company: Efficiency M series motors
- Paszota Z.: *Energy losses in a rotational hydraulic motor – definitions and relations for evaluation of the efficiency of motor and hydrostatic drive.* Chapter in the monograph: „Research, design, production and operation of hydraulic systems” (in Polish), Adam Klich, Antoni Kozieł and Edward Palczak editors. „Cylinder” Library. Komag Mining Mechanisation Centre, Gliwice 2010
- Paszota Z.: *Theoretical and mathematical models of the torque of mechanical losses in a hydraulic rotational motor for hydrostatic drive.* Chapter in the monograph: „Research, design, production and operation of hydraulic systems” (in Polish), Adam Klich, Antoni Kozieł and Edward Palczak editors. „Cylinder” Library. Komag Mining Mechanisation Centre, Gliwice 2010
- Paszota Z.: *Energy losses in a rotational hydraulic motor – definitions and relations for evaluation of the efficiency of motor and hydrostatic drive.* (in Polish), Napędy i sterowanie, scientific monthly, No 10(138), October 2010
- Paszota Z.: *Theoretical and mathematical models of the torque of mechanical losses in a hydraulic rotational motor for hydrostatic drive.* (in Polish), Napędy i sterowanie, scientific monthly, No 11(139), November 2010

19. Paszota Z.: *Energy losses in the hydraulic rotational motor – definitions and relations for evaluation of the efficiency of motor and hydrostatic drive*. Polish Maritime Research 2/2010
20. Paszota Z.: *Theoretical and mathematical models of the torque of mechanical losses in a hydraulic rotational motor for hydrostatic drive*. Polish Maritime Research 3/2010
21. Paszota Z.: *Hydrostatic drives as safe and energy saving machines*. (in Polish), Napędy i sterowanie, scientific monthly, No 1(141), January 2011
22. Paszota Z.: *Hydrostatic drives as safe and energy saving machines*. (in Polish), Proceedings of the „Innovative machines and Technologies - Safety” conference, Szczyrk 03 – 04 February 2011

## CONTACT WITH THE AUTHOR

Prof. Zygmunt Paszota  
Faculty of Ocean Engineering  
and Ship Technology  
Gdansk University of Technology  
Narutowicza 11/12  
80-233 Gdansk, POLAND  
e-mail: [zpaszota@pg.gda.pl](mailto:zpaszota@pg.gda.pl)

# Three-dimensional cfd analysis to study the thrust and efficiency of a biologically-inspired marine propulsor

Lamas M. I., Assoc. Prof.  
Rodríguez J. D., Assoc. Prof.  
Rodríguez C. G., M. Sc.  
González P. B., Prof.  
Escola Universitaria Politécnica.  
Universidade da Coruña

## ABSTRACT

*Aquatic animals, which are the result of many millions of years of evolutionary optimization, are very quick, efficient, robust, and versatile. Accordingly, biologically-inspired mechanisms which emulate the movement of animals have recently become very popular. For the efficient design of a propulsion system it is very important to analyze the fluid flow in detail. CFD (Computational Fluid Dynamics) has become a powerful technique to understand the phenomena because it gives extensive information about the fluid flow characteristics.*

*In the present work, a propulsion system consisting of an undulating fin which emulates the fish swimming was built. In order to optimize the mechanism, several undulating configurations were studied using a 3D turbulent CFD model. The thrust, drag, efficiency and hydrodynamic characteristics were analyzed. Furthermore, it was shown that the efficiency and thrust depend strongly on the oscillation frequency, amplitude and wavelength.*

*In order to validate this CFD model, the numerically obtained thrust was successfully compared with experimental results from the laboratory mechanism.*

**Keywords:** fish swimming; marine propulsion; undulating fin; biomimetic; computational fluid dynamics; CFD

## INTRODUCTION

Biomimetic is an emerging field which employs the principles of living organisms to derive man-made mechanisms which are capable of emulating the efficient movement of animals. In the field of marine propulsion, undulating fish-like mechanisms offers many advantages over rotary propellers. What makes the high efficiency and high thrust of the biologically movement is the manner in which it works. Behind the fin, several vortices are formed with a rotation direction compatible with the direction of thrust, producing an efficient jet. On the contrary, a propeller generates a long jet that rotates in the direction perpendicular to the motion, wasting a considerable amount of power that goes into rotating this jet.

Under the same conditions, a fish consumes much less energy to displace than a rigid body because the motion of the fish contributes to a reduced drag force and increased propulsive efficiency by reducing separation and suppressing turbulence (Shen *et al.*, 2003). Recent works have shown that undulating fish movement is very efficient compared to rigid bodies (Barret *et al.*, 1999, Liu and Kawachi, 1999, Triantafyllou, 1995) and there are several researchers interested in fish-like underwater and surface ships. For example, Barret *et al.* (1999) constructed

a fish-like mechanism and studied it on a laboratory in order to compare the undulating fish movement with a rigid wall movement. They concluded that the power required to propel an actively swimming fish-like body is significantly smaller than the power needed to tow the body straight and rigid and they obtained drag reductions up to 70% for the undulating fish movement. Zhang *et al.* (2008) investigated the bionic neutral network control method for fish-robots and developed a 2D laminar CFD model to study several amplitude envelopes. Young-hua *et al.* (2007) designed an environment-friendly propulsion system mimicking undulating fins and developed a two-dimensional CFD method to study the unsteady flow around the fin. They focused its study on studying the amplitude configuration. Bozkurtass *et al.* (2008) constructed a propulsor for an autonomous underwater vehicle based on the mechanical design and performance of a sunfish pectoral fin, and developed a three-dimensional numerical model. Low (2008) constructed an underwater vehicle using a fin-like mechanism based on a series of connecting linkages which produce undulations similar to those produced by the fin rays. Clark and Smith (2007) built a flexible fin which replicates some features of the pectoral fin of a batoid fish.

Although these studies have revealed many key points of undulating propulsion, much is still unknown regarding the

behavior of the unsteady fluid flow. Recently, CFD has become a powerful tool to study these phenomena. By solving the Navier-Stokes equations, CFD provides information on the pressure and velocity fields. It is very useful to complement traditional testing and experimentation, providing faster time and lower costs. In this work, an undulating propulsor which emulates the high performance and maneuvering of fish swimming was built. In order to analyze the flow around the fin, a tri-dimensional turbulent CFD model was developed. A previously 2D CFD model was already developed elsewhere (Lamas *et al.*, 2010). In the present paper, the 2D model was extended to the more realistic 3D situation. This numerical model was satisfactory compared with the experimental data obtained from the experimental prototype. Once validated, the CFD analysis was employed to predict how the performance varies with different parameters.

This paper begins with an introduction of the experimental prototype and the kinematics of locomotion. The numerical method and results are then briefly described and contrasted with experimental data. Finally, the conclusions of this work and the areas for future research are presented.

## PROBLEM DEFINITION

### Design and kinematics

The experimental ship is shown in Fig. 1.a. The propulsive fin, which is shown in Fig. 1.b, consists of a flexible surface of 0.52 m length and 0.2 m width.

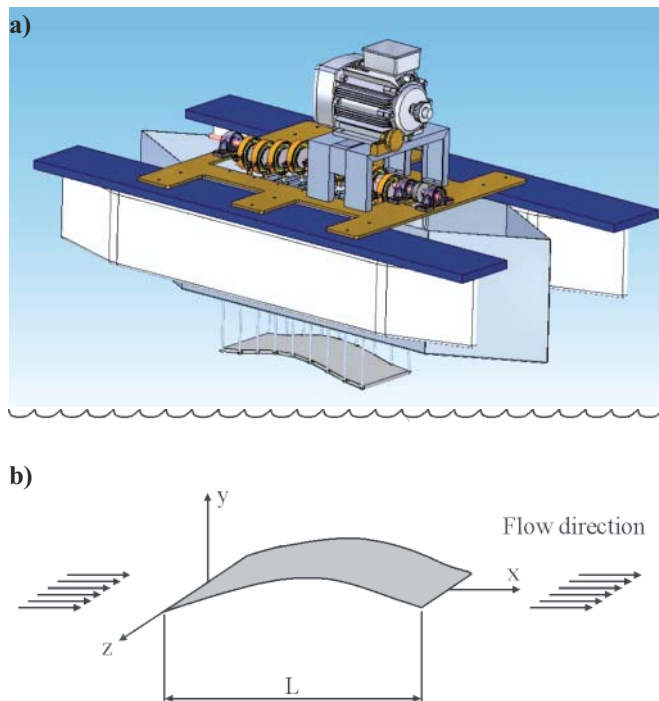


Fig. 1. a) experimental mechanism, b) detail of the fin

Fig. 2 provides the mechanism of the undulating fin, consisting of eight rigid segments, each capable of relative rotation with respect to its neighboring links. The movement of each segment is produced by a crankshaft situated above the fin. The power is supplied by an electric motor and the oscillation frequency is controlled by a variable-frequency drive control.

Every module is attached to a connecting rod on both sides. The position of every segment is defined by the rotation of the crankshaft, which moves the rods, the connecting rods, and finally the segment. In order to investigate what kind of

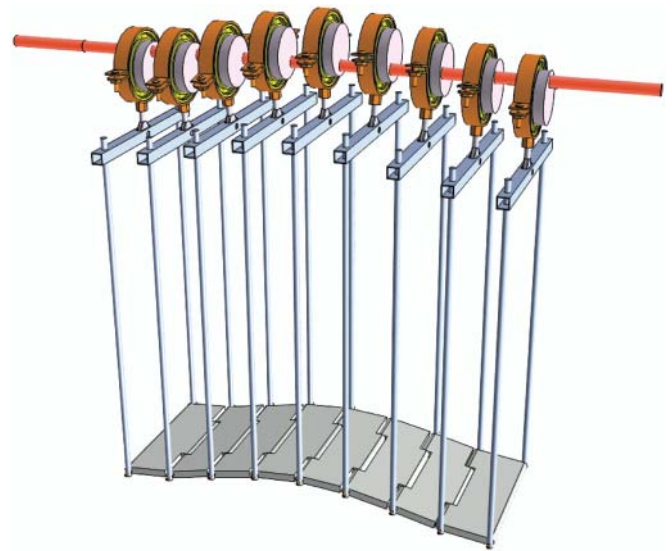


Fig. 2. Detail of the undulating surface and mechanical transmission of movement

amplitude envelope provides the maximum efficiency, the mechanism was designed to accommodate several centimeters peak-to-peak amplitude. More details of the system were given elsewhere (Rodríguez, 2009).

The high thrust and efficiency are not the only advantages of this system. It is also reversible, *i.e.*, it has the same efficiency either operating forward or backward. This makes it ideal for vehicles that require high maneuverability. Other advantage is that the use of several properly positioned fins can minimize vibrations.

### Governing equations

The fluid flow around this mechanism was studied numerically. In order to simplify the model, the flow was considered incompressible and isothermal. The unsteady turbulent flow was simulated by the RANS (Reynolds-averaged Navier-Stokes) equations. In Cartesian tensor form, the mass conservation equation is given by:

$$\frac{\partial \rho}{\partial t} + \frac{\partial}{\partial x_i} (\rho u_i) = 0 \quad (1)$$

and the momentum conservation equation:

$$\begin{aligned} \frac{\partial}{\partial t} (\rho u_i) + \frac{\partial}{\partial x_j} (\rho u_i u_j) = \\ = -\frac{\partial p}{\partial x_i} + \frac{\partial \tau_{ij}}{\partial x_j} + \frac{\partial}{\partial x_j} (-\rho \overline{u_i' u_j'}) \end{aligned} \quad (2)$$

Since the fluid was treated as Newtonian, the stress tensor components are given by:

$$\tau_{ij} = \mu \left( \frac{\partial u_i}{\partial x_j} + \frac{\partial u_j}{\partial x_i} - \frac{2}{3} \delta_{ij} \frac{\partial u_k}{\partial x_k} \right) \quad (3)$$

A common method to model the Reynolds stresses,  $-\rho \overline{u_i' u_j'}$ , is the Boussinesq hypothesis to relate the Reynolds stresses to the mean velocity gradients:

$$-\rho \overline{u_i' u_j'} = \mu_t \left( \frac{\partial u_i}{\partial x_j} + \frac{\partial u_j}{\partial x_i} \right) - \frac{2}{3} \left( \rho k + \mu_t \frac{\partial u_k}{\partial x_k} \right) \delta_{ij} \quad (4)$$

where  $\delta_{ij}$  is the Kronecker delta ( $\delta_{ij} = 1$  if  $i = j$  and  $\delta_{ij} = 0$  if  $i \neq j$ ) which is included to make the formula applicable to the normal Reynolds stresses for which  $i = j$  (Versteeg and

Malalasekera, 2007) and  $\mu_t$  is the turbulent viscosity. Since the turbulent viscosity was modeled by the k- $\epsilon$  model, two transport equations are added, one for the turbulence kinetic energy k (eq. 5) and a further one for its dissipation rate  $\epsilon$  (eq. 6) respectively. Unfortunately, no single turbulence model is universally accepted. The reasons why the k- $\epsilon$  model was applied in this work are that it is robust, computationally economical and reasonably accurate for a wide range of turbulent flows.

$$\begin{aligned} & \frac{\partial}{\partial t}(\rho k) + \frac{\partial}{\partial x_i}(\rho k u_i) = \\ & = \frac{\partial}{\partial x_j} \left[ \left( \mu + \frac{\mu_t}{\sigma_k} \right) \frac{\partial k}{\partial x_j} \right] + G_k + G_b - \rho \epsilon - Y_M \end{aligned} \quad (5)$$

$$\begin{aligned} & \frac{\partial}{\partial t}(\rho \epsilon) + \frac{\partial}{\partial x_i}(\rho \epsilon u_i) = \frac{\partial}{\partial x_j} \left[ \left( \mu + \frac{\mu_t}{\sigma_\epsilon} \right) \frac{\partial \epsilon}{\partial x_j} \right] + \\ & + C_{1\epsilon} \frac{\epsilon}{k} (G_k + G_{3\epsilon} G_b) - C_{2\epsilon} \rho \frac{\epsilon^2}{k} \end{aligned} \quad (6)$$

In the above equations,  $G_k$  represents the generation of turbulence kinetic energy due to the mean velocity gradients;  $G_b$  is the generation of turbulence kinetic energy due to buoyancy;  $Y_M$  represents the contribution of the fluctuating dilatation in compressible turbulence to the overall dissipation rate.  $C_\mu$ ,  $C_{1\epsilon}$ ,  $C_{2\epsilon}$ ,  $C_{3\epsilon}$ ,  $\sigma_k$  and  $\sigma_\epsilon$  are constants with the standard k- $\epsilon$  default values  $C_\mu = 0.09$ ;  $C_{1\epsilon} = 1.44$ ;  $C_{2\epsilon} = 1.92$ ;  $\sigma_k = 1.0$  and  $\sigma_\epsilon = 1.3$ . Details are given in (Fluent Inc., 2006).

The turbulent viscosity,  $\mu_t$ , is computed by combining k and  $\epsilon$  as follows:

$$\mu_t = \rho C_\mu \frac{k^2}{\epsilon} \quad (7)$$

## NUMERICAL IMPLEMENTATION

### Computational mesh

In order to implement the movement of the fin, a moving mesh which regenerates with time was employed. The computational domain is shown in Fig. 3, in which the front surface and the internal mesh were omitted for clarity. It was discretized with 600000 tetrahedral elements. The size mesh was refined near the fin and in the wake region to resolve the shed vortices as they travel downstream. Due to the symmetry of the problem, only half of the geometry was modeled.

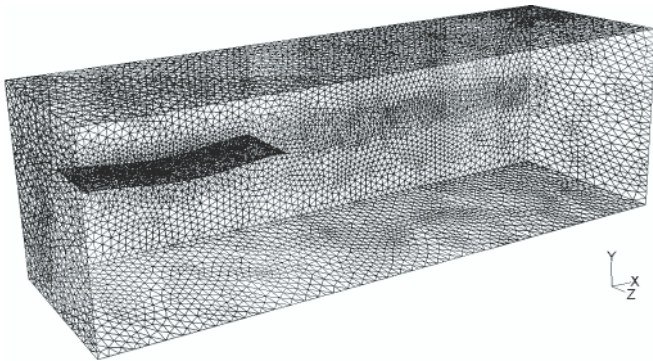


Fig. 3. Computational domain

### Boundary Conditions

The downstream boundary (right surface) was modeled as a pressure outlet and the upstream boundary condition (left surface) was modeled as an uniform velocity inlet

corresponding to the free-stream velocity. The fin surface was treated as a no-slip moving wall. The top and bottom sides were modeled as no slip walls and the front surface was treated as a symmetry plane.

## Numerical Methodology

The numerical solution was performed using the commercial software Ansys Fluent 6.3, which is based on the finite volume method. Pressure-velocity coupling was achieved using the PISO algorithm. A second order scheme was used for discretization of the pressure and momentum equations. The time integration was achieved using a first order fully implicit scheme with a constant time step of 0.001 s.

Extensive convergence checks were taken in order to confirm that the computed results are independent of the time step, the grid size and the computational domain size.

## CALCULATION OF FORCES AND EFFICIENCY

As the fin moves through the water, a force is produced along the x, y and z directions. Particularly, a pressure force is caused due to pressure difference and a friction force is caused due to water viscosity. The components of the forces acting on the body,  $F_x$ ,  $F_y$  and  $F_z$  can be evaluated by integrating the projection of the pressure and the shear stress in the x, y and z directions respectively. The total component along the x direction was computed by adding the component x of the pressure and viscous forces acting on the body as follows:

$$F_x = F_{px} + F_{vx} \quad (8)$$

where:

$F_{px}$  – the pressure force

$F_{vx}$  – the viscous force in the x direction.

The pressure force along the x axis is given by:

$$F_{px} = - \int_A p n_x dS \quad (9)$$

where:

$n_x$  – the x component of the unit normal vector on dS.

The viscous force along the x axis is given by:

$$F_{vx} = \int_A \tau_{xj} n_j dS \quad (10)$$

where:

$\tau_{xj}$  – the viscous stress tensor.

The total power required for the propulsive motion of the fin ( $P_T$ ) consists of two components,  $P_T = P_S + P_U$ . One is the swimming power ( $P_S$ ) required to produce the vertical oscillations of the fin and the other is the useful power ( $P_U$ ), required to thrust. The swimming power was computed as:

$$P_S = \int p \frac{dy_{wall}}{dt} dS \quad (11)$$

where p is the pressure of the surface of the plate and  $dy_{wall}/dt$  refers to the y-component of the velocity at the surface of the fish. For a sinusoidal wavy the motion of the fin and the y-component of the velocity are given by Ec. (12) and (13) respectively.

$$y = A(x) \cdot \sin \left[ 2\pi \left( \frac{x}{\lambda} - \frac{t}{T} \right) \right] \quad (12)$$

$$\frac{dy_{\text{wall}}}{dt} = -\frac{2\pi}{T}A(x) \cdot \cos\left[2\pi\left(\frac{x}{\lambda} - \frac{t}{T}\right)\right] \quad (13)$$

where:

$A(x)$  – represents the amplitude,  
 $\lambda$  – the wavelength,  
 $T$  – the period.

The useful power was computed as the time-average thrust multiplied by the free-stream velocity:

$$P_U = -F_{\text{px}} U_\infty \quad (14)$$

where the minus sign indicates that the velocity of swimming is reverse to that of the stream.

The efficiency was computed as the ratio between the useful power and the total power. Obviously, the efficiency is always less than one because of losses due to wayward vortices and turbulence.

## RESULTS AND DISCUSSION

### Configurations Studied

The motion of the fin is in the form of a streamwise travelling wave. As the fluid moves along the surface, the undulations from the anterior to the posterior of the fin produce thrust. The amplitude may vary along the length, and its design is very important. For this reason, several CFD analysis were carried out to assess the most suitable configuration. Three cases were studied: amplitude increasing from the anterior part to the posterior (Fig. 4a), constant amplitude (Fig. 4b) and amplitude increasing from the anterior part to the mid part and decreasing towards the posterior (Fig. 4c).

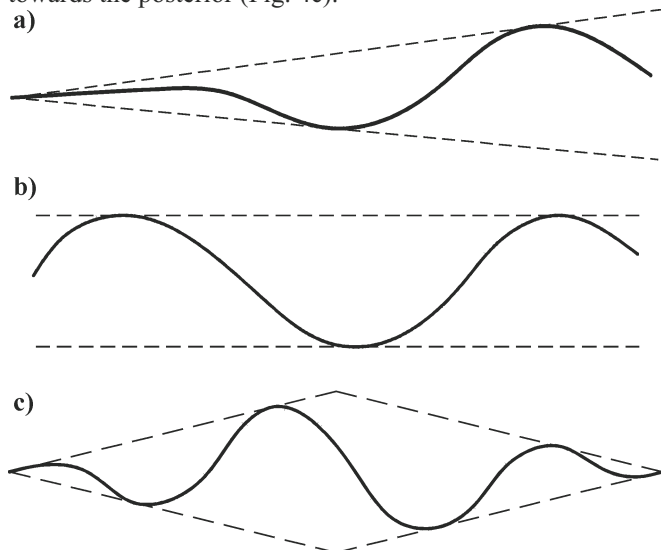


**Fig. 4.** Amplitude configurations. **a)** amplitude increasing from the anterior part to the posterior, **b)** constant amplitude, **c)** amplitude increasing from the anterior part to the mid part and decreasing towards the posterior

### Hydrodynamic forces and efficiency

Fig. 5a represents the time history of the instantaneous pressure force, viscous force and average total force along the cycle at  $U_\infty = 0$ ;  $f = 10$  Hz;  $A_{\text{max}} = 0.02$  m and  $\lambda = 1$  m. The zero free-stream velocity corresponds to a experimental situation in which the ship is tied to a fixed point by means of a rope, Fig. 5b. The configuration studied in Fig. 5a corresponds to (a), i.e., amplitude increasing from the anterior part to the posterior, and the other two amplitude configurations presented a similar tendency, so they are not plotted again.

In order to reach a situation which periodically repeats, i.e., a quasi-steady state, it was necessary to study a long enough interval of time. For the cases studied it was verified that this state is achieved after approximately twenty fin oscillation periods. For this reason, all the results carried out in the present paper correspond to the 20<sup>th</sup> period of time.

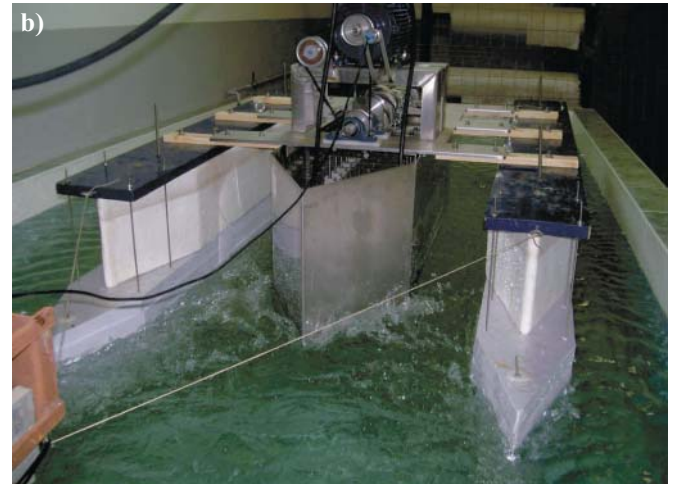
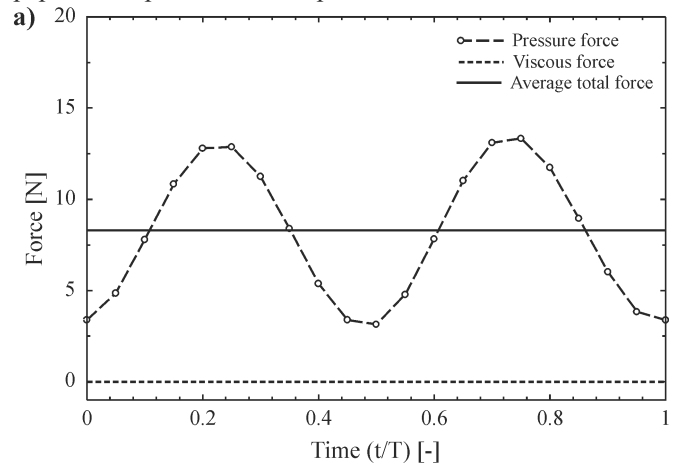


**Fig. 5.** **a)** time history of the instantaneous thrust and drag and average total force at  $U_\infty = 0$ ;  $f = 10$  Hz;  $A_{\text{max}} = 0.02$  m and  $\lambda = 1$  m. Configuration (a), amplitude increasing from the anterior part to the posterior; **b)** equivalent experimental situation (pulling against a fixed point)

The forces shown in Fig. 5a are the ones that accelerate the fin either forward or backward, depending on its sign. For the above conditions the mechanism is accelerating, i.e., the pressure force is much higher than the viscous force. If the rope is broken and the ship is allowed to displace, after accelerating it tends towards an asymptotic state in which the mean velocity is constant and the net thrust (i.e., sum of pressure and viscous force) is zero. For the parameters of the figure above, this situation is obtained at  $U_\infty = 5.1$  m/s, and the respective forces are represented in Fig. 6.

From the figures above, it can be observed that the instantaneous pressure force reaches its maximum value twice in each cycle because of the symmetrical undulating movement. The maximum thrust takes place at the time that the ends of the fin are in the position corresponding to zero amplitude. On the contrary, the worst case occurs at the point where the edges of the fin are in the position corresponding to its maximum amplitude.

The period-average thrust and efficiency of the three cases studied are summarized in Table 1, in which the negative sign was used to denote the direction opposite to that of the stream.

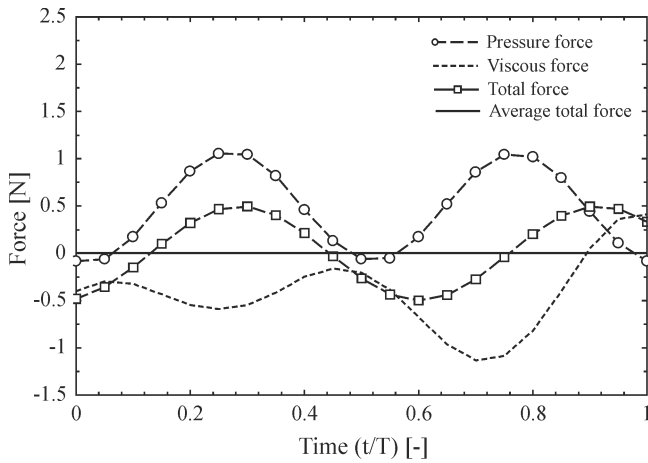


**Fig. 6.** Time variation of instantaneous thrust and drag and average total force at  $U_\infty = 5.1$  m/s;  $f = 10$  Hz;  $A_{max} = 0.02$  m and  $\lambda = 1$  m. Configuration (a), amplitude increasing from the anterior part to the posterior

**Tab. 1.** Period-averaged thrust and efficiency for the three fin undulating patterns at  $U_\infty = 5.1$  m/s;  $f = 10$  Hz;  $A_{max} = 0.02$  m and  $\lambda = 1$  m.

Fin undulating pattern	Thrust (N)	Efficiency (%)
Configuration (a)	0	44.4
Configuration (b)	1.8	34.5
Configuration (c)	-2.96	22.5

- (a) Amplitude increasing from the anterior part to the posterior.
- (b) Constant amplitude.
- (c) Amplitude increasing from the anterior part to the mid part and decreasing towards the posterior.

From Table 1, it can be seen that the case with amplitude increasing from the anterior part to the mid part and decreasing towards the posterior (configuration c) is the worst configuration because it corresponds to the lowest efficiency and thrust. The case with constant amplitude (configuration b) produces the highest thrust and the one with amplitude increasing from the anterior part to the posterior (configuration a) produces the highest efficiency. This conclusion was expected because the travelling waves with increasing amplitude are a typical form adopted for swimming motion of live fish in nature. The most effective amplitude configuration, case a, will be discussed further in the following sections.

### Pressure field

Fig. 7 shows the pressure distribution in the zone closed to the fin. It corresponds to the pattern with amplitude increasing from the anterior part to the posterior at  $U_\infty = 5.1$  m/s;  $f = 10$  Hz;  $A_{max} = 0.02$  m and  $\lambda = 1$  m.

The iso-pressure contours show areas of high and low pressures. Behind the fin a high pressure region is created and hence a propulsive jet which produces thrust. As discussed previously, the peak for pressure and viscous forces do not occur simultaneously. The maximum pressure force occurs at instants of approximately maximum amplitude at the tail, when the pressure gradient attached to the body acts to pull the fish upstream,  $0.25t/T$  and  $0.75t/T$  in Fig. 7. On the other hand, the minimum viscous force occurs when the undulatory wave has a maximum amplitude at approximately the midpoint of the fin,  $0.5t/T$  in Fig. 7, when the pressure gradients are smaller.

From Fig. 7 it can also be seen that a staggered array of reverse von Karman vortices forms behind the fin, which

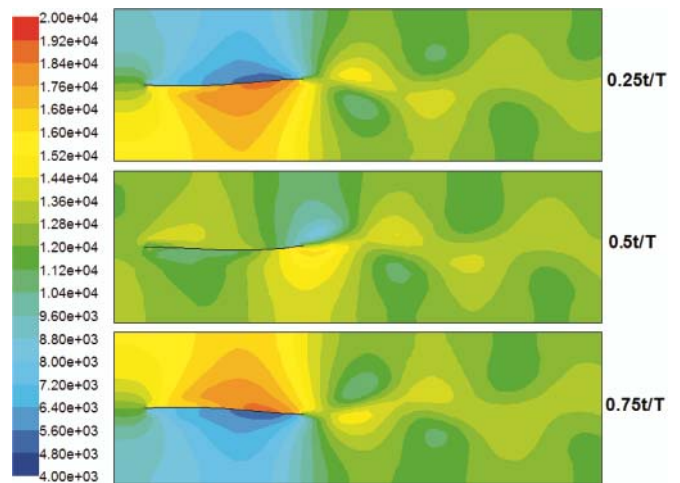


**Fig. 7.** Pressure field (Pa) at  $U_\infty = 5.1$  m/s;  $f = 10$  Hz;  $A_{max} = 0.02$  m and  $\lambda = 1$  m. Configuration (a), amplitude increasing from the anterior part to the posterior

decay downstream due to viscous dissipation. These vortices are very important because they are closely related to the jet stream which generates an opposite force to thrust the body forward and their optimal formation would increase efficiency noticeable.

### Velocity field

Fig. 8 shows the velocity field of the pattern with amplitude increasing from the anterior part to the posterior at  $U_\infty = 5.1$  m/s;  $f = 10$  Hz;  $A_{max} = 0.02$  m and  $\lambda = 1$  m. It corresponds to Fig. 7.

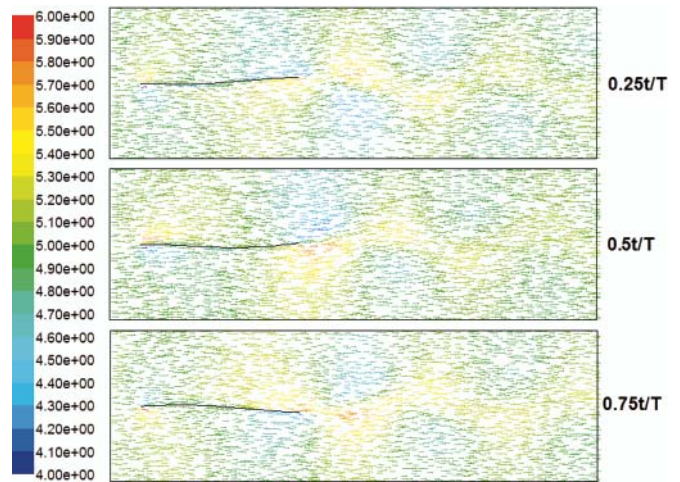


**Fig. 8.** Velocity field (m/s) at  $U_\infty = 5.1$  m/s;  $f = 10$  Hz;  $A_{max} = 0.02$  m and  $\lambda = 1$  m. Configuration (a), amplitude increasing from the anterior part to the posterior

In this picture, the downstream-directed jet and the von Karman vortices are appreciated too. The streamwise velocity in this thrust jet is as much as 20% greater than the free-stream velocity, so the fish increases the momentum of the fluid in the wake.

### Influence of the amplitude, frequency and wavelength

The influence of the maximum amplitude, oscillation frequency and wavelength on the thrust and efficiency was analyzed and represented in Fig. 9. This figure was carried out for the configuration (a), amplitude increasing from the anterior part to the posterior and zero free-stream velocity. The other two configurations presented similar tendencies.

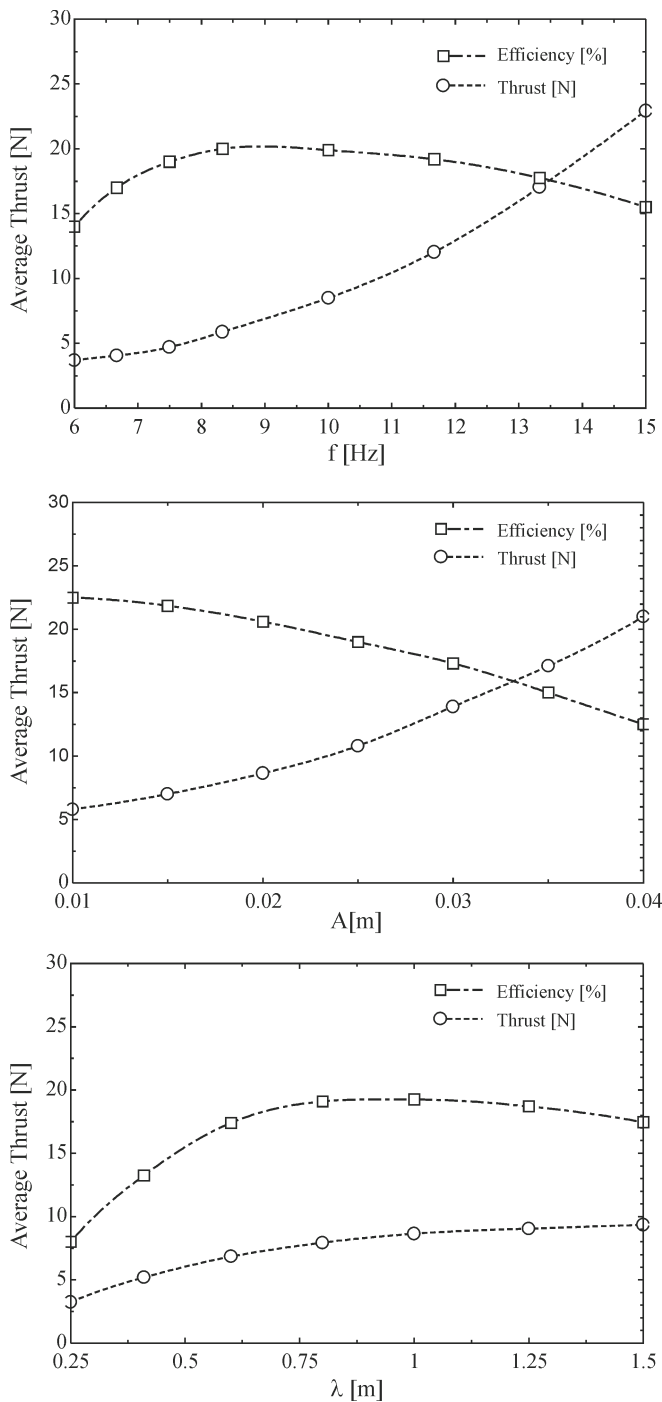


**Fig. 9.** Variation of the period-average thrust and efficiency with amplitude, frequency and wavelength at  $U_\infty = 0$  m/s. Configuration (a), amplitude increasing from the anterior part to the posterior

From the figures above it can be seen that, as expected, the thrust increases when the oscillation frequency increases. As the frequency increases, the efficiency increases rapidly to its maximum and then decreases gradually. Other studies realized in flapping foils and fishes confirmed that the efficiency is maximum in a limited range of frequency. (Triantafyllou, 1995; Liu and Kawachi, 1999; Deng *et al.*, 2005).

In what concerns the maximum amplitude, it can be seen that the thrust increases with increasing amplitude. However, this is at the expense of even larger power cost required and hence less efficiency. On the other hand, at smaller amplitudes the efficiency is higher but it is more difficult to generate an effective thrust.

In what concerns the wavelength, as the wavelength increases, the average thrust at first increases up to a certain

maximum value and then decreases, while the efficiency increases monotonically.

From the calculated results, the best option should be a combination of thrust and efficiency. It would depend on every practical case. For example, military applications require high specific power even though the efficiency is not optimal. On the contrary, for civil applications the most important issue is the efficiency.

## EXPERIMENTAL RESULTS

A validation test was carried out in order to assess the adequacy of the computational model developed here. The experimental results were based on tying the ship to a fixed point by means of a rope, Fig. 5b. Once the prototype was fixed, the force was measured at different oscillation frequencies of the fin. A load cell was used to measure these forces and a variable-frequency drive control was used to control the oscillation frequency of the electrical motor.

Numerically, it was simulated with zero free-stream velocity. Numerical and experimental results for the average thrust force against the frequency are compared in Fig. 10.

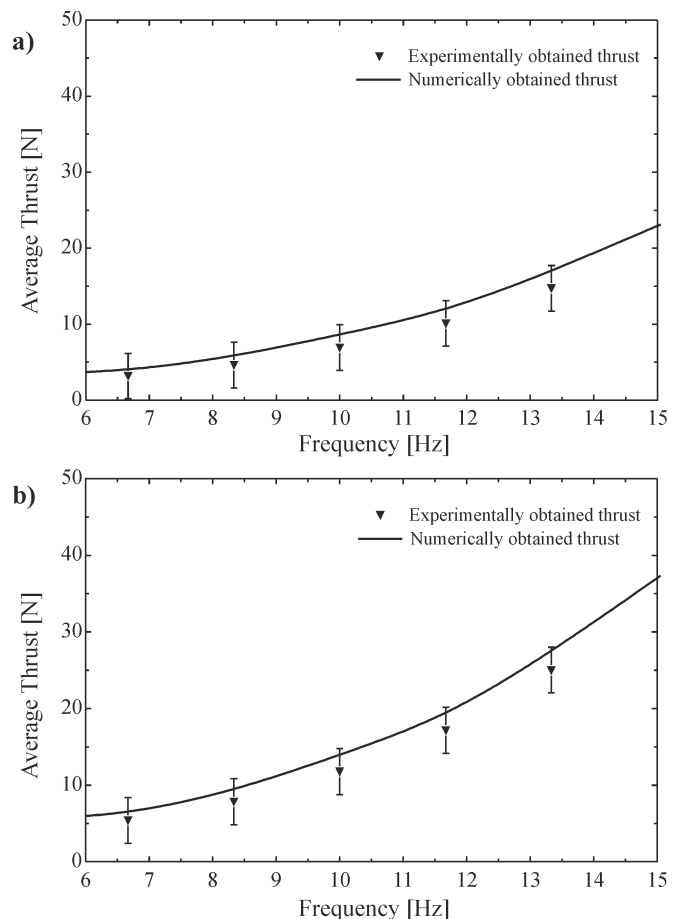


**Fig. 10.** Average force against frequency for numerical and experimental results. **a)** amplitude increasing from the anterior part to the posterior; **b)** constant amplitude

From the figure above, it can be seen that the experimental results were in good agreement with numerical ones, which means that this CFD model can accurately predict the physical phenomena.

## CONCLUSIONS

In this work, a fish-like marine propulsor was designed and the fluid around the mechanism was numerically investigated

by solving the three-dimensional incompressible Navier-Stokes equations. The hydrodynamics of the fluid flow, pressure and velocity fields were obtained. The efficiency and forces (which were decomposed into pressure and viscous forces) were obtained too. The influence of the amplitude envelope was studied, concluding that the configuration with amplitude increasing from the anterior part to the posterior is the most efficient. Several values of the frequency, wavelength and maximum amplitude were analyzed and it was found that the efficiency and thrust depend strongly on these parameters. Particularly, the thrust increases both with the increase of the frequency and the amplitude; the efficiency decreases with increasing the amplitude and as the frequency or the wavelength increases, the efficiency increases to its maximum and then decreases gradually. For this reason, the results obtained in this study provide interesting information on the performance of fish-like mechanisms and demonstrate that a properly design of the fin can be very appropriate for ships and underwater vehicles. The optimal propulsive mechanism would be a combination of the properly thrust or efficiency, depending on every practical application.

While CFD is a very powerful tool, it can not be applied blindly as it has the capability to produce non-physical results due to erroneous modeling. For this reason, the numerically obtained thrust was compared with experimental results from the laboratory mechanism to ensure that the model accurately predicts the physical phenomena.

#### Acknowledgements

The authors wish to thank to Xunta de Galicia its financial support through the project "Sistema de propulsión ondulante", PGIDIT06DPI172PR8.

#### NOMENCLATURE

L	– Fin length [m]
t	– Time [s]
F	– Force [N]
A	– Amplitude [m]
S	– Surface [m <sup>2</sup> ]
n	– Unit normal vector [-]
u	– Velocity [m/s]
T	– Period [s]
f	– Oscillation frequency [Hz]
p	– Pressure [Pa]
g	– Gravity [m/s <sup>2</sup> ]
C <sub>μ</sub> , C <sub>e</sub>	– Empirical constant coefficients [m <sup>2</sup> /s <sup>2</sup> ]
k	– Turbulent kinetic energy [m <sup>2</sup> /s <sup>2</sup> ]
τ	– Viscous stress tensor [N/m <sup>2</sup> ]
ρ	– Density [kg/m <sup>3</sup> ]
μ	– Dynamic viscosity [Pa-s]
λ	– Wavelength [m]
η	– Efficiency [-]
δ <sub>ij</sub>	– Kronecker delta [-]
μ <sub>t</sub>	– Turbulent viscosity [kg/m-s]
τ	– Viscous stress tensor [N/m <sup>2</sup> ]
ε	– Dissipation rate of turbulent kinetic energy [m <sup>2</sup> /s <sup>2</sup> ]

#### Subscripts

x, y, z	– X, Y, Z directions
i	– Cartesian coordinate (i = 1, 2, 3)
j	– Cartesian coordinate (j = 1, 2, 3)

max	– Maximum
p	– Pressure
v	– Viscosity
T	– Total
S	– Swimming
U	– Useful
∞	– Free-stream

#### BIBLIOGRAPHY

- Shen, L., Zhang, X., Yue, D. K. P., (2003), Turbulent flow over a flexible wall undergoing a streamwise travelling wave motion, *Journal of Fluid Mechanics*, vol. 484, pp. 197-221.
- Barret, D. S., Triantafyllou, M. S., Yue, D. K. P., Grosenbaugh, M. A., and Wolfgang, M. J. (1999) Drag reduction in fish-like locomotion. *Journal of Fluid Mechanics* 392, 183-212.
- Liu, H., Kawachi, K. (1999) A numerical study of undulatory swimming, *Journal of Computational Physics* 155, pp. 223-247.
- Triantafyllou, M. S., Triantafyllou, G. S., (1995). An efficient swimming machine. *Scientific American*, vol. 272, issue 3, pp. 64-70.
- Zhang, D., Hu, D., Shen, L., Xie, H., (2008), Design of an artificial bionic neural network to control fish-robot's locomotion, *Neurocomputing* 71, pp. 648-654.
- Yong-hua Zhang, Jia, L., Zhang, S., Yang, J., Low, K. H. (2007) Computational research on modular undulating fin for biorobotic underwater propulsor. *Journal of Bionic Engineering* 4, 25-32.
- Bozkurtas, M., Tangorra, J., Lauder, G., Mittal, R. (2008) Understanding the hydrodynamics of swimming: from fish fins to flexible propulsors for autonomous underwater vehicles. *Advances in Science and Technology* 58, 193-202.
- Low, K. H. (2008) Locomotion simulation and system integration of robotic fish with modular undulating fin. *International Journal of Simulation* 7 (8), 64-77.
- Clark, R. P., Smith A. J., (2006) Thrust production and wake structure of a batoid-inspired oscillating fin, *Journal of Fluid Mechanics* 562, pp. 415-429.
- Lamas, M. I., Rodríguez, J. D., Rodríguez, C. G., González, P. B., Design aspects and two-dimensional CFD simulation of a marine propulsor based on a biologically-inspired undulating movement. *Journal of Maritime Research*, vol. 7, No. 2, pp. 73-87, 2010.
- Rodríguez, J., González, P., Couce, A., González, G., (2009) Diseño de sistema de propulsión ondulante. *Proceedings of XIII International Congress on Project Engineering, June, Badajoz, Spain, pp. 1961-1972.*
- Versteeg H K, Malalasekera W. *An introduction to computational fluid dynamics: the finite volume method*. 2<sup>nd</sup> edition. Harlow: Pearson Education, 2007. 503p. ISBN 978-0-13-127498-3.
- Fluent 6.3 Documentation, 2006, Fluent Inc.
- Deng, J., Shao, X. M., Ren, A. L., (2005), Numerical study on propulsive performance of fish-like swimming foils, *Journal of Hydrodynamics*, Ser. B 18(6), pp. 681-687.

#### CONTACT WITH THE AUTHORS

Lamas M. I., Assoc. Prof.  
 Rodríguez J. D., Assoc. Prof.  
 Rodríguez C. G., M. Sc.  
 González P. B., Prof.

Escola Universitaria Politécnica. Universidade da Coruña.  
 Avda. 19 de Febreiro s/n - 15405 Ferrol - A Coruña. Spain.  
 e-mail: isabellamas@udc.es

# The Added Mass Coefficient computation of sphere, ellipsoid and marine propellers using Boundary Element Method

**Hassan Ghassemi**, Assoc. Prof.  
Amirkabir University of Technology  
**Ehsan Yari**, M. Sc.  
Malekashtar University of Technology

## ABSTRACT

*Added mass is an important and effective dynamic coefficient in accelerating, non uniform motion as a result of fluid accelerating around a body. It plays an important role, especially in vessel roll motion, control parameters as well as in analyzing the local and global vibration of a vessel and its parts like propellers and rudders. In this article, calculating the Added Mass Coefficient has been examined for a sphere, ellipsoid, marine propeller and hydrofoil; using numerical Boundary Element Method. Since an Ellipsoid and a sphere have simple geometric shapes and the Analytical values of their added mass coefficients are available, so that the results of added mass matrix are obtained and evaluated, using the boundary element method. Then the added mass matrix is computed in a given geometrical and flow specifications for a specific propeller and its results are studied versus experimental results, which it's current numerical data In comparison with other numerical methods has a good conformity with experimental results. The most important advantage of the method in determining the added mass matrix coefficients for the surface and underwater vessels and the marine propellers is extracting all the added mass coefficients with very good Accuracy, while in other numerical methods it is impossible to extract all the coefficients with the Desired Accuracy.*

**Key words:** Added mass coefficient; Boundary element method; Marine propeller; Ellipsoid

## INTRODUCTION

In fluid mechanics, added mass or virtual mass, is the added inertia to the system, owing to that the Increase or decrease in the body acceleration should cause the Fluid to move around the body in such a way that the object can move through it, because the body and the fluid cannot simultaneously occupy this physical space. For simplicity this can be modeled in such a way that the Volume of fluid moves along the object, While in fact all parts of the fluid move with varying degrees. Added mass coefficient matrix usually is expressed as a dimensionless value which is equal to added mass coefficient divided by the Mass of displaced fluid. For example the body density can be considered in the body volume. In general, the added mass coefficient is a second order tensor that depends on the fluid acceleration vector in order to obtain force vector on the body.

The added mass was considered as the first time in 1776 by Dubua who did laboratory studies on spherical pendulum in low swings. [2] Precise mathematical equations for the added mass of sphere, was obtained by Green (1833) and Stokes (1843) respectively. Stokes, also studied on the sphere motions in a finite volume of fluid. Later, following the efforts of many researchers, the concept of added mass was generalized for moving a desired object in different flow regimes. [3]

## THE ADDED MASS COEFFICIENT RELATIONS

The hydrodynamic forces and moments are determined by fluid inertia and viscous properties according to the motion of a body in real incompressible fluid. Definitely, the other forces and moments can be calculated by obtaining one of the inertia or viscous terms. Since the fluid can be assumed as an ideal one (Inviscid). Therefore the inertia forces and moments can be calculated with this estimate. The forces and moments of inertia can be introduced as the body added mass terms, using this method.

Assume that the body with surface  $S$  is moving in an infinite homogeneous ideal Fluid. Consider two systems of coordinates: the stationary one (We denote it by  $XYZ$ ) and the coordinate system moving together with the body (We denote it by  $Oxyz$ ). The vortex-free condition implies the existence of a potential  $\phi(X, Y, Z, t)$ , assuming that the moment of these two systems of coordinate are specified. So the components of the fluid velocity are defined as follows:

$$v_x = \frac{\partial \phi}{\partial X} ; v_y = \frac{\partial \phi}{\partial Y} ; v_z = \frac{\partial \phi}{\partial Z} \quad (1)$$

Using the continuity and incompressibility of fluid and due to the vortex-free condition as mentioned above the Laplace equation is implied as follows:

$$\frac{\partial^2 \phi}{\partial X^2} + \frac{\partial^2 \phi}{\partial Y^2} + \frac{\partial^2 \phi}{\partial Z^2} = 0 ; \nabla^2 \phi = 0 \quad (2)$$

The boundary conditions for Eq. (2) look as follows:

1. The watertight condition, valid on the surface S:

$$\frac{\partial \phi}{\partial \mathbf{n}} \Big|_S = \mathbf{u}_n \quad (3)$$

Where  $\left(\frac{\partial \phi}{\partial \mathbf{n}}\right)_S = \mathbf{u}_n$  is a projection of fluid velocity on the (external) direction  $\mathbf{n}$ , which is normal to surface S;  $\mathbf{u}_n$  is the velocity projection of a point of the body, normal to surface  $\mathbf{n}$ .

2. Stationary condition at infinity:

$$\lim_{r \rightarrow \infty} \frac{\partial \phi}{\partial X} = \lim_{r \rightarrow \infty} \frac{\partial \phi}{\partial Y} = \lim_{r \rightarrow \infty} \frac{\partial \phi}{\partial Z} = 0 \quad (4)$$

Where  $r^2 = X^2 + Y^2 + Z^2$  ( $r$  is the distance from the origin to a fluid point). The function  $\phi$  vanishes at infinity as  $1/r^2$ , whereas its first-order coordinate derivatives vanish as  $1/r^3$  [4, 5]

From the formulation of the problem (1-4) it is seen that the function  $\phi$  depends on time  $t$  via the boundary condition of right-hand side equation (3), so the boundary condition is investigated specifically. The origin  $O$  is chosen to coincide with an arbitrary point of the body

The velocity of the point  $O$  is Denoted by  $\vec{u}_0$  (components  $u_{0x}, u_{0y}, u_{0z}$  are projections of the vector  $\mathbf{u}_0$  on coordinate axes attached to the body).

The angular velocity of the body with respect to the point  $O$  is also denoted by  $\vec{\omega}$  (components of  $\vec{\omega}$  in the same coordinate system are denoted by  $\omega_x, \omega_y, \omega_z$ ). Thus, the velocity of an arbitrary point of the body, including any point of its surface S, is determined by the following equation:

$$\vec{u} = \vec{u}_0 + \vec{\omega} \times \vec{r} \quad (5)$$

Where  $\vec{r}$  is the vector, determining the position of the point. The components of Eq. (5) look as follows:

$$\begin{aligned} u_x &= u_{0x} + \omega_y Z - \omega_z Y \\ u_y &= u_{0y} + \omega_z X - \omega_x Z \\ u_z &= u_{0z} + \omega_x Y - \omega_y X \end{aligned} \quad (6)$$

On the surface S we have:

$$\mathbf{u}_n = u_x \cos(n, x) + u_y \cos(n, y) + u_z \cos(n, z) \quad (7)$$

Writing:  $\alpha \equiv \cos(n, x)$ ;  $\beta \equiv \cos(n, y)$ ;  $\gamma \equiv \cos(n, z)$  and substituting (6) into (7), the following form of the boundary condition is obtained (3):

$$\begin{aligned} \frac{\partial \phi}{\partial \mathbf{n}} \Big|_S = \mathbf{u}_n &= u_{0x} \alpha + u_{0y} \beta + u_{0z} \gamma + \omega_x (\gamma \gamma - z \beta) + \\ &+ \omega_y (z \alpha - x \gamma) + \omega_z (x \beta - y \alpha) \end{aligned} \quad (8)$$

In the formula (8) the variables  $\alpha, \beta, \gamma, \gamma \gamma - z \beta, z \alpha - x \gamma, x \beta - y \alpha$  are determined only based on the shape of the body surface. The body motion and the dynamics of the flow are determined by the functions  $u_{0x}, u_{0y}, u_{0z}, \omega_x, \omega_y, \omega_z$ . The potential  $\phi$  is represented as follows, due to the Linearity of the problem.

$$\phi = u_{0x} \phi_1 + u_{0y} \phi_2 + u_{0z} \phi_3 + \omega_x \phi_4 + \omega_y \phi_5 + \omega_z \phi_6 \quad (9)$$

In the above equation  $\phi_i, i = 1, 2, 3$  are the flow potentials corresponding to the body moving along the axes  $x, y, z$  at unit linear velocities, respectively. On the other hand  $\phi_i, i = 4, 5, 6$  are potentials, corresponding to rotation of the body around the same axes at unit angular velocities respectively. It is seen that the body motion in an ideal infinite fluid causes to solve six problems. The first problem can be formulated as follows: the solution of the Laplace equation  $\Delta \phi_1 = 0$  will be found, using the following boundary conditions:

$$\frac{\partial \phi_1}{\partial \mathbf{n}} = \alpha \quad (10)$$

$$\frac{\partial \phi_1}{\partial X} + \frac{\partial \phi_1}{\partial Y} + \frac{\partial \phi_1}{\partial Z} \rightarrow 0 \text{ as } r \rightarrow \infty \quad (11)$$

The function  $\frac{\partial \phi_1}{\partial \mathbf{n}} = \alpha$  is given on the surface S and The last (sixth) problem, taking (8) into account. To solve the problem, considering the Laplace equation  $\Delta \phi_6 = 0$  using the following boundary conditions:  $\frac{\partial \phi_6}{\partial \mathbf{n}} = x \beta - y \alpha$  which is given at the surface S, so:

$$\frac{\partial \phi_6}{\partial X} + \frac{\partial \phi_6}{\partial Y} + \frac{\partial \phi_6}{\partial Z} \rightarrow 0 \text{ as } r \rightarrow \infty$$

It can be seen that the function  $\phi_i, i = 1, 2, \dots, 6$  does not depend on  $u_0$  and  $\omega_0$ . These functions are determined only by the shape of the surface S of the body and Choice of coordinate system Oxyz attached to the body.

## KINETIC ENERGY OF THE FLUID

In order to obtain fluid kinetic energy, considering the surface S and the sphere  $\Sigma$  of radius  $a$  including the body with surrounding Fluid, the following integral is defined.

$$T = \frac{1}{2} \rho \iiint_V v^2 dV = \quad (12)$$

$$= \frac{1}{2} \rho \iiint_V \left[ \left( \frac{\partial \phi}{\partial x} \right)^2 + \left( \frac{\partial \phi}{\partial y} \right)^2 + \left( \frac{\partial \phi}{\partial z} \right)^2 \right] dx dy dz$$

Where  $\rho$ , is the fluid Density

Using Green's transformation for two functions ( $\phi_1, \phi_2$ ):

$$\begin{aligned} &\iiint_V \left( \frac{\partial \phi_1}{\partial x} \frac{\partial \phi_2}{\partial x} + \frac{\partial \phi_1}{\partial y} \frac{\partial \phi_2}{\partial y} + \frac{\partial \phi_1}{\partial z} \frac{\partial \phi_2}{\partial z} \right) dx dy dz = \\ &= - \iint_{S+\Sigma} \phi_1 \frac{\partial \phi_2}{\partial \mathbf{n}} dS - \iiint_V \phi_1 \left( \frac{\partial^2 \phi_2}{\partial x^2} + \frac{\partial^2 \phi_2}{\partial y^2} + \frac{\partial^2 \phi_2}{\partial z^2} \right) dx dy dz \end{aligned} \quad (13)$$

And considering  $\phi_1 = \phi_2 = \phi, \Delta \phi = 0$  and putting words in the above equation the following expression is gotten:

$$T = - \frac{\rho}{2} \iint_S \phi \frac{\partial \phi}{\partial \mathbf{n}} dS - \frac{\rho}{2} \iint_{\Sigma} \phi \frac{\partial \phi}{\partial \mathbf{n}} dS \quad (14)$$

The Second term in the right hand side of Eq. (14) tends to zero as  $a \rightarrow \infty$  according to the asymptotic behavior of  $\phi$  and its first derivatives while  $r \rightarrow \infty$ . Therefore, the following formula is obtained for the total kinetic energy of the fluid around the surface S:

$$T = - \frac{\rho}{2} \iint_S \phi \frac{\partial \phi}{\partial \mathbf{n}} dS \quad (15)$$

Substituting the expression (9) in to (15) and writing:

$$\begin{aligned} u_{0x} &= u_1, u_{0y} = u_2, u_{0z} = u_3, \\ \omega_x &= u_4, \omega_y = u_5, \omega_z = u_6 \end{aligned}$$

The expression (16) is finally obtained:

$$T = \frac{1}{2} \sum_{i=1}^6 \sum_{k=1}^6 \lambda_{ik} u_i u_k \quad (16)$$

Where  $\lambda_{ik}$  is:

$$\lambda_{ik} = -\rho \iint_S \frac{\partial \phi_i}{\partial n} \phi_k dS \quad (17)$$

$\lambda_{ik}$  is called the added mass of the body.

According to Eq. (17) it is found that the added mass, do not depend on the body velocity and Kinematics of the motion but is only a function of the body surface geometry.

Applying Green's formula to functions  $\phi_i$  and  $\phi_k$  in the volume  $V$  between the surfaces  $\Sigma$  and  $S$  then:

$$\begin{aligned} & \iiint_V (\phi_i \Delta \phi_k - \phi_k \Delta \phi_i) dV = \\ & = \iint_{\Sigma} \left( \phi_i \frac{\partial \phi_k}{\partial n} - \phi_k \frac{\partial \phi_i}{\partial n} \right) dS - \iint_S \left( \phi_i \frac{\partial \phi_k}{\partial n} - \phi_k \frac{\partial \phi_i}{\partial n} \right) dS \end{aligned} \quad (18)$$

Since  $\Delta \phi_i = \Delta \phi_k = 0$ , so that the left-hand side of the equation equals zero, and the first term of the right-hand side of the equation tends to zero at  $\alpha \rightarrow \infty$ . Therefore, the condition for the infinite fluid surrounding the body is as follows:

$$\iint_S \phi_i \frac{\partial \phi_k}{\partial n} dS = \iint_S \phi_k \frac{\partial \phi_i}{\partial n} dS \quad (19)$$

Since  $\lambda_{ik} = \lambda_{ki}$ . Therefore, only 21 values out of 36  $\lambda_{ik}$  ( $i, k = 1, 2, \dots, 6$ ) are independent.

This part, in fact proved that the added mass matrix is symmetric.

To obtain the added mass coefficient matrix using force view, ultimately the same formula is achieved. [6]

## CALCULATING THE ADDED MASS COEFFICIENT USING THE BOUNDARY ELEMENT METHOD

Boundary element method is based on the Green's theory. Based on the theory solving the fluid flow around the body can be transferred from the volume solving domain around the body to the body boundary that is performed on the produced surface elements in three-dimensional modes. The boundary element method is used to obtain all six unit potentials corresponding to the six free degrees. The added mass tensor can be computed, obtaining the unit potential. The forces and momentum also can be achieved, having the added mass. [7]

$$\int_{\Omega} \nabla \cdot u d\Omega = \int_{\Gamma} u \cdot n ds \quad (20)$$

## THE BOUNDARY ELEMENT METHOD TO COMPUTE THE ADDED MASS COEFFICIENT

Consider the Closed area  $\Omega$ , the boundary  $S$  and unit vector  $\vec{n}$  normal to  $S$  (Fig. 1). The boundary  $S$  is composed of the body wetted surface  $S_B$ , the wake surface  $S_W$  and the external control surface  $S_{\infty}$  including surface area  $S_B, S_W$ .

The  $\Omega$  encountered the Uniform inflow velocity  $\vec{V}_I$ , assuming the flow is Incompressible, Inviscid and Irrotational in the domain  $\Omega$ , in the upstream flow.

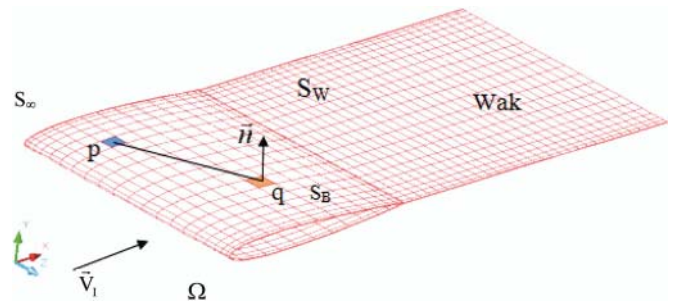


Fig. 1. Application of Green theory for hydrofoils

With these assumptions, the flow field around the body can be identified using Perturbation Velocity potential  $\phi$ , which satisfies the Laplace equation:

$$\nabla^2 \phi = 0 \quad (21)$$

To solving the problem, the boundary conditions are considered as follows:

### Kinematic Boundary Condition

Based on the Kinematic boundary condition, the Flow velocity normal to the body surface must be zero.

$$\frac{\partial \Phi}{\partial n} = 0 \rightarrow \frac{\partial \phi}{\partial n} = -\vec{V}_I \cdot \vec{n} \quad (22)$$

Where  $\vec{n}$ , is the unit vector normal to outside of the boundary [8] and is changed as follows, considering the unit potential Kinematic of Boundary Condition:

$$\frac{\partial \phi_j}{\partial n} \Big|_{j=1 \rightarrow 6} = \begin{cases} n_i \Big|_{i=1 \rightarrow 3}^{j=1 \rightarrow 3} \\ (r \times n_i) \Big|_{i=1 \rightarrow 3}^{j=4 \rightarrow 6} \end{cases} \quad (23)$$

Where,  $r$  is a vertical distance from a fixed origin point [12].

### Kinematic And Dynamic Conditions In Wake

Based on this condition, there is no velocity jump of flow on the wake vortex, however there is velocity jump of potential on the surface which is equal to circulation  $\Gamma$  around the fin. The mathematical relations of flow velocity and potential are expressed as follows:

$$\begin{aligned} (\Delta \phi)_{on S_w} &= \phi^B - \phi^F = \Gamma \\ (\Delta \frac{\partial \phi}{\partial n}) &= (\frac{\partial \phi}{\partial n})^B - (\frac{\partial \phi}{\partial n})^F = 0 \end{aligned} \quad (24)$$

Where B and F showing back and face sides of the propeller [8].

### KUTTA CONDITION IN THE TRAILING EDGE

Hess and Smith have shown that the flow passing along a thin and non lifting body can be described by the distribution singularities of source. But to describe the flow passing along lifting bodies, modeled by the circulation distribution on the surface, a boundary condition for the Trailing Edge of the body must be satisfied, expressing that the velocity at the trailing edge should be limited and unique. [9, 10]

$$|\nabla \phi|_{TE} < 0 \quad (25)$$

## Surface At Infinity

At the boundary surface at infinity  $S_\infty$ , the perturbation velocity due to the body surface must tend to zero.

$$\nabla\phi \rightarrow 0 \text{ as } S_\infty \rightarrow 0 \quad (26)$$

Using Green's theory, general answers of the Laplace equation for each point P can be expressed as the following integral equation:

$$4\pi\phi(P) = \iint_{S_B} \phi(q) \frac{\partial}{\partial n_q} \left( \frac{1}{R(p,q)} \right) ds + \iint_{S_W} \Delta\phi(q) \frac{\partial}{\partial n_q} \left( \frac{1}{R(p,q)} \right) ds - \iint_{S_B} \frac{\partial\phi}{\partial n_q} \left( \frac{1}{R(p,q)} \right) ds \quad (27)$$

In the above equation  $\partial\phi/\partial n$  is determined, using the boundary condition of Eq (23).  $1/R(p, q)$ , is the distance between p and q, so that the only remaining unknown for solving Eq (27) is  $\phi$ . [8]

## EQUATIONS DISCRETIZATION

In order to solve Eq (27), the equation form must be discrete and the body boundary surface shall be made of tetragonal elements.

Fractional equations lead to linear algebraic equation system for  $\phi$  and i as follows:

$$2\pi\phi_i = \sum_{j=1}^N D_{ij}(\phi_j) + \sum_{j=1}^{N_R} \sum_{l=1}^{N_W} W_{ijl}(\Delta\phi)_l + \sum_{j=1}^N S_{ij} \left( \frac{\partial\phi}{\partial n} \right)_j \quad i = 1, 2, \dots, N_{tot} \quad (28)$$

Where  $D_{ij}$ ,  $S_{ij}$ , and  $W_{ijl}$  are Dipole coefficients and source for j element that acts on the arithmetic point i. The coefficients are defined as follows:

$$D_{ij} = \sum_{k=1}^k \left[ \iint_{S_B} \frac{\partial}{\partial n_j} \left( \frac{1}{R_{ij}} \right) ds_j \right]_k \quad \text{on } S_B$$

$$W_{ijl} = \sum_{k=1}^k \left[ \iint_{S_W} \frac{\partial}{\partial n_j} \left( \frac{1}{R_{ij}} \right) ds_j \right]_k \quad \text{on } S_W \quad (29)$$

$$S_{ij} = \sum_{k=1}^k \left[ \iint_{S_B} \left( \frac{1}{R_{ij}} \right) ds_j \right]_k \quad \text{on } S_B$$

To obtain these coefficients the numerical solution of the integrals is used. Calculating these coefficients, the following matrix equation is formed

Solving the equations using the Gauss - Sydl method is done as a repetitive solving, so that  $\phi_j$  are obtained. [11]

$$[D][\phi] = [S] + [W][\Delta\phi] \quad (30)$$

Where:

[D] = dipole Potential effects of induction coefficient matrix  
[S] = source Potential effects of induction coefficient matrix  
[W] = dipole Potential effects of induction coefficient matrix

For lifting and non-lifting bodies, the above computational method can be used, but the difference is in the use of Kutta boundary condition which there is no need to consider it in non-lifting bodies, so that the results are obtained directly regarding the kinematic boundary condition.

Although the Kutta condition is considered to analyze the propeller and the hydrofoil, the obtaining results have no significant difference with the ones which are obtained without considering the Kutta condition. So, regarding this issue it can be expressed that only the D and S out of the D, S and W are important for calculating the added mass matrix.

$$D_{ij} = \sum_{k=1}^k \left[ \iint_{S_B} \frac{\partial}{\partial n_j} \left( \frac{1}{R_{ij}} \right) ds_j \right]_k \quad \text{on } S_B \quad (31)$$

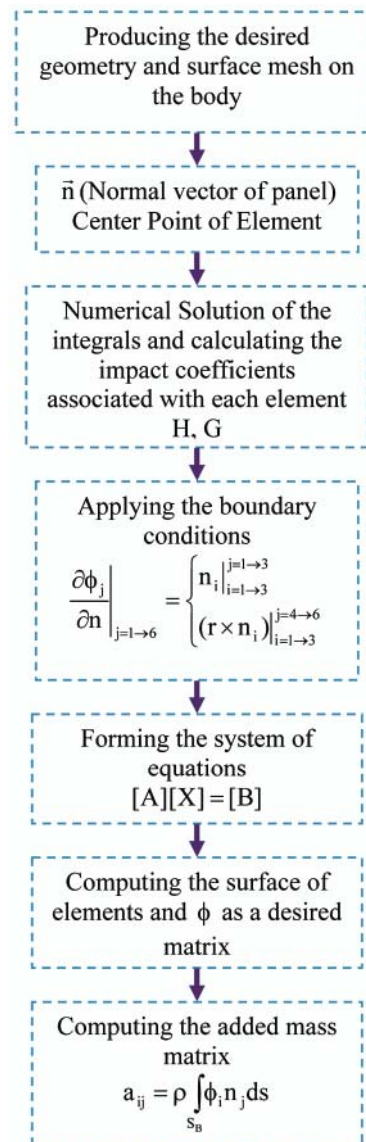
$$S_{ij} = \sum_{k=1}^k \left[ \iint_{S_B} \left( \frac{1}{R_{ij}} \right) ds_j \right]_k \quad \text{on } S_B$$

Which in Reference 12, the integrals are expressed as follows that in fact are the same general term in Eq (27) and with extracting the D and S, the formulas in Eq (31) is obtained.

$$\int_{S_B} \left[ \frac{1}{R} \frac{\partial\phi}{\partial n} \right] dS = \sum_{\substack{K=1 \\ K \neq i}}^N \left. \frac{1}{R} \frac{\partial\phi_j}{\partial n} \right|_{j=1 \rightarrow 6} \delta S_K \quad (32)$$

$$\int_{S_B} \left[ \phi \frac{\partial}{\partial n} \left( \frac{1}{R} \right) \right] dS = \sum_{\substack{K=1 \\ K \neq i}}^N \left[ \frac{\partial}{\partial n} \left( \frac{1}{R} \right) \right] \delta S_K + 2\pi\phi_{i=K}$$

## The Flowchart Of The Added Mass Matrix Extraction Using The Boundary Element Method



If the above integrals are formulated based on matrix equations, the following relation is obtained:

$$[A_{iK}][\phi_K] = [B_i] \quad (33)$$

So that  $i = K$  and  $A_{iK} = 2\pi$ .

The added mass matrix values with solving matrix equations for all six potential unit functions can be defined as follows:

$$\mu_{iK} = \rho \int_{S_B} \phi_i n_K dS_B \quad (34)$$

If the above equation is written in the matrix form, which is the general form of added mass matrix. [12]:

$$\text{Added Mass Matrix} = \begin{bmatrix} \sum_{i=1}^N \phi_1^i n_1^i \delta S_i & \sum_{i=1}^N \phi_1^i n_2^i \delta S_i & \dots & \sum_{i=1}^N \phi_1^i (r \times n)_3^i \delta S_i \\ \sum_{i=1}^N \phi_2^i n_1^i \delta S_i & \sum_{i=1}^N \phi_2^i n_2^i \delta S_i & \dots & \sum_{i=1}^N \phi_2^i (r \times n)_3^i \delta S_i \\ \dots & \dots & \dots & \dots \\ \sum_{i=1}^N \phi_6^i n_1^i \delta S_i & \sum_{i=1}^N \phi_6^i n_2^i \delta S_i & \dots & \sum_{i=1}^N \phi_6^i (r \times n)_3^i \delta S_i \end{bmatrix}$$

## RESULTS

### Computing The Added Mass Coefficient Of Sphere

The added mass coefficient for a sphere of radius 0.25 m has been investigated in this part. However, according to the

analytical relations in the mass matrix of sphere, only  $a_{11}$ ,  $a_{22}$  and  $a_{33}$  have values and the others are zero. The three coefficients are equal with each other and should be equal to half of the sphere mass. In order to evaluate the Mesh independency, the added mass matrix were investigated for three cases of surface element (2400, 3360 and 4800 elements), using the boundary element numerical code and the obtained results and errors were checked.

The obtained values for the added mass of the sphere using numerical analysis of the boundary element are as follows:

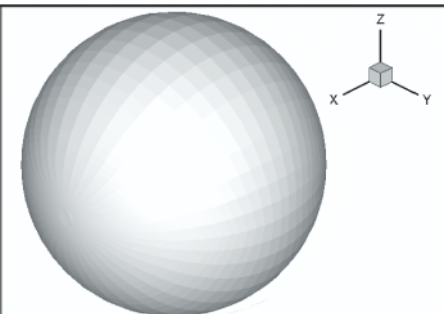
Added Mass Matrix =

$$= \begin{bmatrix} 0.032752 & 0 & 0 & 0 & 0 & 0 \\ 0 & 0.032753 & 0 & 0 & 0 & 0 \\ 0 & 0 & 0.032753 & 0 & 0 & 0 \\ 0 & 0 & 0 & 0 & 0 & 0 \\ 0 & 0 & 0 & 0 & 0 & 0 \\ 0 & 0 & 0 & 0 & 0 & 0 \end{bmatrix}$$

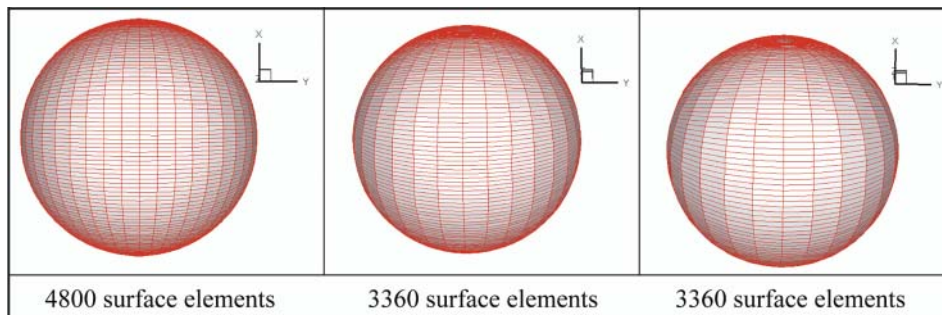
For a sphere with radius of 0.25 m, the analytical values of  $a_{11}$ ,  $a_{22}$ ,  $a_{33}$  are equal to 0.0327245

As it was mentioned, only  $a_{11}$ ,  $a_{22}$ ,  $a_{33}$  have non-zero value, which is equal to half of the sphere mass and the other elements of the added mass matrix are zero. So it can be seen that the obtained values of the numerical boundary element method have a high conformity with the analytical data and the error rate, according to the table (3) is the 10E-2 order. [6]

Tab. 1. Geometric and flow data to calculate the added mass coefficient of sphere

Radius = 0.25 Volume (Numerical) = 0.065449 Volume (Exact) = 0.0654498 Fluid = Water Density = 1000 kg/m <sup>3</sup>	
---	--

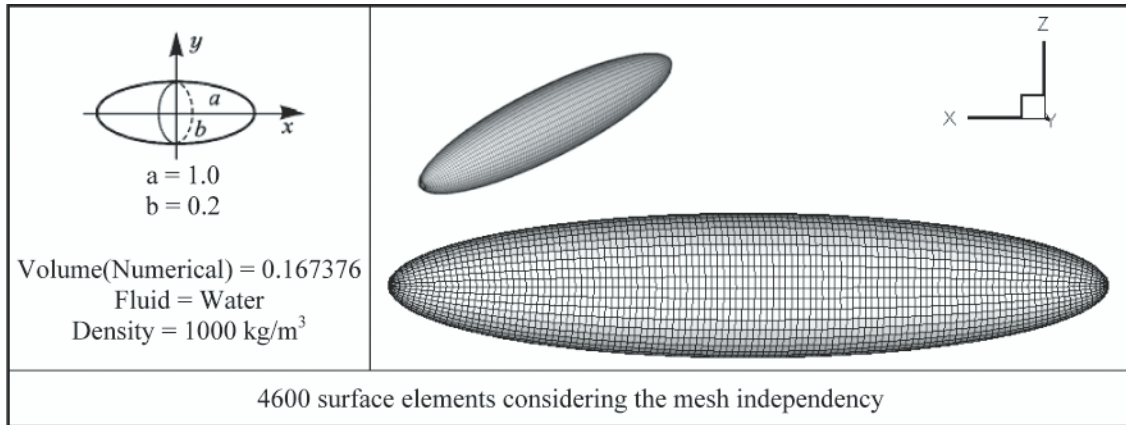
Tab. 2. Showing the produced geometry with surface elements to check the mesh independency condition



Tab. 3. The compared Results of the added mass numerical and analytical data of the sphere and the Error percentage Due to the elements numbers

Number of Element	Numerical result for $a_{11}$ (code result)	Analytical value of $a_{11}$	Difference between Numerical and Analytical result	% Error $\left( \frac{a_{11}(\text{Num}) - a_{11}(\text{Anal})}{a_{11}(\text{Num})} \right) \times 100$
2400	0.032814	0.032725	8.95E-05	0.272749
3360	0.032771	0.032725	4.65E-05	0.141894
4800	0.032752	0.032725	2.75E-05	0.083964

Tab. 4. Geometric and flow data of computing the added mass coefficient ellipsoid



### Computing The Added Mass Of Ellipsoid

Continue the contex, the coefficient of added mass for an ellipsoid has been investigated.

Since the added mass coefficients of ellipsoid as well as the sphere are available in references, so that to validate the computing results of the boundary element code, this analysis is given. The numerical analysis with the mesh independency condition was investigated and the results of the surface element with the number of 4600 had very little error in comparison with the existing data.

The added mass matrix obtained by numerical analysis for an ellipsoid with the above specification is as follows:

Added Mass Matrix =

$$= \begin{bmatrix} 0.009025 & 0 & 0 & 0 & 0 & 0 \\ 0 & 0.143401 & 0 & 0 & 0 & 0 \\ 0 & 0 & 0.143401 & 0 & 0 & 0 \\ 0 & 0 & 0 & 0 & 0 & 0 \\ 0 & 0 & 0 & 0 & 0.030467 & 0 \\ 0 & 0 & 0 & 0 & 0 & 0.030467 \end{bmatrix}$$

Considering that the numerical analysis results of the added mass were dimensional and the results in the references were dimensionless, then to validate the results, the data obtained from the numerical analysis were transformed to dimensionless one and compared with the available data in those references. To make the added mass matrix of ellipsoid dimensionless  $a_{11}$ ,  $a_{22}$  and  $a_{33}$  shall be divided on  $(4\pi/3)ab^2$  and also  $a_{44}$ ,  $a_{55}$  and  $a_{66}$  must be divided on  $(4\pi/15)ab^2(a^2 + b^2)$ .

Due to the symmetry of the ellipsoid, then  $a_{22} = a_{33}$ ,  $a_{55} = a_{66}$  and  $a_{44} = 0$ .

According to data obtained from the Diagram and making them dimensional, then:

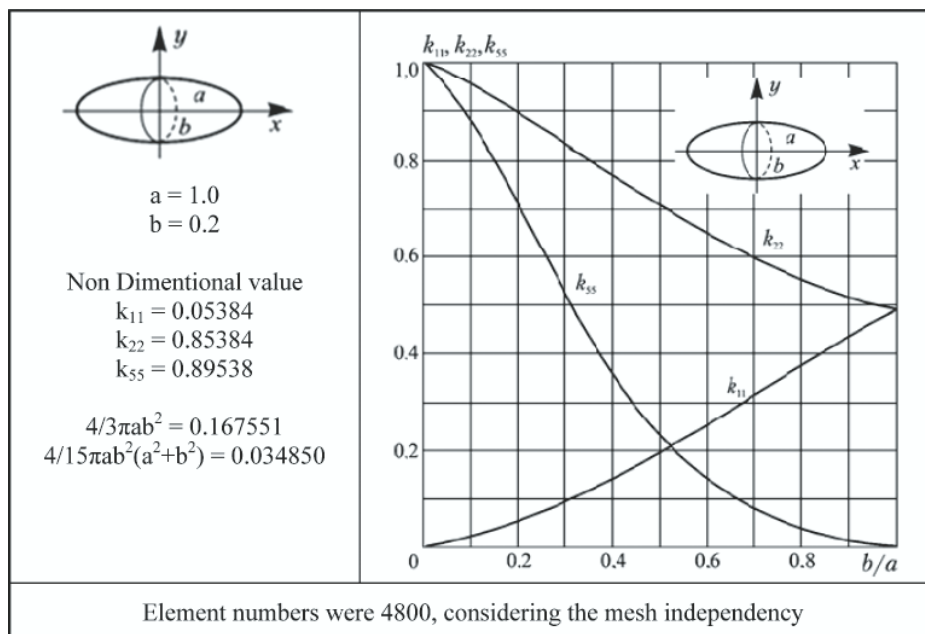
$$a_{11} = K_{11} \times \frac{4\pi}{3} ab^2$$

$$a_{22} = a_{33} = K_{22} \times \frac{4\pi}{3} ab^2$$

$$a_{55} = a_{66} = K_{55} \times \frac{4\pi}{15} ab^2 (a^2 + b^2)$$

It is found from comparing the boundary element numerical analysis results with the data available in references for added mass coefficients of ellipsoid that there is a good conformity between the numerical data and the ones in the references [6, 12].

Tab. 5. The added mass coefficient Diagram of an ellipsoid [6]



Tab. 6. the compared Results of the added mass numerical and analytical data of the ellipsoid and the Error percentage Due to the elements numbers

Matrix array	Numerical result (code result)	Analytical result	Difference between Numerical and Analytical result	% Error $(\frac{a_{11(Num)} - a_{11(Anal)}}{a_{11(Num)}}) \times 100$
A <sub>11</sub>	0.009025	0.00902094	4.06E-06	0.044986
A <sub>22</sub>	0.143401	0.14306174	0.000339	0.236581
A <sub>55</sub>	0.030467	0.03120399	-0.00074	-2.41898

### Computing The Added Mass Matrix For A Sample Propeller

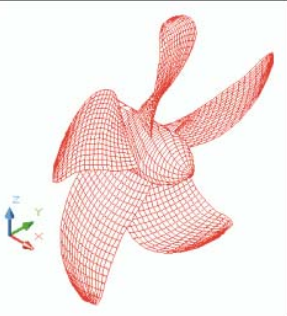
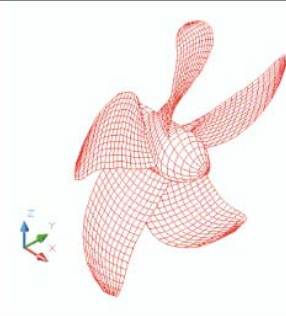
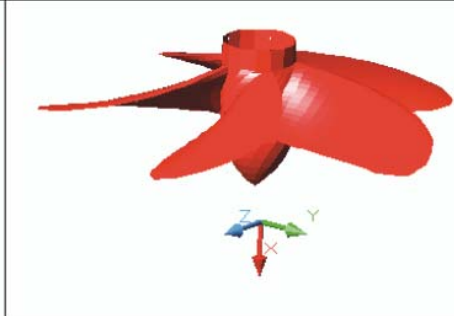
According to the data and results obtained for the added mass matrix of the sphere and ellipsoid it can be found that there is a very good accuracy between the data obtained from the analytical and the numerical solution, suggestive of the validity of the boundary element method code in calculating the added mass matrix. The following text is about computing the added mass matrix for a sample propeller which its experimental and geometrical data is on hand and the results have been validated with the experimental data. The added mass matrix, considering what was mentioned in the text do not depends on the body velocity and is only a function of the body geometry.

First of all, the existing Geometric data of the propeller was considered based on the standards and the propeller geometry modeled with a very high accuracy. Then the propeller surface and the hub were analyzed according to the flow conditions. The propeller analysis was performed in several different modes of surface element numbers so that the most appropriate numbers of the elements is achieved in a way that the obtained answers do not depend on the element numbers [14].

Tab. 7. Geometric and flow data related to the propeller and the produced geometry for boundary element numerical analysis [13]

Property	Value	
Type	FPP	
No. of Blades, Z	5	
Section Type	NACA66	
Skew	21.150 deg	
Hub Ratio, H/D	0.170	
Pitch Ratio, P/D	0.671	
Expanded Area Ratio	0.595	
Advance Ratio, J	0.4489	
Diameter, D (m)	0.25	
Material	ALBC3	
Young's Modulus, E (GPa)	73	
Shear Modulus, G (GPa)	28	
Material Density, ρp (kg/m3)	2,800	
Water Density, ρw (kg/m3)	1,000	
Revolution Speed, n (rpm)	487.4	

		
---	---	--

### Dimensional Added Mass Matrix Obtained For The Propeller

$$\text{Added Mass Matrix} = \begin{bmatrix} 2.176192 & -0.240440 & -0.686280 & -0.670630 & 0.015638 & -0.196440 \\ -0.240440 & 0.042111 & 0.080637 & 0.006256 & 0.000156 & 0.018995 \\ -0.686280 & 0.080637 & 0.251128 & 0.019366 & -0.005240 & 0.059255 \\ -0.058640 & 0.006256 & 0.019366 & 0.001617 & -0.000450 & 0.005282 \\ 0.015638 & 0.000156 & -0.005240 & -0.000450 & 0.000505 & -0.001630 \\ -0.196440 & 0.018995 & 0.059255 & 0.005282 & -0.001630 & 0.018315 \end{bmatrix}$$

Tab. 8. Compared results of the added mass numerical and analytical data of the propeller and the Error percentage Due to the element numbers

Number of Element	Numerical result Matrix Array $A_{13}$ (Addedprop code)	Experimental Result	Difference between Numerical and Experimental result	% Error $\left(\frac{a_{11}(\text{Num}) - a_{11}(\text{Anal})}{a_{11}(\text{Num})}\right) \times 100$
1800	0.6242060	0.6860000	-0.0617940	-9.0078717
2520	0.6382161	0.6860000	-0.0477839	-6.9655831
3240	0.6451033	0.6860000	-0.0408967	-5.9616181
3960	0.6510313	0.6860000	-0.0349687	-5.0974781
4320	0.6631462	0.6860000	-0.0228538	-3.3314577
5040	0.6691640	0.6860000	-0.0168360	-2.4542274
5760	0.6706359	0.6860000	-0.0153641	-2.2396647

### Investigating The Mesh Independency

To investigate that the obtained data for the propeller is independent of the produced surface elements of the propeller and the hub surface, the added mass matrix was obtained in seven different numbers of surface elements and the results were checked, as it is identified from the diagram (figure 2) the results do not have any significant change after 3960 elements.

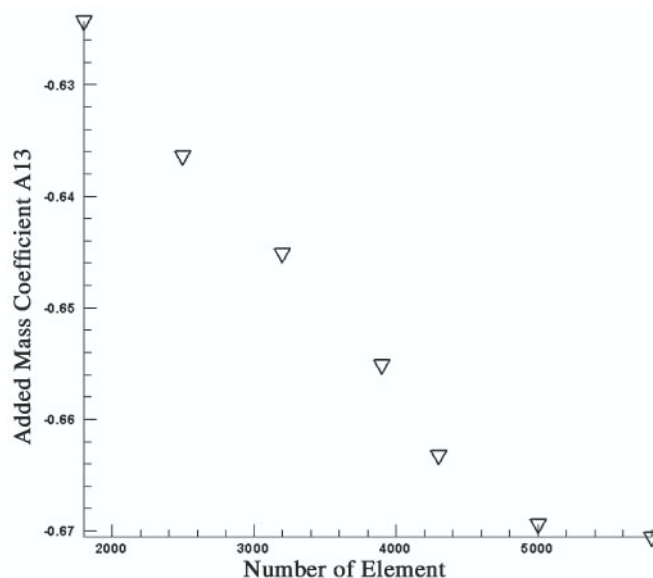


Fig. 2. Changes in the mass added coefficient based on the element numbers at the propeller surface

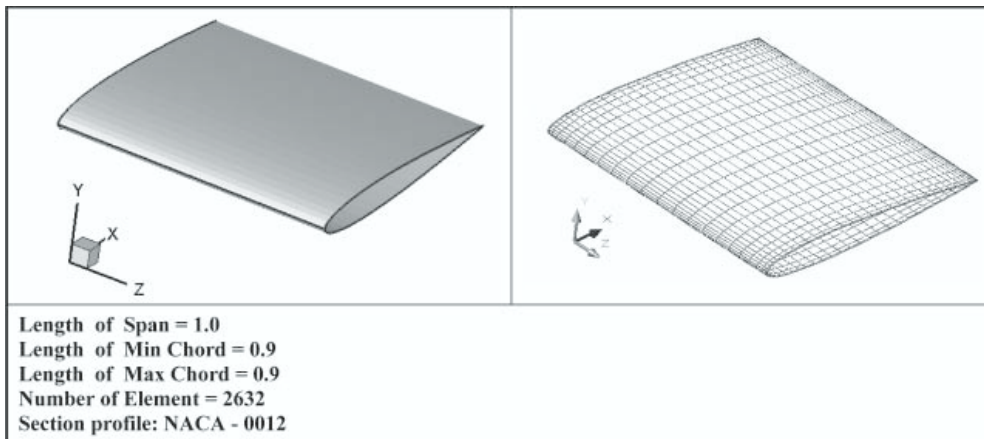
### Comparing The Added Mass Matrix Of The Propeller With The Obtained Data From Other Numerical And Experimental Methods

Tab. 9. Comparing the data, obtained from the numerical solution, experimental and formulated data

Estimation Method	Added Mass (kg)	Diff [%]
Experiment	0.6860000	0.0
AddedProp (Present method)	0.6706359	-2.24%
Prodas	0.6690000	-2.5%
Schwanecke	0.8240000	+20.1%
Shuster	0.9660000	+40.8%

## Computing The Added Mass Matrix Of The Hydrofoil (NACA0012 Section)

Tab. 10. Geometrical data and the element numbers of calculating the added mass coefficient of hydrofoil



### Gradual Increase In The Span Length To Validate The Results

To calculate the added mass matrix of the hydrofoil with NACA0012 section, first of all the mesh independency was investigated in which the obtained data from 2632 elements had very good accuracy, then to validate the obtained data, the span length was increased gradually from 0.2 to 1 and thus the added mass matrix was computed. Afterward the added mass matrix element changes were plotted based on the span length increase. All of the coefficients are increased with linear and non-linear curves of the 2 and 3 order, which is completely ascending. In fact, by increasing the Span length, all coefficients were reasonably increased as expected. Of course, investigating each of the diagrams whether they should be linear or nonlinear, of the 2 orders or 3 orders are denied due to that they are Proportional to Dynamic and Simulation topics.

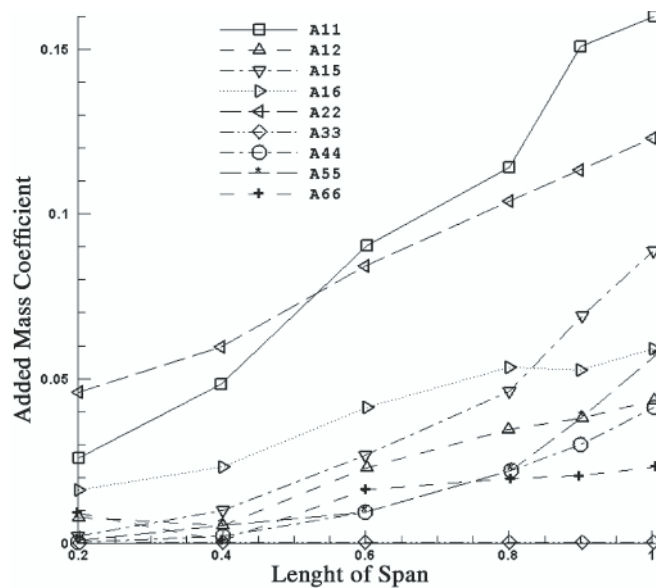


Fig. 3. The added mass coefficient changes of hydrofoil based on the gradually increase along the Span length

### The Added Mass Matrix Of Hydrofoil

The added mass matrix of hydrofoil with NACA0012 section for the Span length of 1 m and Chord length of 9/0 m is as follows:

$$\text{Added Mass Matrix} = \begin{bmatrix} 159.3152 & 31.63824 & 0 & -13.5806 & 89.37951 & 58.75352 \\ 31.63824 & 122.4136 & 0 & -63.4481 & 11.35911 & 44.82613 \\ 0 & 0 & 0 & 0 & 0 & 0 \\ -13.5806 & -63.4481 & 0 & 40.92427 & -7.51047 & -23.5442 \\ 89.37951 & 11.35911 & 0 & -7.51047 & 56.3155 & 21.46682 \\ 58.75352 & 44.82613 & 0 & -23.5442 & 21.46682 & 22.75078 \end{bmatrix}$$

## CONCLUSION

- The added mass coefficient is one of the most important dynamic coefficients in solving dynamic equations and simulating the vessels. Calculating the Add mass coefficient especially the bodies whose shapes are not simple is difficult. Added mass coefficient is extractable using empirical formulas, the simple analytical relations and numerical methods such as Strip theory and lab tests.
- But each of these methods can be used in a limited range. For example, the analysis relations can be used only for simple geometries and lab tests to extract the added mass are costly and obtaining all matrix coefficients is very difficult. Moreover, the numerical methods cannot model the full three-dimensional body and have a lot of errors that ultimately causing a large deviation in calculating the coefficients. Meanwhile since the boundary element method solves the problem on surface boundary elements of the body, it needs less elements and time to solve and can obtain the added mass coefficients owing to modeling the full three-dimensional body and also extracting the potential values with high accuracy.
- As mentioned in the article to investigate the mesh independency, the added mass matrix of an ellipsoid and a sphere of specific geometry were extracted, using the boundary element method and the results were validated with the analytical data.
- Afterward the added mass matrix for a certain propeller was computed which its results had a very good conformity with the experimental ones. However due to lack of access to distribution Cord of the propeller, the standard distribution of Series B for a propeller with specific section (NACAa66) was used, considering that the volume of the produced propeller geometry was checked with the volume of the examined propeller in a way that the geometry would have a high conformity with the existing data so that if the exact geometry is on hand, the error rate with be lower than 10E-2 order.
- To put it in a nut shell, extracting a complete and dimensional add mass matrix with any desired geometry and the accuracy of obtained data is the difference between this method and boundary element code with other numerical methods.

## BIBLIOGRAPHY

1. Newman, John Nicholas: *Marine hydrodynamics*. Cambridge, Massachusetts, MIT Press. ISBN: 0-262-14026-8 §4.13, p. 139, 1977

2. Birkhoff, G.: *Hydrodynamics*. Princeton Univ. Press, Princeton, 1960
3. Lamb, G.: *Hydrodynamics*. Cambridge University Press, Cambridge, 1932
4. Kochin, N.E., Kibel, I.A., Rose, N.V.: *Theoretical Hydromechanics*, Parts I and II. State Publisher of Physical and Mathematical Literature, Moscow, in Russian, 1963
5. Taylor, J.L.: *Some hydrodynamical inertia coefficients*. Phil. Mag. Ser. 7 9(55), 161-183, 1930
6. Alexandr I. Korotkin: *Added mass of ship structure*. Fluid mechanics and its applications, Volume 88, 2009
7. John T. Katsikadelis: *Boundary Elements, Theory and Applications*, Elsevier Science Ltd, 2002
8. Kinnas S.A. and Hsin C.Y.: *Boundary Element Method for the Analysis of the Unsteady Flow around Extreme Propeller Geometry*. IAA, Journal, 30 (3), 1992
9. Hess J.T, Smith A.M.: *Lecture 3 AA200b* January 13-18, 2005
10. Hess J.T, Smith A.M.: *Calculation of nonlifting potential flow about arbitrary three-dimensional bodies*. Journal of Ship Research, 8(2), 1964
11. Morino L. and Kuo C.C.: *Subsonic Potential Aerodynamics for Complex Configuration: A general Theory*. AIAA Journal, 12 (2), 191-197, 1974
12. Olivier Saout.: *Computation of Hydrodynamic Coefficients and Determination of Dynamic Stability Characteristics of an Underwater Vehicle Including Free Surface Effects*. Ms Thesis, Florida Atlantic University, May 2003
13. Young-Joong Kim, Hyun Yup Lee and Chang-Sup Lee: *The Added Mass and Damping for the Axial Rigid Body Motion of a Marine Propeller Rotating in a Uniform Flow*. Journal of the Society of Naval Architects of Korea, Vol. 45, No. 3, pp. 309-314, June 2008
14. Donald M. MacPherson and Vincent R. Puleo and Matthew B. Packard, *Estimation of Entrained Water Added Mass Properties for Vibration Analysis*, SNAME New England Section, June 2007.

---

## CONTACT WITH THE AUTHORS

Hassan Ghassemi, Assoc. Prof.  
Faculty of Marine Technology  
Amirkabir University of Technology  
Hafez Ave.,  
Tehran, IRAN  
e-mail: gasemi@cic.aut.ac.ir

Ehsan Yari, M. Sc.  
Faculty of Marine Engineering,  
Malekashtar University of Technology,  
Shahinshar,  
Isfahan, IRAN

# A method for evaluating durability of porous slide bearings

Piotr Bzura, Ph. D.  
Gdansk University of Technology

## ABSTRACT



*The article presents the structures of porous slide bearing bushes and greasy lubricants, and the similarity criterion resulting from these structures. A physical model is proposed which describes the operation of the porous slide bearing bush taking into account, via analogy, the phenomena taking place in the greasy lubricant nodes instead of those observed in the bush structures.*

*Included are the results of experimental tests of three greasy lubricants which allow transferring the results recorded in model experiments to real objects.*

**Key words:** structure; durability; strength of bonds

## INTRODUCTION

The published data on operating parameters of Diesel engines used in shipbuilding reveal a remarkably slowing increase, or even decrease, of the consumption of lubricating media [17, 18]. This effect results, on the one hand, from ship owners' permanent search for the ways to reduce the cost of operation of the internal combustion engines, and, on the other hand, from increasing pressure toward the reduction of environment pollution caused by those engines [5]. The rationalisation of the use of lubricating media requires delivering them to tribological nodes in optimal volumes and precisely defined time intervals [11, 12].

This need for rationalisation of lubrication is the reason why slide bearings with "limited supervision" are expected to be used in future in marine piston engines. To this group belong, for instance, the bearings with porous bushes. A distinguishing feature of these bearings is their durability, which can be evaluated in laboratory tests using the here presented method.

## DURABILITY OF POROUS SLIDE BEARINGS

The porous slide bearings belong to the group of bearings which do not need lubricating service, and therefore they are frequently called the slide bearings with "limited supervision". The lubricant is not delivered to them from outside, but it is

collected in bush wormholes and is to be periodically refilled. Taking into account the lubricating supervision, a distinction should be made between the porous slide bearings and those with conventional lubrication - Fig. 1 [11, 12].

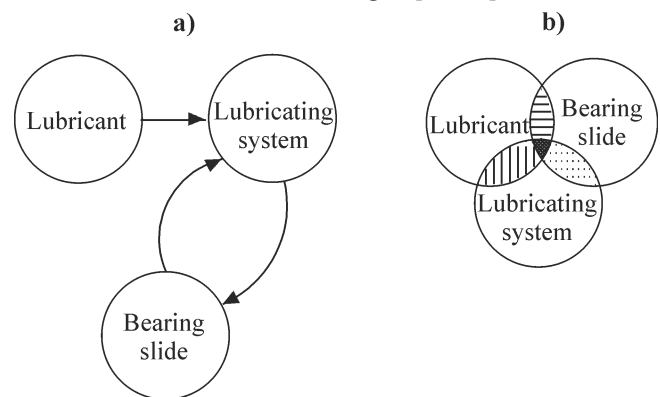


**Fig. 1.** Scheme illustrating the classification of slide bearings due to lubricating supervision: **a)** slide bearings with conventional lubrication, **b)** porous slide bearings (the lubricating system and the lubricant are within the journal-bush area)

The bushes in the porous slide bearings (Fig. 2) resemble a sponge, due to the presence of wormholes having the form of capillary ducts [4]. After saturating the porous bush with the lubricant using the vacuum method and connecting it with the journal, the self-lubricating porous slide bearing is ready for operation [9, 11, 12]

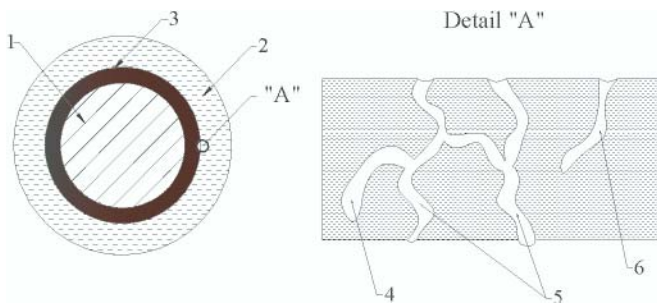


Fig. 2. Scheme of porous slide bearings : 1) journal, 2) bush, 3) lubricant placed in the bush material, 4) dead end, 5) capillary ducts open at two ends, 6) capillary duct open at one end

The self-lubricity of the porous bearings [3,10,11,12,14,15] is realised using the oil flow from the porous wall, which is mainly forced by the difference in thermal expansion of the lubricating oil and the metal bush structure (Fig. 3). Initially, when the bearing is cold, some role is also played by elastic strains of the bush material which, pressed by the journal, releases the oil from the wormholes (per analogy to a sponge). Then the journal moving at the presence of the oil generates the hydrodynamic pressure in the oil clearance. In the high pressure area the oil is pressed back into the porous wall, then it flows through the wormholes and flows out to the oil clearance at the low pressure area.

During the operation, the porous slide bearings lose their durability, following the decrease of their lubricating ability. All this is caused by oil evaporation and leakage off the bearing, due to excessively high temperatures of bearing operation and the ageing of the oil. Therefore the area of application of the porous slide bearing is limited by its load capacity, i.e. the journal load, at which the porous slide bearing can still work safely which is affected by [12]:

- the reduced amount of oil and rate of its circulation,
- the decreased hydrodynamic uplift pressure.

Experimental tests are in progress now which are oriented on evaluating permissible journal loads in porous slide bearings for given sliding speeds at which the slide bearing can still work safely [9, 11, 12, 14]. Unfortunately, in these tests different criteria of load limits for given speeds are adopted, which reduces the space for data comparison and reliability.

In this context, to provide opportunities for comparing journal load limits in different porous slide bearings, a simple physical model is proposed in the form of a four-sphere apparatus T-02. The frictional association in this machine is created using four spheres, each of 12.7 mm in diameter, made of ŁH15 steel in the accuracy class 16 according to the PN-83/M-86452 standard. Three spheres are placed in the lower holder-container having the form of a small cup, which is poured with the greasy lubricant. The fourth sphere, which

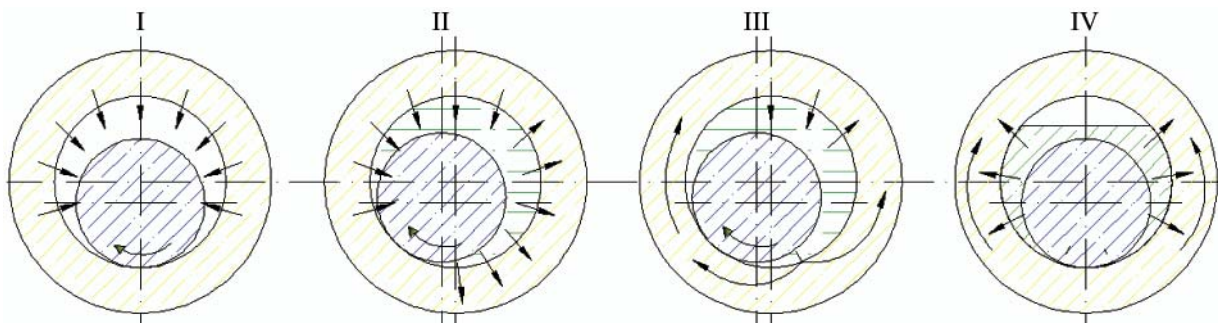


Fig. 3. Scheme of porous bearing lubrication: I) start-up, II) thermal outflow, III) equilibrium, IV) standstill [12]

models the journal in the porous slide bearing, is fixed in the upper holder. The spheres in the cup are pressed towards the sphere fixed in the upper holder using a special lever. The parameters controlled during the tests include the journal load and rotational speed, and the greasy lubricant temperature [19] – Fig. 4.

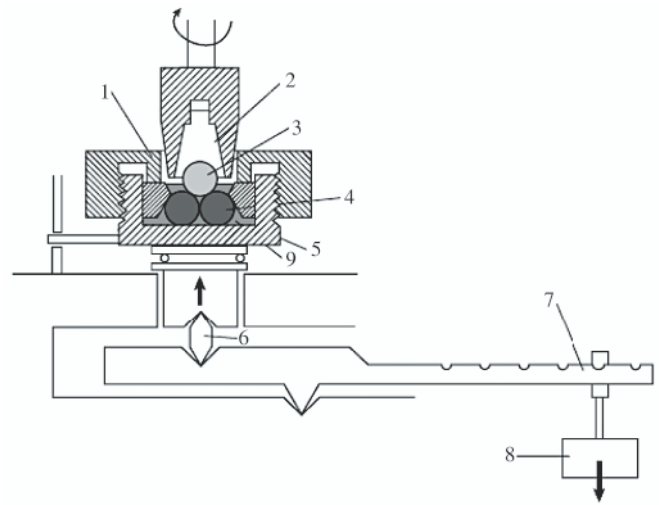


Fig. 4. Kinetic scheme of the four-sphere apparatus: 1) cover which fixes the lower spheres, 2) holder of upper sphere, 3) upper sphere (rotating), 4) lower spheres (stationary), 5) container with the tested lubricant, 6) prism, 7) lever, 8) weights, 9) tested greasy lubricant [19]

## DURABILITY OF GREASY LUBRICANTS

The greasy lubricants [16] are semi-liquid plastic lubricants having the colloidal structure which consist of the base oil (the mineral oil in general, but in exceptional cases also the synthetic oil) and the thickening agent. They are used wherever frequent lubricating oil refilling is extremely difficult or impossible. They execute all functions of liquid lubricants – except cooling and cleaning of friction surfaces. Like for the porous bearing bushes, which are the systems consisting of a metal skeleton filled with the lubricating substance, the structure of the greasy lubricants (composed of the base oil and the thickener, Fig. 5) resembles the sponge, and this fact was assumed as the required similarity criterion for creating the physical model.

In the greasy lubricant the percent share of the thickener is low, unlike the porous bushes in which the bush skeleton plays the role of “the thickener”. Frequently, to strengthen the structure of the lubricant and make it more resistant to the action of external agents, extra additives are used [16] which modify the cohesion forces between the base oil and the thickener in the required range. The bigger the cohesion forces, the more coherent is the body and the more difficult is to stratify it. Therefore the strength of the bonds can be considered the property determining durability of the greasy lubricants.

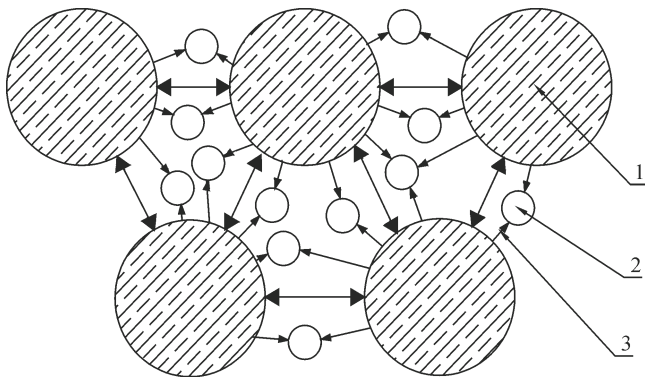


Fig. 5. Scheme of the structure of greasy lubricants:  
1) thickener; 2) base oil, 3) cohesion forces

The parameter which determines the durability of a conventional slide bearing (Fig. 1a) is the lubricating ability of the oil, i.e. the property of the lubricating substance which characterises its ability to preserve lubricating features in mitigated solid friction conditions. This way it determines oil ability to create a stable boundary layer being the consequence of the adsorption of fluid particles on the solid body surfaces. The measure of the lubricating ability of the oils is the durability of the boundary layer, i.e. the durability of bonds between the lubricating substance (adsorbent) and the base [1, 2, 6, 8, 16].

In this context it seems logical to relate the durability of the bonds with the lubricating ability of the greasy lubricants, which defines the minimal pressure required for stopping the action of the cohesion forces between the thickener and the base oil. Therefore the lubricating ability of the greasy lubricants can be considered a parameter determining the durability of the slide bearing with "limited supervision" (Fig. 1b).

## PHYSICAL MODEL OF A POROUS SLIDE BEARING

The structure of the porous bearing bush is characterised by the set of technical and operating characteristics assumed when designing and manufacturing the bearing. These characteristics determine the level of bearing applicability to realise assumed tasks in given operating conditions. Each structure has a separate set of structure parameters which map the technical condition.

$$U = \{u_i\} \text{ for } i = 1, \dots, n \quad (1)$$

Change in the technical condition of the porous slide bearing is, among other factors, a function of the resistance of the porous bush saturated with the lubricant to ageing. During bearing operation, the effects of excitation forces acting in the micro- and macro- environment of the bush cumulate with time, which leads to the leakage flow of the lubricant, and bearing seizure as a possible further consequence. Therefore an important parameter which determines the durability of the porous slide bearing is structural strength of the bushes saturated with the lubricant.

The durability of the greasy lubricant is, in turn, the feature which determines the strength  $H$  of the bonds between the thickener and the base oil (Fig. 5). Consequently, the strength of bonds of the greasy lubricant can be identified with the structural strength of the porous slide bearing bush.

The strength of bonds of the greasy lubricant can be evaluated by analysing the diagram of the friction torque (Fig. 6) as the time function, created using the results of the investigations of the physical model which was the friction pair of the apparatus T-02 (Fig. 4) immersed in the greasy lubricant.

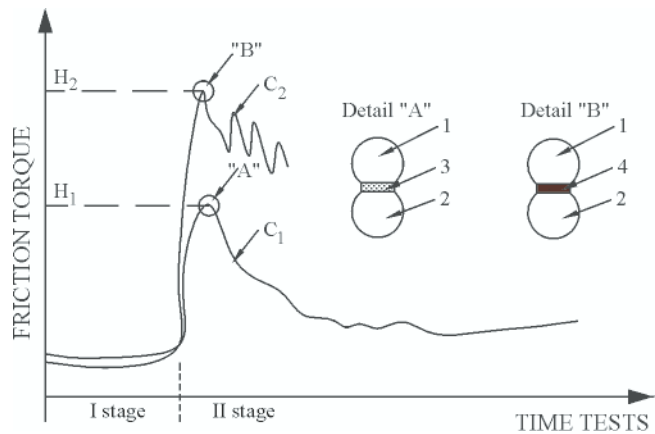


Fig. 6. Diagram of greasy lubricant friction torque:  $C_1$ ) curve which characterises the greasy lubricant revealing small strength of bonds  $H_1$ ,  $C_2$ ) curve which characterises the greasy lubricant revealing large strength of bonds  $H_2$ , A) time when the boundary layer is broken and reconstructed, B) time when the boundary layer is broken and not reconstructed, 1) upper sphere of the friction pair, 2) lower sphere of the friction pair, 3) greasy lubricant base oil, 4) friction pair seizures

The shapes of curves  $C_1$  and  $C_2$  depend on the type of the greasy lubricant. It results from their nature that the limit of strength of bonds between the thickener and the base oil is preserved as long as the lubricant resistance to breaking is larger or equal to the destroying actions (stage I). Once the bonds are broken, the leakage of the base oil takes place. If the base oil reveals high lubricating ability, characteristic for lubricants [1, 2] and, simultaneously, it has low strength of bonds of the greasy lubricant  $H_1$  (symbol A in Fig. 6), all this produces stable bonds between the base oil and the foundation. In the opposite case, when the base oil reveals low lubricating ability concerning the lubricating oil and, at the same time, high strength of bonds of the greasy lubricant  $H_2$  (symbol B in Fig. 6) the boundary layer will not appear and the seizure of the bearing will take place.

That is why the porous slide bearings for which the physical model is the friction pair in which the seizure is observed (curve  $C_2$ ), are characterised by larger maximal load which they can carry.

## EXPERIMENTAL TESTS

The measurements were performed on the friction pair of the T-02 apparatus with spheres immersed in a greasy lubricant (Fig. 4). The following lubricants were tested:

- the graphite grease created on the base of the mineral oil with 10% of natural graphite, the minimum, thickened with the lime and used for lubricating heavily loaded friction pairs in temperatures ranging between  $-20$  and  $+50^\circ\text{C}$ ;
- the LT43 grease created on the basis of the mineral oil thickened with lithium. It contains refining additives, especially those acting towards anticorrosion, anti-oxidation and improvement of lubricating abilities. It is used for lubricating heavily loaded friction pairs in temperatures ranging between  $-20$  ÷  $+130^\circ\text{C}$ ;
- the grease being a composition of the graphite grease and the LT43 grease.

Due to the flow limits of the greasy lubricants, all tests were performed at the temperature of  $100^\circ\text{C}$ . Two test procedures were executed:

- determining the strength of bonds  $H$  [Nm] at continuous load increase for the rotational speed of the spindle equal to 500 rev/min,

- determining the strength of the structure  $H$  [Nm] at continuous load increase for the rotational speed of the spindle equal to 1440 rev/min.

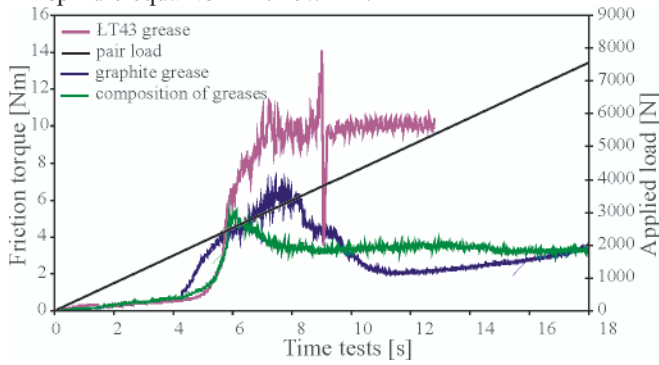


Fig. 7. Joint diagram of greasy lubricants for spindle rotational speed  $n = 500$  rev/min

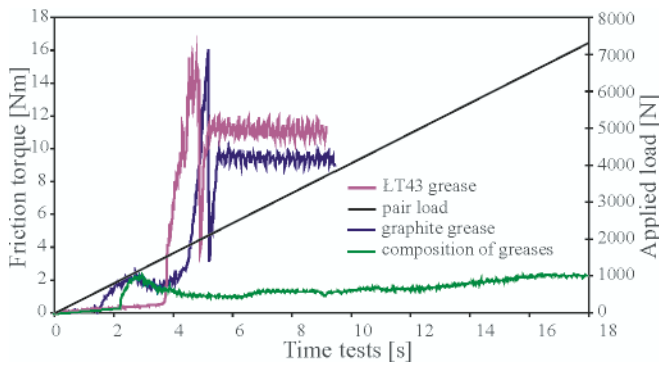


Fig. 8. Joint diagram of greasy lubricants for spindle rotational speed  $n = 1440$  rev/min.

The obtained values show that:

- the smaller the rotational speed of the journal, the larger the load  $P$  [N] needed for breaking the boundary layer created on the spheres,
- the graphite grease with the thickener having calcium compounds reveals very small strength of bonds, and the boundary layer between the spheres and the greasy lubricant in the friction pair was broken at low seizing load;
- the LT43 grease with the thickener having lithium compounds reveals high strength of bonds and breaking the boundary layer took place at higher value of seizing load.
- the composition of greases consisting in 50% of the graphite grease and 50% of the LT43 grease reveals the strength of bonds comparable with the graphite grease.

When the boundary layer is broken, the thickener and the base oil separate from each other (points A and B in Fig.6) which provides opportunities for evaluating the strength  $H$  of

bonds of the greasy lubricants. This value of  $H$  can be identified with the structural strength of the bushes saturated with the lubricating oil, considered the basic parameter of the durability of porous slide bearings.

## POSSIBILITY OF TRANSFER OF THE MEASURED RESULTS TO A REAL OBJECT

The rate of the conversion of the porous slide bearing from the state of operating ability to partial ability, or disability, can be presented using the Weibull, normal, or another distribution. Therefore transferring the experimental data from the physical model to a real object is possible, for instance by creating the interval of porous slide bearing technical efficiency tolerance [8] depending on the bush structure parameter which determines the durability of porous slide bearings. This can be done in the following steps:

- measuring the strength of bonds of the greasy lubricant having the characteristics correlated (via acoustic emission, for instance [7]) with the strength of the porous bearing bush structure with respect to the operating time  $\tau_1$  (the values will be within the interval  $u' - u''$  and their distribution will be close to normal – Fig. 9);

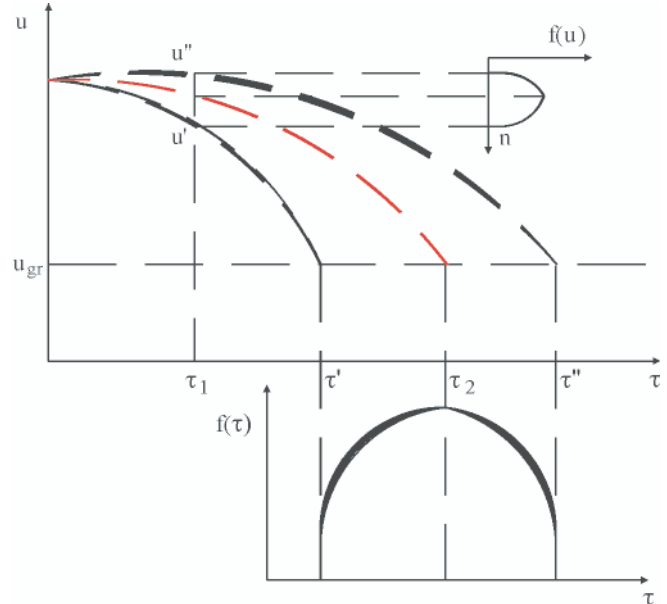


Fig. 9. Interval of porous slide bearing technical efficiency tolerance:  $\tau$  – time of porous slide bearing operation,  $u$  – strength of porous slide bearing bush structure,  $u_{gr}$  – bush structure strength limit,  $f(u)$  – probability density of the random variable  $u$ ,  $f(\tau)$  – probability density of the random variable  $\tau$

- determining the time period of full operating ability of the porous slide bearings until time  $\tau_2$  with the tolerance ranging

Table 1. Evaluated values of diagnostic parameters

	Results of measurements for $n = 500$ rev/min		
	Seizing load $P$ [N]	Seizing load limit $P_z$ [N]	Strength of bonds $H$ [Nm]
Graphite grease	1656	7400	6.7
Grease LT43	2229.6	3943.2	11.21
Composition of greases	1924.8	7400	5.37
Results of measurements for $n = 1440$ rev/min			
	Seizing load $P$ [N]	Seizing load limit $P_z$ [N]	Strength of bonds $H$ [Nm]
Graphite grease	700.8	2389.2	2.34
Grease LT43	1461.6	1984.8	15.61
Composition of greases	820.8	7400	2.29

within  $\tau' - \tau''$  for the known limit of the strength of bonds of the greasy lubricant (the value taken from experimental investigations) - Fig. 9.

## FINAL REMARKS AND CONCLUSIONS

- Although the physical model of a porous slide bearing, presented in the article as the friction pair of the apparatus T-02, cannot be treated as fully adequate to real porous slide bearings, the obtained results of the tests indicate that the application of the here presented method for examining the strength of the porous bush structure is fully justified.
- The presented theoretical and experimental analysis of the physical model shows that the strength of bonds of the greasy lubricants, i.e. their lubricating ability can be considered one of parameters of porous bearing bush structure. The analysis of lubricating ability of the greasy lubricants determines the area of applications of the porous slide bearings with respect to their lubricating ability, i.e. durability.

## BIBLIOGRAPHY

1. Bzura P.: *Method of identification of the sidle tribological system top laser condition by ASSESSMENT of the T-02 four-ball tester friction NODE operation*, Journal of KONES Powertrain and Transport, Vol.16, No.3, p.69-76, Warszawa 2009.
2. Bzura P.: *The effect of lubricating ability on the operation of the tribological system*, (in Polish), Zeszyty Naukowe Akademii Marynarki Wojennej, 178A / editor: Cz. Dyrzc - Instytut Konstrukcji i Eksploatacji Okrętów AMW. - Gdynia: Wydaw. AWM. – 2009.
3. Cameron A.: *The principles of lubrication*. New York McHill 1987.
4. Cegielski W., Rutkowski W.: *Sintered bearings* (in Polish). Warsaw, PWT, 1960.
5. Girtler J.: *Statistic and probabilistic measures of diagnosis likelihood on the state of self-ignition combustion engines*, Journal of POLISH CIMAC Diagnosis, Reliability and Safety, Vol.2, No. 2, Gdańsk 2007, p.57-63.
6. Girtler J.: *Stochastic Model Of The Process Of Starting Combustion Engines And Practical Application Of The Process*, Journal of POLISH CIMAC Diagnosis, Reliability and Safety, Vol.3, No. 2, Gdańsk 2008, p.47-54.
7. Girtler J., Darski W., Olszewski A., Baran I., Nowak M.: *The use of acoustic emission to identification damages bearings the main and crank engines about the automatic ignition*, Journal of POLISH CIMAC Diagnosis, Reliability and Safety, Vol.4, No. 2, Gdańsk 2009, p.57-70.
8. Hebda M., Mazur T., Pelc H.: *Theory of operation of vehicles*, (in Polish), Wydawnictwo komunikacji i łączności Warsaw 1978.
9. GLACIER INDUSTRIAL BEARINGS Catalogues, UK.
10. Krzeziński K.: *Pressure distributions and load capacity of the hydrodynamic lubricating film in porous bearings*, (in Polish), Theoretical and Applied Mechanics 2/1978, s. 169–180.
11. Lawrowski Z.: *Technique of lubrication*, (in Polish), Wydawnictwo Naukowe PWN Warsaw 1996.
12. Lawrowski Z.: *Maintenance-free slide bearings*, (in Polish), Wydawnictwo Politechniki Wrocławskiej, Wrocław 2001.
13. Meurisse M.H., Guidicelli B.: *3D conservative model for self-lubrication porous journal bearings in hydrodynamic study-state*. Journal of Tribology. Tran. of the ASME, Vol. 121/3, 1999, s. 529–537.
14. Nepale M.J.: *Tribology handbook*, Butterworths, Londyn 1973.
15. Nield D.A., Bejan A.: *Convection in Porous Media*. Springer-Verlag, New York, Berlin, Heidelberg 1999.
16. Industrial lubricants. Manual, (in Polish), Wydawnictwo TOTAL Polska Sp.z o.o., Warsaw 2003.
17. Project Guides, MAN Diesel&TURBO.
18. Ship Power Product Catalogue, Wärtsilä.
19. Szczerek M., Tuszyński W.: *Tribological tests. Seizing*. Radom: Biblioteka Problemów Eksploatacyjnych 2000.

---

## CONTACT WITH THE AUTHOR

Piotr Bzura, Ph. D.  
Faculty of Ocean Engineering  
and Ship Technology  
Gdansk University of Technology  
Narutowicza 11/12  
80-233 Gdansk, POLAND  
e-mail: pbzura@pg.gda.pl

# Influence of local bush wear on properties of water lubricated marine stern tube bearings

Wojciech Litwin, Ph. D.  
Gdansk University of Technology

## ABSTRACT



*In recent years more and more frequently can be met ships in which propeller shaft water-lubricated polymer bearings have been applied. It results from their simplicity and associated relatively low initial and operational cost as compared with the complex classical sealed system based on oil-lubricated bearings. It is worth mentioning that the water-lubricated bearings are also environmentally friendly as no risk of pollution with lubricating oil used in classical systems, is involved. Design procedure of bearings in question based on materials available from their producers is relatively simple. However the calculating of such bearings creates many problems. For calculating the hydrodynamic lubricating theory is as a rule used and elastic bush flexibility taken into account. In the case of greater loads when lubricating film is very thin to achieve a proper solution is very difficult.*

*For this reason is proposed a novel method in which bush local wear effect can be accounted for. Such phenomenon has been observed during experimental tests of heavy-loaded water-lubricated slide bearings. With the use of the applied calculation algorithm bush local wear close to its edges can be taken into account, and - in consequence - a greater bearing capacity can be achieved.*

**Keywords:** bearing systems; water-lubricated bearing; propeller shaft bearing systems

## INTRODUCTION

In recent years water-lubricated bearings fitted with polymer bushes have been more and more commonly applied to shipbuilding, hydro power industry and water pumps. Such solution has many merits among which lack of risk of contamination of the environment by lubricants is crucial one.

Recently more and more sliding polymers capable of operating in water have been appeared on the market. Their price has been dropping that makes such solution more and more attractive. Moreover, many data on successive applications of water - lubricated bearings have appeared. Their producers have used the issues for advertising their products whose life time is estimated to about thirty years. However as results from practice such bearings behave in very different ways during operation and in the past many dangerous breakdowns resulting in ship docking or premature repairing of water turbine, happened.

The bearing lubricated with water, a low viscosity liquid, shows many limitations. Doubtlessly, it develops always a smaller hydrodynamic capacity as compared with oil-lubricated bearing of the same size. In addition, it shows form instability of polymer bush which, due to shrinkage mounting and water soaking, is capable of suffering large deformations. There are known many cases of propulsion shaft or rudderstock blocking due to polymer bush swelling. In order to prevent shaft seizing bush producers often recommend to increase bearing clearance, that results in lowering their hydrodynamic features. A less dangerous consequence of bush expansion during shrinkage mounting and subsequent water absorption in initial phase of its operation is rather large form deformation

of its sliding surface. The effect is especially distinct if lead-over longitudinal grooves necessary for heat transferring by water from friction zone, are made in the bush. In such case significant deformations occur in the vicinity of the grooves as bush material is there of the smallest thickness [1].

In calculating a water-lubricated bearing an isothermal model can be used, that highly facilitates to obtain calculation results [2]. In order to achieve reliable results for bearing hydrodynamic capacity elastic polymer bush flexibility should be accounted for. However it makes a trouble. It turns out that to precisely determine shape elasticity value is rather difficult. Usually only its approximate value is given. Hence especially in the case of more flexible materials calculation results may contain a great error, that was confirmed experimentally [3].

## RESEARCH PROBLEM

The research problem in question results from the need of answering the question as to which extent water-lubricated polymer hydrodynamic bearing can be loaded.

In the Faculty of Ocean Engineering and Ship Technology, Gdansk University of Technology, have been conducted for several years experimental and theoretical projects aimed at solving a set of problems associated with water-lubricated bearings. One of the crucial research problems was to determine ultimate hydrodynamic load-carrying capacity of bearings of the kind [4, 5]. Results of the performed experimental tests have been very promising. Polymer bearings of many kinds were tested. The shaft of the test stand was of 100 mm diameter, and the tested bushes were from 100 to 400 mm in length. The

shaft rotational speed was varied in the range of  $0 \div 11$  rev/s, that made it possible to obtain linear slide velocities below 3.5 m/s. From the performed tests it results that the bearings have operated in the fluid friction range even under the pressure of the order of 0.5 MPa (Fig. 1 and 2).

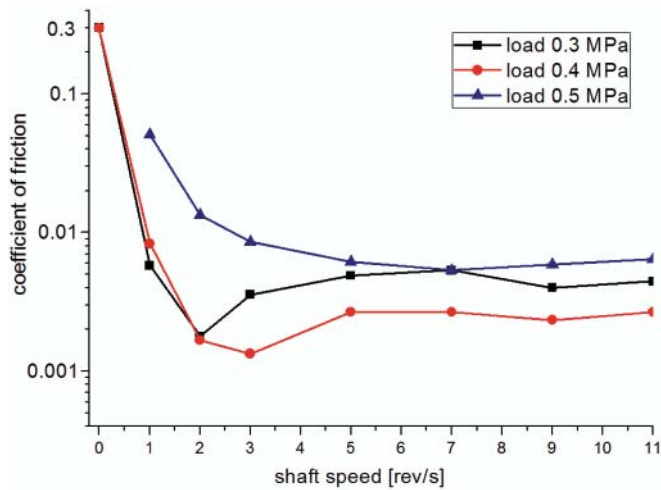


Fig. 1. Diagram of the measured friction torque converted to value of coefficient of friction, under the load up to 0.5 MPa and at shaft rotational speed in the range of  $1 \div 11$  rev/s

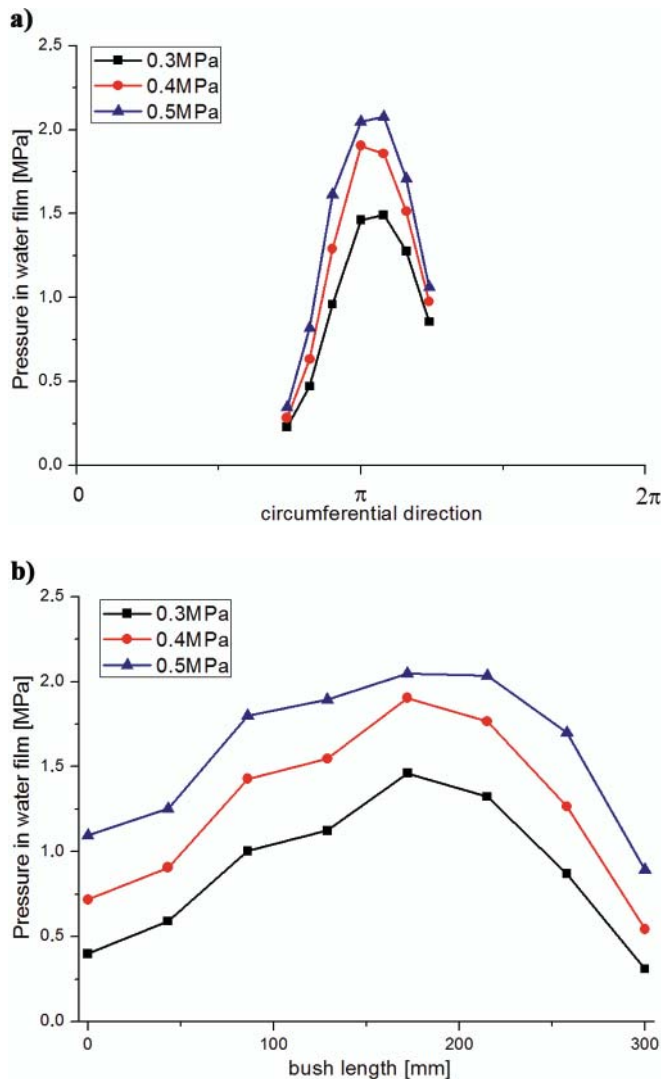


Fig. 2. The pressure distribution in bearing lubricating film, measured on the test stand at the shaft rotational speed of 11 rev/s and under the load range from 0.3 to 0.5 MPa: a) in circumferential direction within the range of  $0 \div 2\pi$ , b) in longitudinal direction within the range of  $0 \div 300$  mm

A serious problem is met in conducting calculations for the similar bearing by applying the hydrodynamic lubrication theory, (EHL), to bush elastic material. Namely, below certain minimum film thickness which, in the case in question, amounts to about 5 to 7  $\mu\text{m}$  for elastic materials, it was not possible to obtain a convergent solution. The iteration between a module which calculates pressure distribution in lubricating gap and a module which calculates elastic deformation field of bush surface has not led to any convergent solution (Fig. 3)

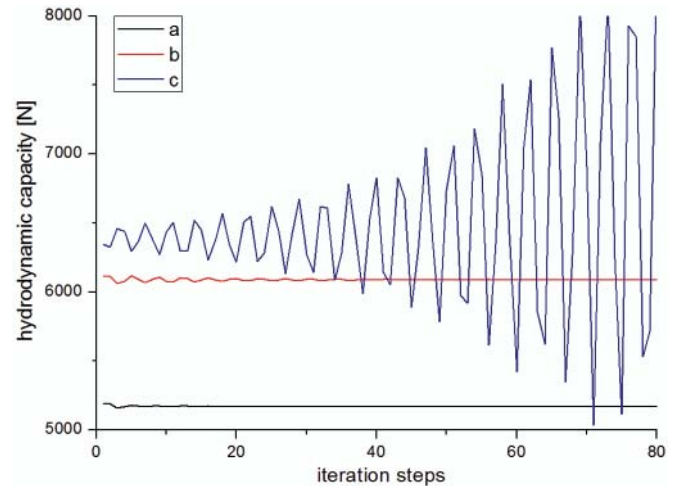


Fig. 3. An attempt to calculating hydrodynamic capacity of a heavy-loaded bearing fitted with elastic bush, a, b) for film thickness values of over  $5 \mu\text{m}$  and c) for a smaller value - in this case the iteration diverges and no solution is available.

Attempts to solving the problem which consists in introduction of the so-called relaxation factor, did not give any satisfying result. In practice in the case in question it was not managed to achieve a stable solution for lubricating films thinner than  $5 \div 7 \mu\text{m}$ . The calculations performed for the minimum acceptable lubricating gap of  $5 \mu\text{m}$  showed a much lower value of bearing capacity as compared with results of experimental tests (Fig. 4).

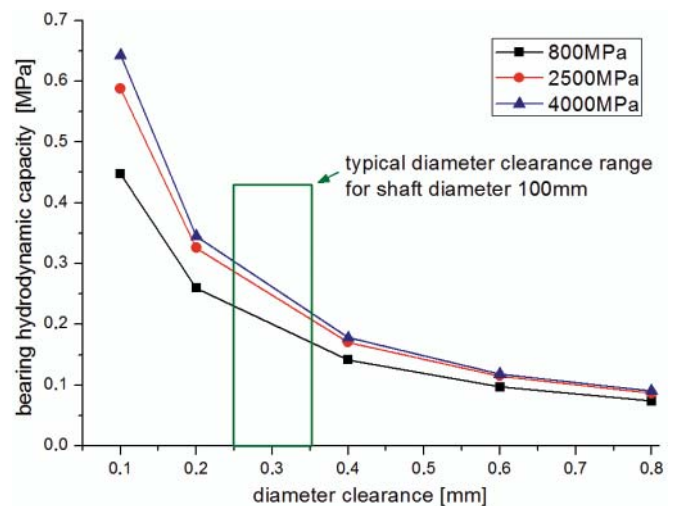


Fig. 4. The calculated maximum potential hydrodynamic capacity of water-lubricated bearing in function of bush material, bearing diameter clearance; shaft speed 11 rev/s

However it is possible to reach certain conclusions by analyzing results of the calculated pressure distributions and bush elastic deformations (Fig. 5 and 6). As turns out, elastic deformation value may exceed that assumed for calculations of minimum film thickness amounting to  $5 \mu\text{m}$ . In practice an elastic sag of bush results in dropping value of hydrodynamic pressure

in lubricating film, that detrimentally affects bearing capacity. As appears, the zones close to bush edges are not elastically deformed due to hydrodynamic pressure action. Analyzing the experimentally tested bushes one observed significant wear in the zones, which is visible because sliding surface fast became polished in the places.

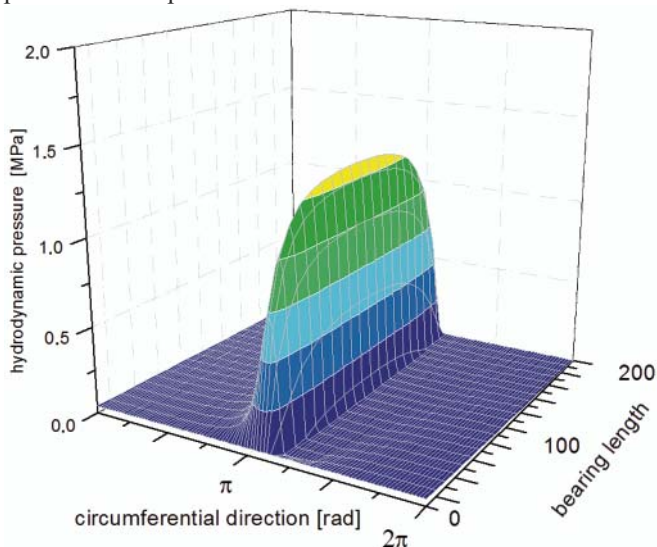


Fig. 5. The calculated pressure distribution in lubricating film of water-lubricated polymer bearing, (P1), in function of bush length (of  $l \div 200$  mm) and bush developed circumference (of  $0 \div 2\pi$  rad)

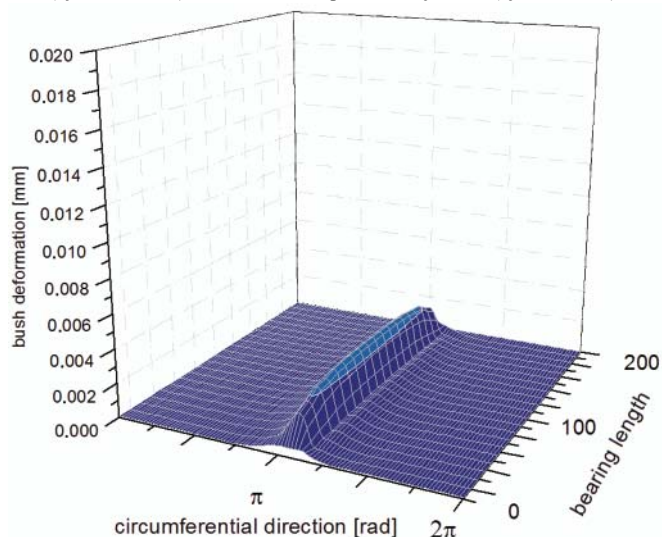


Fig. 6. The calculated distribution of elastic deformation of polymer bush of water-lubricated bearing, (P1), in function of bush length (of  $l \div 200$  mm) and bush developed circumference (of  $0 \div 2\pi$  rad)

## PRESENTATION OF THE PROPOSED CALCULATION METHOD

During searching subject-matter literature sources dealing with slide bearing systems, has been found several papers whose authors undertook the task to predict growing wear [6 ÷ 10]. Unfortunately the papers did not help in solving the wear problem of water-lubricated bearing and its effect on bearing capacity.

Basing on the earlier conducted projects one decided to perform calculations for the case when local wear occurs close to bush edges. To make it possible the classical algorithm of EHL method has been modified.

It was assumed that the minimum lubricating gap height was equal to  $5\mu\text{m}$ . If due to application of greater and greater load the lubricating gap decreases and its height becomes smaller than the assumed minimum then wear will occur. As a result

of the process bush geometry undergoes permanent change. The schematic diagram of the relevant calculation software is shown in Fig. 7.

It was assumed that the method in question has to serve for calculating slide bearing capacity with accounting for edge wear. However if the procedure of application of greater and greater load is not terminated then the model will approach to the ridging effect reported in literature sources, when the journal rubs out a longitudinal groove in the bush. In the author's opinion the effect will not occur in the case of ship shaft line bearing as the shaft operates with various rotational speeds and the bearing's loading results from many different factors, e. g. ship operation in heavy weather conditions. Therefore working position of the shaft against the bush changes in operation and bush ovalization appears after long period of service (Fig. 8).

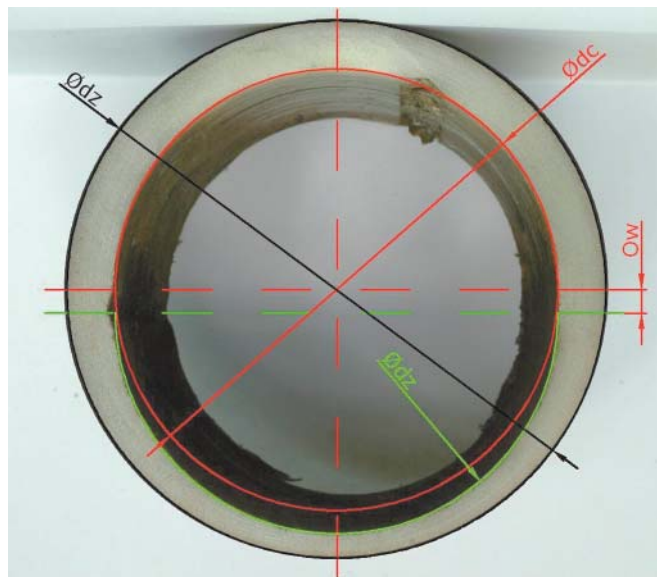


Fig. 8. Heavy-used water-lubricated slide bearing in which distinct bush ovalization took place and consequently the shaft altered its position down by the value  $O_w$ ;  $\text{ød}z$  external bush diameter;  $\text{ø}dc$  initial bush internal diameter;  $\text{ød}z$  worn area diameter

## THE TESTED BEARING AND ITS SIMULATED WORKING CONDITIONS

The calculations were performed for two kinds of bush material of different values of module of shape elasticity. The analysis was performed for the polymer of shape elasticity module equal to about 2500 MPa and the rigid composite of shape elasticity module equal to about 4500 MPa (Tab. 1). As the lubricating medium fresh water of  $5^\circ\text{C}$  temperature and viscosity of about  $1.55\text{ mPa}\cdot\text{s}$ , was assumed. The calculations were conducted for the shaft rotational speed of 11 rev/s.

## RESULTS OF THE CALCULATIONS

Results of the calculations of hydrodynamic pressure distributions in lubricating film, and bush elastic deformations resulting from interaction between pressure field and wear field, are presented in Fig. 9 ÷ 12. The developed surface diagrams were made for the lower part of the bush of the analyzed bearing (for circumference arc changeable from  $0.5\pi$  to  $1.5\pi$ ) and the bush length from 0 to 200 mm. In order to make interpretation of the diagrams easier, values of elastic deformation and wear are shown within the same range, i. e. from 0 to  $20\mu\text{m}$ . Values of ultimate relative journal-bush eccentricity as well as results of the calculated bearing capacity are shown in Tab. 1.



Tab. 1. Input data and results of the calculations for two kinds of the analyzed polymer bush of different values of shape elasticity module

No.	Bearing code	Bush material type	Module of elasticity	Bearing clearance/shaft diameter/bush thickness [mm]	Shaft eccentricity ratio ( $\epsilon$ )	Maximum wear [ $\mu\text{m}$ ]	Calculations results – maximum hydrodynamic capacity
1	P1	polymer	2500 MPa	0.3/100/12	0.965	0	5537 N
2	P2				0.98	16	6320 N
3	C1	composite	4500 MPa		0.965	0	5929 N
4	C2				0.98	13	6394 N

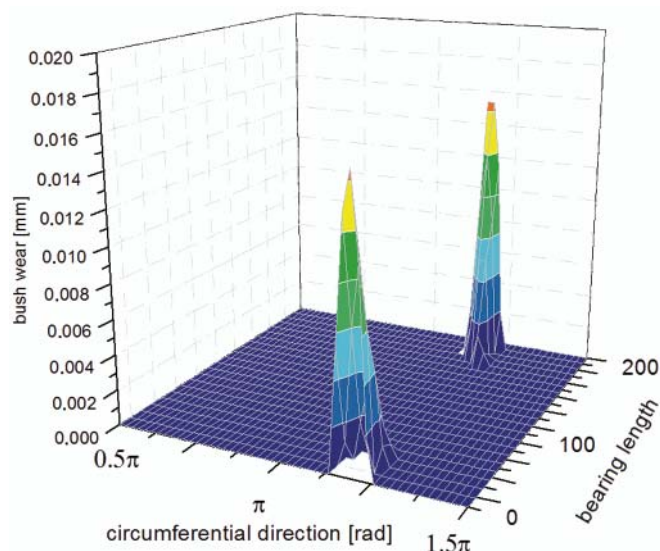


Fig. 11. The wear field for the bush of the elasticity module of 2500 MPa, (P2), at the shaft rotational speed of 11 rev/s; the wear occurred close to the bearing's edges only

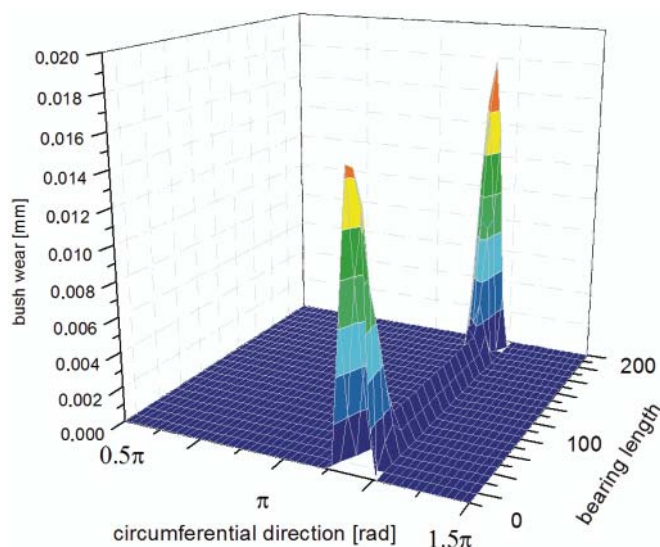


Fig. 12. The wear field for the bush of the elasticity module of 2500 MPa, (P2); the wear occurred also along the whole breadth of the bearing; this is the case when the calculations have been discontinued; the shaft rotational speed of 11 rev/s; the calculated bearing capacity of 6500 N

## CONCLUSIONS

The proposed calculation method based on the EHL model extended by a module which accounts for bush wear, made it possible to obtain calculation results for the conditions in which the classical model ceases to be effective.

In the author's opinion the proposed calculation method is reliable as the phenomenon of local seizing close to bush edges was observed in the experimentally tested bearings.

The performed calculations demonstrated that the accounting for bush local wear makes it possible to increase theoretical

bearing capacity by 7% in the case of the more rigid composite material and by nearly 15% for the less rigid one (polymer).

The calculated bearing hydrodynamic capacity with accounted for bush local wear reaches the value of 0.316 MPa. On the basis of experimental tests it is possible to conclude that the maximum hydrodynamic capacity of bearings of the kind may reach even the value of 0.5 MPa. Therefore it should be considered why not to carry out calculations for smaller values of lubricating film thickness and greater values of bush wear located not only close to its edges but also along the whole contact line between shaft and slide bush (Fig. 12).

The proposed calculation method may be applied also in the case of the skewed shaft against bush, i.e. in which the method may be especially helpful.

## BIBLIOGRAPHY

- Litwin W.: *Marine water lubricated main shaft bearings, problems, theoretical and experimental research*. Polish Maritime Research No. 4, Vol. 16, 2009
- Litwin W.: *Water – An Extraordinary, Ordinary Lubrication Liquid. Influence Of Water Salinity, Pressure And Temperature On Water Lubricated Bearings Properties*. ASME/STLE International Joint Tribology Conference October 17 ÷ 20, 2010, San Francisco, California, USA
- Litwin W.: *Influence of main design parameters of ship propeller shaft water-lubricated bearings on their properties*. Polish Maritime Research No. 4 (67), Vol. 17, 2010
- Litwin W.: *Water Lubricated Marine Stern Tube Bearings – Attempt At Estimating Hydrodynamic Capacity*. ASME/STLE International Joint Tribology Conference October 19 ÷ 21, 2009, Memphis, Tennessee, USA
- Litwin W.: *Marine water lubricated stern tube bearings – calculations and measurements of heavy loaded bearings*. STLE/ASME International Joint Tribology Conference October 20 ÷ 22, 2008, Miami, Florida, USA
- Ramalho A.: *A geometrical model to predict the wear evolution of coated surfaces*. *Wear*, 264 (2008)
- Sfantos G. K., Aliabadi M. H.: *Wear simulation using an incremental sliding Boundary Element Method*, *Wear*, 260 (2006)
- Nikolakopoulos P. G., Papadopoulos C. A.: *A study of friction in worn misaligned journal bearings under severe hydrodynamic lubrication*. *Tribology International*, 41 (2008)
- Bouyer J., M. Fillon, and I. Pierre-Danos: *Influence of Wear on the Behavior of a Two-Lobe Hydrodynamic Journal Bearing Subjected to Numerous Startups and Stops*. *ASME Journal of Tribology*, January 2007, Vol. 129
- Wang, W., Wong, P.L., Guo, F.: *Application of partial elasto-hydrodynamic lubrication analysis in dynamic wear study for running-in*. *Wear*, 2004, Vol. 257.

## CONTACT WITH THE AUTHOR

Wojciech Litwin, Ph. D.  
Faculty of Ocean Engineering  
and Ship Technology  
Gdansk University of Technology  
Narutowicza 11/12  
80-233 Gdansk, POLAND  
e-mail: wlitwin@pg.gda.pl

# Model of thermal comfort in the hyperbaric facility

Anna Majchrzycka, Ph. D.  
West Pomeranian University of Technology, Szczecin

## ABSTRACT

*The paper discusses the mathematical model of thermal comfort in the hyperbaric facility. Based on human thermal balance and thermal comfort conditions the comfort equation for the hyperbaric environment was derived. The comfort equation enables to calculate all those combinations of the diver's activity, clothing (thermal insulation, moisture permeation factor) and environmental variables (temperature, pressure, composition, relative humidity and velocity of the breathing gas and mean radiant temperature), which would create thermal comfort in the hyperbaric environment. The paper presents also the solution of thermal comfort equation for dives up to the depth of  $g = 590$  m, with helium-oxygen and hydrogen-oxygen breathing mixture, as well as the comfort diagrams.*

**Keywords:** comfort temperature; human balance; hyperbaric environment

## INTRODUCTION

Saturation diving is the diving operation that enables man to live and work in the sea-going deep dive systems or to be trained in the land-based hyperbaric complexes for a long time. Advanced diving technique requires an optimal breathing gas to be selected. The use of air as the breathing gas is limited because of oxygen toxicity and narcotic effect of nitrogen [5, 14, 15]. Breathing mixtures used in deep diving consist of oxygen that meets demands for metabolic needs and inert gases (helium, nitrogen, hydrogen). Moreover, breathing gas contains contaminants generated by the divers during exposure and some gaseous additives improving voice communication (sulphur hexafluoride, carbon tetrafluoride) or freon used as fire extinguishing agent [5].

Saturation diving is based on the principle that the tissues and blood of a diver's body absorb inert gases and reach saturation point where the pressure of the dissolved gas in the blood and tissues is the same as that of the gas in the lungs. The diving technique is based on the fact that once the saturation point has been reached the diver can safely remain saturated for a long period, and the diver's obligation for decompression does not increase with further exposure. It makes deep diving operations more efficient.

Most of the deep diving experience is based on the breathing gas containing helium, however the last years have shown that hydrogen also can be used [4] as the component of breathing mixtures used in saturation diving. There were also some trials

with experimental breathing mixtures containing the other inert gases: neon, argon [5].

Helium and hydrogen causes certain thermal problems related to dangerous cooling of the divers. This is due to the high thermal conductivity and specific heat of helium and hydrogen. Therefore, comfort temperature in the hyperbaric environment increases with the total pressure of gas and should be maintained at a level higher than that in atmospheric air [8, 9, 11, 14, 15, 16, 17, 18, 19, 20].

A sea-going deep dive system presented in Fig.1 consists of the support vessel, deck decompression chamber and diving bell. A land-based hyperbaric facility presented in Fig. 2 includes one or a series of the hyperbaric chambers where the divers live and work at the pressure which simulates the ambient one at their work site. Dry or wet chambers of the land-based hyperbaric facility are connected by locks. The chambers can be maintained at the same pressure or different one depending on the goals of hyperbaric tests (medical tests, equipment tests, etc).

One of the major tasks of the life support systems of the hyperbaric facilities is to create the environment which maintains the safe level of oxygen partial pressure, required level of contaminants and the thermal comfort for the divers [15]. The thermal comfort is defined by ASHRAE standard 55-66 [2], as a state of mind that express satisfaction with the surrounding environment.

There are many variables which influence the thermal comfort condition in hyperbaric environment: pressure,

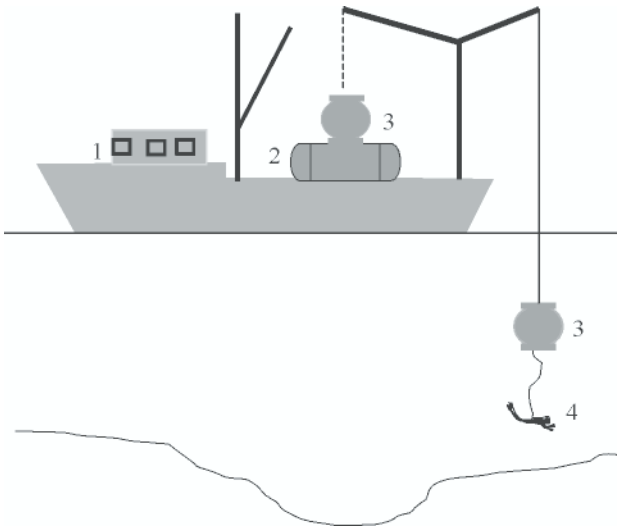


Fig. 1. Sea-going deep dive hyperbaric system: 1) support vessel, 2) deck decompression chamber, 3) diving bell, 4) diver

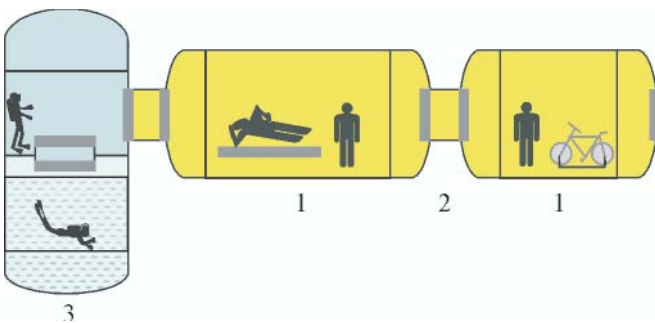


Fig. 2. Land-based hyperbaric complex: 1) dry hyperbaric chamber, 2) lock, 3) „wet-pot” hyperbaric chamber

composition, temperature, humidity and relative velocity of the breathing mixture, mean radiant temperature, activity level and thermal insulation of the diver's clothing. It is impossible

to consider the effect of any of the above mentioned variables independently. Thermal comfort can be reached by many different combinations of the environmental variables, however there are also some irrational (human) factors (stress, fatigue, etc.) which should be taken into consideration. Fig. 3 presents the factors (grouped in six blocks - pieces of thermal comfort puzzle supplemented with block of irrational factors.) which affect thermal comfort in the hyperbaric facility.

Not many earlier comfort studies for the hyperbaric environment have taken all the above mentioned variables into account. However, few studies have been performed on men to ascertain the comfort conditions experimentally and theoretically [3, 8, 9, 11, 13, 16, 18, 19, 20].

In order to determine the comfort temperature in the hyperbaric environment the comfort equation based on the mathematical model of human body thermal exchange, was developed. Mathematical modelling of thermal comfort enables to assure the comfort temperature by taking into account the most important variables which affect thermal comfort in the hyperbaric facility:

$$t = f(p, x_i, c_p, \lambda, \eta, \rho, \dot{q}_m, I_{cla}, t_r, \phi, v) \quad (1)$$

### THERMAL COMFORT EQUATION FOR THE HYPERBARIC FACILITY

The overall steady-state thermal balance of the human body can be expressed [2] with the following equation:

$$\dot{Q}_m - \dot{Q}_e - \dot{Q}_o = \dot{Q}_p = \dot{Q}_c + \dot{Q}_r \quad (2)$$

The equation (2) expresses that the flux of metabolic heat production,  $\dot{Q}_m$ , minus the flux of heat loss by evaporation from the skin,  $\dot{Q}_e$ , and that by respiration,  $\dot{Q}_o$ , is equal to the flux of heat conducted through the clothing,  $\dot{Q}_p$ , and that dissipated from the outer surface of the clothing by convection,  $\dot{Q}_c$ , and radiation,  $\dot{Q}_r$ . Figure 3 shows the overall thermal balance of the human body. As seen from Fig. 3 the flux

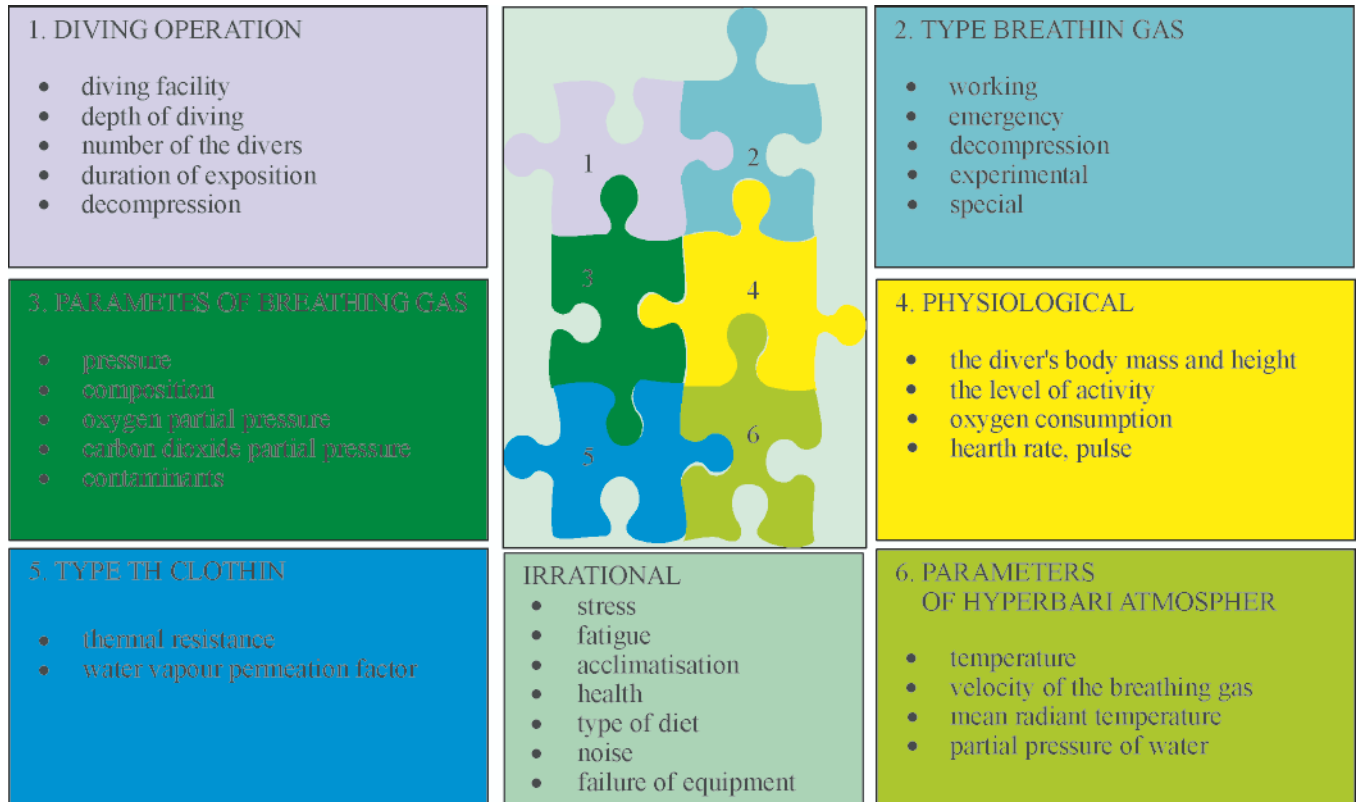


Fig. 3. Factors which influence thermal comfort in the hyperbaric facility.

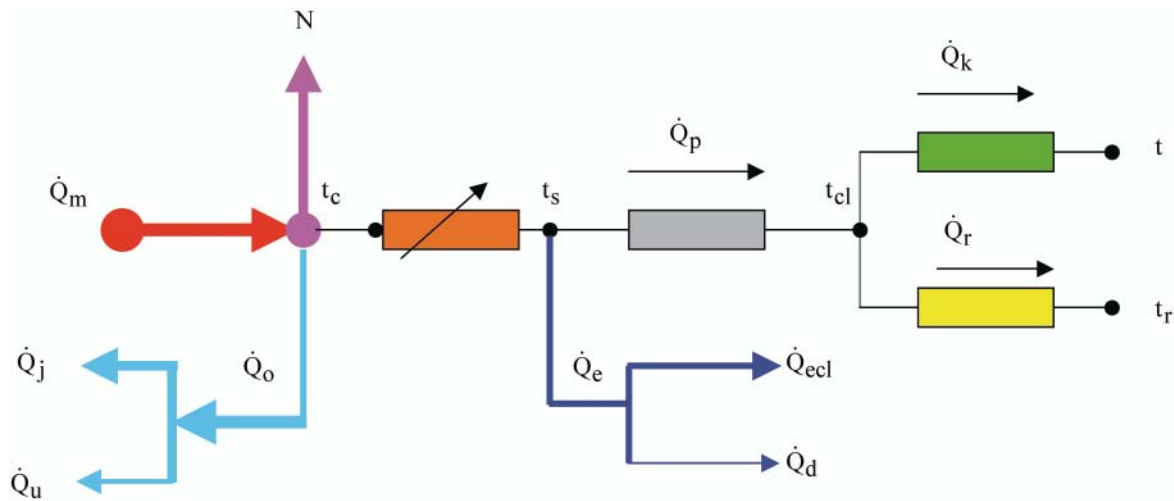


Fig. 4. Overall thermal balance of the human body

of heat loss by respiration,  $\dot{Q}_o$ , and by evaporation from the skin,  $\dot{Q}_e$ , are not driven by the temperature difference directly.

The flux of metabolic heat released in oxidation processes in human body is partly converted into the external power  $N$  and the internal body heat flux  $\dot{Q}$ , hence thermo-regulatory system maintains the core temperature  $t_c$  approximately constant:

$$\dot{Q}_m = \dot{q}_m \cdot A_{Du} = \dot{Q} + N \quad (3)$$

External mechanical efficiency is defined as [2]:

$$\eta_d = \frac{N}{\dot{Q}_m} \quad (4)$$

By introducing the equation (4) to equation (3) the following is obtained:

$$\dot{Q} = \dot{Q}_m (1 - \eta_d) \quad (5)$$

The flux of heat loss by respiration consists of the flux of dry respiration heat loss,  $\dot{Q}_{oj}$  and the latent respiration heat loss  $\dot{Q}_{ou}$ :

$$\dot{Q}_o = \dot{Q}_{oj} + \dot{Q}_{ou} \quad (6)$$

The flux of heat loss by evaporation consists of flux of heat loss by water vapour diffusion through skin and sweat evaporation from the skin:

$$\dot{Q}_e = \dot{Q}_d + \dot{Q}_{ecl} \quad (7)$$

The heat loss by sweat evaporation is affected by skin temperature and the activity level. The skin assists in thermal homeostasis. The blood vessels and sweat glands located in the skin are activated due to thermal environmental conditions. Vasodilatation which allows increased blood to flow through the artery, sweat secretion and evaporation are the most important ways by which man attempts to lose excess of body heat. In cold conditions sweat is not secreted, muscles under the surface of the skin contract lifting the hair follicle upright and cause "goose bumps". Vasoconstriction enables to direct blood away from the skin and towards the warmer core of the body. This prevents blood against losing heat to the surroundings and also prevents the core temperature against decreasing.

The transfer of heat from skin to the outer surface of clothed body is rather complex as it consists of internal convection and radiation in material pores and conduction through material of the clothing itself, [2]. Flux of heat transferred from the skin to the outer surface of clothed body depends upon the total heat resistance to transfer from skin to the outer surface, skin temperature and temperature of the outer surface of the clothing:

$$\dot{Q}_p = \frac{(t_s - t_{cl}) \cdot A_{Du}}{R_{cl}} \quad (8)$$

The total heat resistance to transfer from skin to the outer surface of the clothed body is given as follows [2]:

$$I_{cla} = \frac{0.155}{R_{cl}} \quad (9)$$

The flux of heat dissipated by convection from the outer surface of the clothing,  $\dot{Q}_k$  and radiation,  $\dot{Q}_r$ , depend upon ambient temperature and mean radiant temperature, emissivity of skin and clothing surface and thermal properties of the environment. Satisfaction of the heat balance equation (2) is the first sufficient condition for the diver's thermal comfort under long exposure to the hyperbaric environment. At a given activity level the skin temperature and the heat loss by evaporation are deemed the only physiological variables which influence the heat balance equation (2). Sensation of thermal comfort has been related to magnitude of the two variables:

$$t_s = f_1(\dot{q}_m), \quad a < t_s < b \quad (10)$$

$$\dot{q}_e = f_2(\dot{q}_m), \quad c < \dot{q}_e < d \quad (11)$$

Man is in thermal comfort when the mean skin temperature and sweat secretion is maintained within the narrow limits (a, b) and (c, d), respectively, determined by the physiologists. According to the mathematical comfort model, [2], the equations (10) and (11) represent the second and third basic conditions for thermal comfort. The skin temperature for persons in thermal comfort, experimentally investigated in atmospheric air, can be expressed [2] as follows:

$$t_s = 35.7 - 0.026 \cdot \dot{q}_m \cdot (1 - \eta_d) \quad (12)$$

Under the assumption that the skin temperature in hyperbaric environment is nearly the same [3] as in atmospheric air it is more convenient to express the second comfort condition (10) in function of the oxygen consumption, external mechanical efficiency and type of diet:

$$t_s = 35.7 - 0.032 \cdot C \cdot \dot{V}_{O_2} \cdot (1 - \eta_d) \quad (13)$$

Average value of the coefficient  $C$  which describes the utilization of 1 cm<sup>3</sup> volume of oxygen can vary from  $C = 18.85$  to 20.95 J/cm<sup>3</sup> depending on the proportion of carbohydrate, protein and fat being oxidized in the diver's organism [3]. The second basic comfort condition [2] enables to determine heat loss by evaporation of sweat secretion. It can be expressed for the hyperbaric environment as follows:

$$\dot{q}_e = \frac{\dot{Q}_e}{A_{Du}} = w \cdot \beta \cdot r \cdot F_{pcl} \cdot (p_s - \varphi \cdot p_{sg}) \quad (14)$$

Area of the nude body surface, i.e. DuBois area, is expressed by the following equation [2]:

$$A_{Du} = 0.203 \cdot m^{0.425} \cdot h^{0.725} \quad (15)$$

Skin wetness is defined [1] as follows:

$$w = \frac{\dot{Q}_e}{\dot{Q}_{e \max}} = 0.02 + 0.4[1 - \exp(-0.01034 \cdot \dot{q}_m + 0.6)] \quad (16)$$

The clothing moisture permeation factor  $F_{pcl}$  describes the „cooling efficiency” of sweating on the surface for a clothed human body [10]. The permeation efficiency factor  $F_{pcl}$  has been derived theoretically for the different kinds of the hyperbaric breathing mixtures [8]:

$$F_{pcl} = \frac{I_{dm}}{I_{dm} + I_{dcl}} = \left( 1 + \frac{0.155 \cdot R_w \cdot T_s \cdot \lambda_a \cdot I_{cla} \cdot \beta}{D_{w-m}} \right)^{-1} \quad (17)$$

By substituting all the terms of heat loss derived in [8], and thermal comfort basic conditions into the heat balance equation (2) the following is obtained:

$$\begin{aligned} & \dot{q}_m (1 - \eta_d) - \frac{0.127 \cdot \beta \cdot r \cdot (p_s - \varphi \cdot p_{sg})}{4.58 + 3.46 \cdot v} + \\ & - 0.8895 \cdot 10^{-11} \cdot \dot{q}_m \cdot r \cdot (p_s - \varphi \cdot p_{sg}) + \\ & - 4.1 \cdot 10^{-9} \cdot \dot{q}_m \cdot c_p \cdot p \cdot R^{-1} \cdot (t_{ex} - t) + \\ & - w \cdot \beta \cdot r \cdot F_{pcl} \cdot (p_s - \varphi \cdot p_{sg}) = \\ & = \frac{\lambda \cdot (t_s - t_{cl})}{4.03 \cdot 10^{-3} \cdot I_{cla}} = \alpha \cdot f_{cl} \cdot (t_{cl} - t) + \\ & + 4 \cdot 10^{-8} \cdot f_{cl} \cdot (T_{cl}^4 - T_r^4) \end{aligned} \quad (18)$$

The comfort equation derived for the hyperbaric environment can be expressed in function of breathing mixture pressure, composition and thermal properties (specific heat, thermal conductivity, viscosity and density), diver's activity, thermal resistance of the clothing, gas temperature, mean radiant temperature, relative humidity and velocity of the breathing mixture, (18).

The comfort equation (18) makes it possible to calculate all combinations of the above specified variables which are responsible for thermal comfort in the hyperbaric chamber. Moreover, it is possible to determine the comfort temperature inside the hyperbaric facility and all terms of the heat dissipated from the human body exposed to the hyperbaric environment. It's worth to accentuate that thermal comfort is felt very individually.

## THE RESULTS

The comfort equation was solved under the following assumptions:

- the depth of simulated diving:  $g = 90, 190, 290, 390, 490, 590$  m;
- the breathing gas: oxygen + helium, (HELIOX), oxygen + hydrogen (HYDROX);
- the relative humidity of the breathing gas:  $\varphi = 0.4, 0.5, 0.6, 0.7, 0.8, 0.9, 1$  at each depth;
- the relative velocity of the breathing gas:  $v = 0.1, 0.15, 0.2, 0.25, 0.3$  m/s;

- the mean radiant temperature:  $t_r = 0, 10, 20, 30, 40, 50$  °C;
- the Du Bois area:  $A_{Du} = 1.8$  m<sup>2</sup>;
- the diver was clothed in a clothing of the total heat transfer resistance from skin to the outer surface of  $I_{cla} = 0.2 \div 1.1$  clo, clothing area factor  $f_{cl} = 0, 8, 1$  clo =  $0.155$  m<sup>2</sup>K/W;
- the activity levels: the sedentary activity  $\dot{q}_m = 58$  W/m<sup>2</sup>, medium work activity  $\dot{q}_m = 90$  W/m<sup>2</sup>, intensive work activity  $\dot{q}_m = 120$  W/m<sup>2</sup>.

The comfort equation has been solved for relevant combinations of the above specified variables and the results have been presented in the form of the diagrams. The curves in Fig. 5 and Fig. 6 (gas pressure versus comfort temperature with gas velocity as a parameter) represent the comfort lines i.e. lines drawn through points which satisfy the equation (17) and thus provide the thermal comfort in HELIOX and HYDROX breathing mixtures under the following assumptions: the relative humidity of breathing gas  $\varphi = 0.7$ , sedentary activity level  $\dot{q}_m = 58$  W/m<sup>2</sup>, clothing thermal resistance  $I_{cla} = 0.37$  clo, mean radiant temperature  $I_{cla} = 0.37$ .

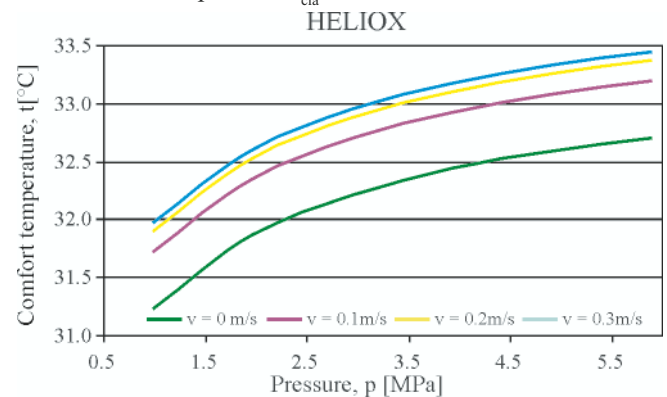


Fig. 5. Comfort lines for HELIOX (pressure versus comfort temperature with parameter of relative gas velocity) under the following assumptions:  $\dot{q}_m = 58$  W/m<sup>2</sup>,  $I_{cla} = 0.37$  clo,  $\varphi = 0.4$ ,  $t_r = 30$  °C

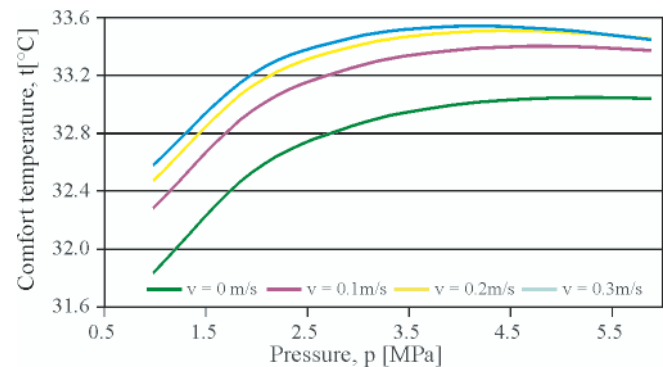
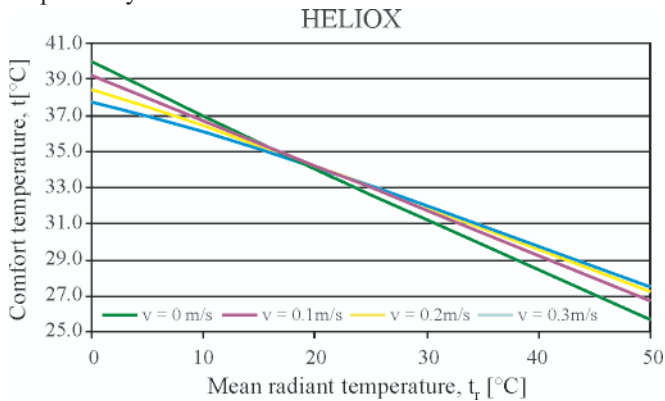


Fig. 6. Comfort lines for HYDROX (pressure versus comfort temperature with relative gas velocity as a parameter) under the following assumptions:  $\dot{q}_m = 58$  W/m<sup>2</sup>,  $I_{cla} = 0.37$  clo,  $\varphi = 0.4$ ,  $t_r = 30$  °C

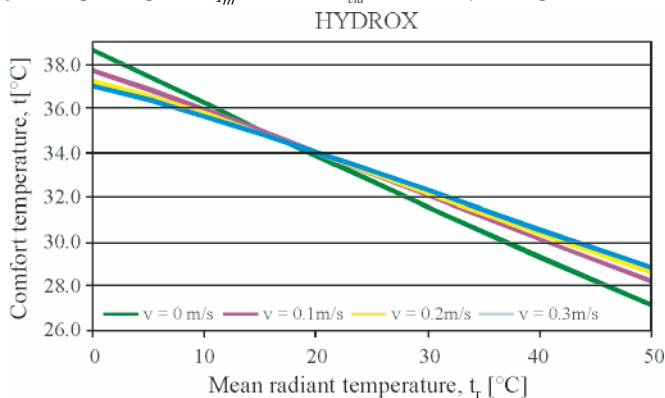
From Fig. 5 and Fig. 6 it is evident that the total pressure of the breathing gas exerts a large effect on thermal comfort. To compensate body heat losses and achieve thermal comfort within the gas pressure range of  $p = 0.98 \div 5.88$  MPa and gas relative velocity range of  $v = 0 \div 0.3$  m/s it is necessary to increase the comfort temperature by  $\Delta t \approx 2.2$  K. As it follows from calculations despite pressure range, at  $p = \text{const}$  the increase of relative gas velocity from  $v = 0$  to  $v = 0.3$  m/s should be compensated for by the comfort temperature increase of  $\Delta t \approx 0.7$  K.

Fig. 7 and Fig. 8 show comfort lines which illustrate the relationship between comfort temperature in HELIOX and HYDROX atmospheres, mean radiant temperature and relative

gas velocity under the following assumptions:  $\dot{q}_m = 58 \text{ W/m}^2$ ,  $I_{cla} = 0.37 \text{ clo}$ ,  $\phi = 0.7$ ,  $t_r = 30 \text{ }^\circ\text{C}$ ,  $p = 0.98 \text{ MPa}$ . As it follows from Fig. 7 and Fig. 8 at constant relative gas velocity increase of mean radiant temperature should be compensated by comfort temperature decrease. As seen from Fig. 7 and Fig. 8, the comfort lines cross each other at the mean radiant temperature  $t_r = 20 \text{ }^\circ\text{C}$  and comfort temperature  $t = 34.1 \text{ }^\circ\text{C}$  for HELIOX, and  $t_r = 20 \text{ }^\circ\text{C}$  and  $t = 34 \text{ }^\circ\text{C}$  for HYDROX, respectively.



**Fig. 7.** Comfort lines for HELIOX (mean radiant temperature versus comfort temperature with relative gas velocity as a parameter) under the following assumptions:  $\dot{q}_m = 58 \text{ W/m}^2$ ,  $I_{cla} = 0.37 \text{ clo}$ ,  $\phi = 0.7$ ,  $p = 0.98 \text{ MPa}$



**Fig. 8.** Comfort lines for HYDROX (mean radiant temperature versus comfort temperature with gas velocity as parameter) at the following assumptions:  $\dot{q}_m = 58 \text{ W/m}^2$ ,  $I_{cla} = 0.37 \text{ clo}$ ,  $\phi = 0.7$ ,  $p = 0.98 \text{ MPa}$

The comfort lines cross each other where the temperature of the breathing mixture is equal to the mean temperature of the clothed body since the convective heat transfer here will be zero, independent of the relative velocity. To the right of the crossing point the temperature of the outer surface of the clothing is higher than the breathing mixture temperature and an increase in the relative velocity will therefore require an increase of the breathing mixture temperature or changing mean radiant temperature in order to maintain thermal comfort. To the left of the crossing point the temperature of the outer surface of the clothing is lower than the breathing mixture temperature and an increase in gas velocity will therefore require a decrease in the mixture temperature or changing mean radiant temperature to maintain thermal comfort.

Fig. 9 and Fig. 10 show comfort lines for HELIOX and HYDROX, which illustrate the relationship between comfort temperature, pressure and the total heat transfer resistance of clothing under the following assumptions:  $\dot{q}_m = 58 \text{ W/m}^2$ ,  $\phi = 0.4$ ,  $t_r = 25 \text{ }^\circ\text{C}$ ,  $v = 0 \text{ m/s}$ .

From Fig. 9 and Fig. 10 it is evident that for all types of the total heat transfer resistance of clothing increase of gas pressure should be compensated for by increase of comfort temperature. As it follows from Fig. 9 and Fig. 10 at  $I_{cla} = \text{const}$ ,

increase of pressure from  $p = 0.98 \text{ MPa}$  to  $p = 5.88 \text{ MPa}$  should be compensated for by increase of comfort temperature by  $\Delta t = 0.7 \text{ K}$  for HELIOX and by  $\Delta t = 0.6 \text{ K}$  for HYDROX. To maintain thermal comfort in HELIOX atmosphere of pressure  $p = 2.94 \text{ MPa}$  and in HYDROX atmosphere of pressure  $p = 1.96 \text{ MPa}$  increase of the total heat transfer resistance of clothing from  $I_{cla} = 0.3 \text{ clo}$  (light clothing ensemble) to  $I_{cla} = 1.1 \text{ clo}$  (heavy working ensemble) should be compensated for by decrease of comfort temperature of  $\Delta t = 1.3 \text{ K}$  for HELIOX and of  $\Delta t = 0.8 \text{ K}$  for HYDROX.

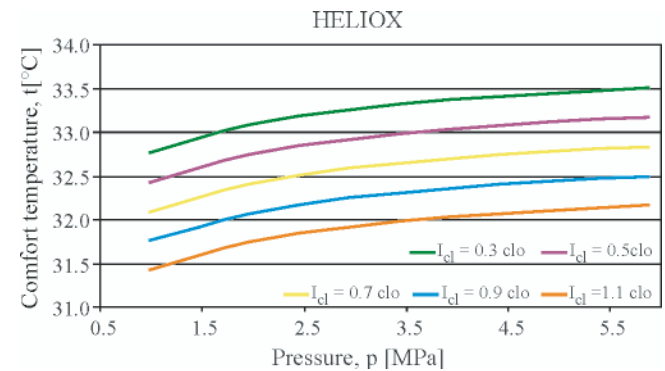


**Fig. 9.** Comfort lines for HELIOX (pressure versus comfort temperature with the total heat transfer resistance of clothing as a parameter) under the following assumptions:  $\dot{q}_m = 58 \text{ W/m}^2$ ,  $\phi = 0.4$ ,  $t_r = 25 \text{ }^\circ\text{C}$ ,  $v = 0 \text{ m/s}$

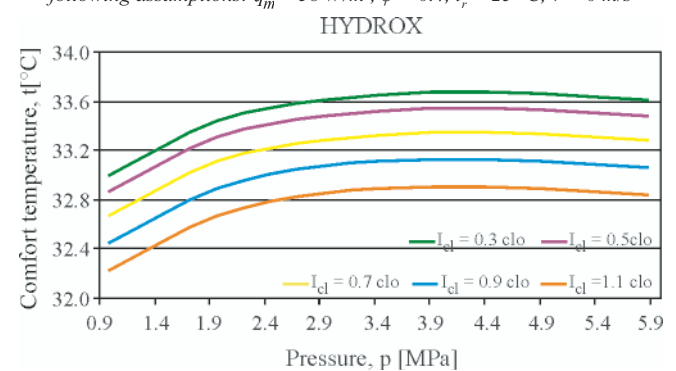


**Fig. 10.** Comfort lines for HYDROX (pressure versus comfort temperature with the total heat transfer resistance of clothing as a parameter) under the following assumptions:  $\dot{q}_m = 58 \text{ W/m}^2$ ,  $\phi = 0.4$ ,  $t_r = 25 \text{ }^\circ\text{C}$ ,  $v = 0 \text{ m/s}$

Fig. 11 and Fig. 12 show the relationship between comfort temperature, pressure and the diver's activity in HELIOX and HYDROX atmosphere under the following assumptions:  $\phi = 0.6$ ,  $t_r = 30 \text{ }^\circ\text{C}$ ,  $v = 0 \text{ m/s}$ ,  $I_{cla} = 0.2 \text{ clo}$ . It is evident from Fig. 11 and Fig. 12 that at the constant activity of the diver, comfort temperature increases due to increase of pressure. To maintain thermal comfort at  $p = \text{const}$  and increasing activity of the diver it is necessary to reduce comfort temperature.

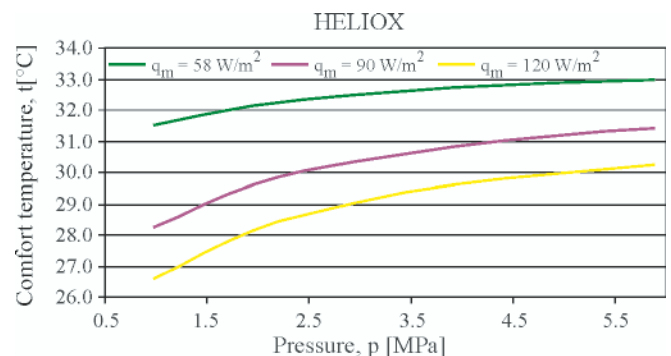


**Fig. 11.** Comfort lines for HELIOX (pressure versus comfort temperature with the diver activity as a parameter) under the following assumptions:  $I_{cla} = 0.2 \text{ clo}$ ,  $\phi = 0.6$ ,  $t_r = 30 \text{ }^\circ\text{C}$ ,  $v = 0 \text{ m/s}$

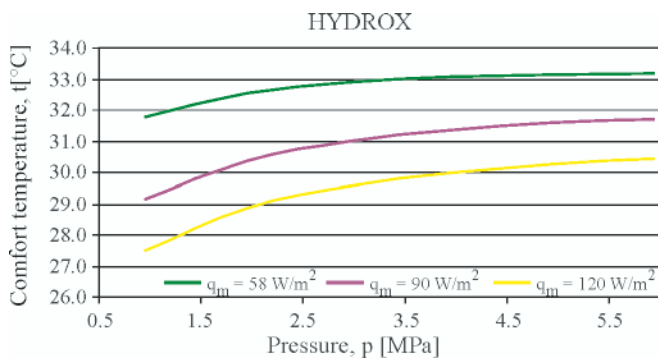


**Fig. 12.** Comfort lines for HYDROX (pressure versus comfort temperature with the diver activity as a parameter) under the following assumptions:  $I_{cla} = 0.2$  clo,  $\phi = 0.6$ ,  $t_r = 30$  °C,  $v = 0$  m/s

As it follows from Fig. 11 and Fig. 12 to maintain thermal comfort at the pressure  $p = 0.981$  MPa, change in the diver's activity from  $\dot{q}_m = 58$  W/m<sup>2</sup> (sedentary) to  $\dot{q}_m = 120$  W/m<sup>2</sup> (intensive work) should be compensated for by the comfort temperature decrease  $\Delta t = 4.9$  K in the case of HELIOX, and  $\Delta t = 3.0$  K in the case of HYDROX. At the diver's sedentary activity  $\dot{q}_m = 58$  W/m<sup>2</sup> the pressure increase from  $p = 0.98$  MPa to  $p = 5.88$  MPa should be compensated for by the comfort temperature increase  $\Delta t = 1.5$  K both for HELIOX and HYDROX.

Fig. 13 and Fig. 14 show comfort lines for HELIOX and HYDROX under the following assumptions:  $I_{cla} = 0.37$  clo,  $\phi = 0.6$ ,  $t_r = 30$  °C,  $p = 1.96$  MPa. As it follows from Fig. 13 and Fig. 14 at constant activity an increase of relative gas velocity should be compensated for by an increase of comfort temperature. At  $v = \text{const}$  an increase of diver's activity should be compensated for by a decrease of comfort temperature.

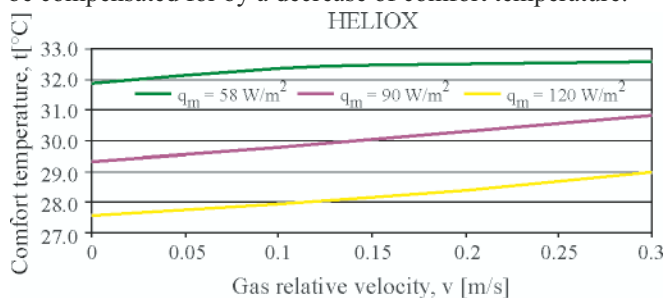


**Fig. 13.** Comfort lines for HELIOX (gas velocity versus comfort temperature with the diver activity as a parameter) under the following assumptions:  $I_{cla} = 0.37$  clo,  $\phi = 0.6$ ,  $t_r = 30$  °C,  $p = 1.96$  MPa

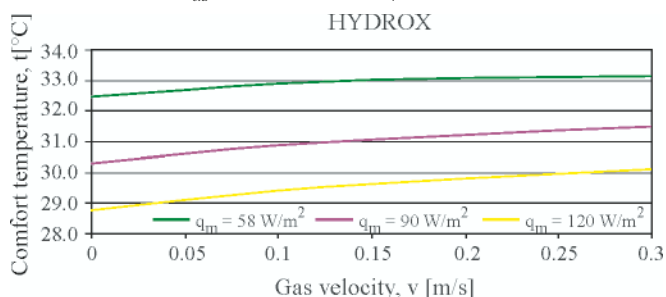


**Fig. 14.** Comfort lines for HYDROX (relative gas velocity versus comfort temperature with the diver activity as a parameter) under the following assumptions:  $I_{cla} = 0.37$  clo,  $\phi = 0.6$ ,  $t_r = 30$  °C,  $p = 1.96$  MPa

As seen from Fig. 13 and Fig. 14, to maintain the sedentary diver ( $\dot{q}_m = 58$  W/m<sup>2</sup>) and working diver ( $\dot{q}_m = 120$  W/m<sup>2</sup>) in thermal comfort, when relative gas velocity changes from  $v = 0$  to  $v = 0.3$  m/s, it is necessary to increase comfort temperature by  $\Delta t = 0.7$  K for HELIOX and  $\Delta t = 3.5$  K for HYDROX. As shown in Fig. 13 and Fig. 14 the change in the diver's activity

from  $\dot{q}_m = 58$  W/m<sup>2</sup> to  $\dot{q}_m = 120$  W/m<sup>2</sup>, at constant relative gas velocity of  $v = 0.1$  m/s, should be compensated for by the temperature decrease  $\Delta t = 4.4$  K for HELIOX and  $\Delta t = 3.5$  K for HYDROX.

Fig. 15 shows the relationship between comfort temperature, pressure and relative humidity of HYDROX under the following assumptions:  $\dot{q}_m = 58$  W/m<sup>2</sup>,  $I_{cla} = 0.37$  clo,  $v = 0$  m/s, mean radiant temperature  $t_r = 25$  °C.

As it follows from Fig. 15 at constant gas relative humidity an increase in pressure will increase comfort temperature. At the pressure  $p = 0.98$  MPa a change in HYDROX relative humidity from  $\phi = 0.4$  to  $\phi = 1$  should be compensated for by the comfort temperature decrease  $\Delta t = 0.6$  K.

At higher pressure of breathing mixture comfort lines are convergent and asymptotically approach the comfort temperature  $t = 33.6$  °C. It means that there is no significant influence of breathing mixture relative humidity on comfort temperature. As it follows from the obtained results the influence of the breathing gas relative humidity on the magnitude of comfort temperature is not significant however very important for sweat evaporation and comfort sensation. Poor evaporative rate may result in a diver's feeling of high humidity (discomfort) and will prevent from evaporative cooling of the skin.

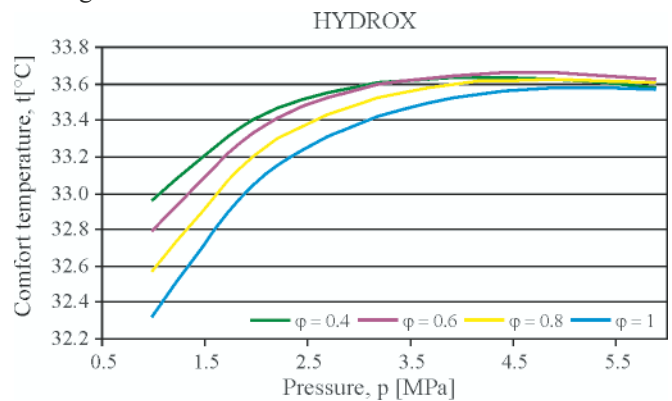


**Fig. 15.** Comfort lines for Hydrox (gas pressure versus comfort temperature with the relative humidity as a parameter) under the following assumptions:  $\dot{q}_m = 58$  W/m<sup>2</sup>,  $I_{cla} = 0.37$  clo,  $v = 0$  m/s,  $t_r = 25$  °C,  $p = 0.98$  MPa.

By using the comfort equation it is possible, for any type of the breathing mixture (composition, pressure), type of clothing and type of the diver's activity, to calculate all reasonable combinations of the temperature, relative humidity and velocity of the breathing gas and mean radiant temperature. The water vapour transport coefficient in the hyperbaric environment can be computed from the experimental relationship for vapour transport coefficient in helium-oxygen mixture [4,5] or theoretically [8]. The results of the experiments demonstrated a great influence of the total pressure on the water vapour transport coefficient in the helium rich atmosphere. To make an assessment of the thermal comfort equation derived for the hyperbaric facility, its theoretical and an experimental verification is recommended. Fig. 16 shows comparison between the theoretical results obtained from the thermal comfort equation and the experimental results published in [12, 16, 18].

The theoretical solution of the thermal comfort equation, shown in Fig. 16, was obtained under the following assumptions:  $\dot{q}_m = 58$  W/m<sup>2</sup>,  $I_{cla} = 0.37$  clo,  $v = 0$  m/s,  $\phi = 0.4$ ,  $t_r = 30$  °C. As it follows from Fig. 16 the theoretical results are in compliance with those previously published in [16] for HELIOX, and are higher approximately by  $\Delta t = 2$  K than the temperature predicted in [12, 13, 19]. Comparison of the results is difficult.

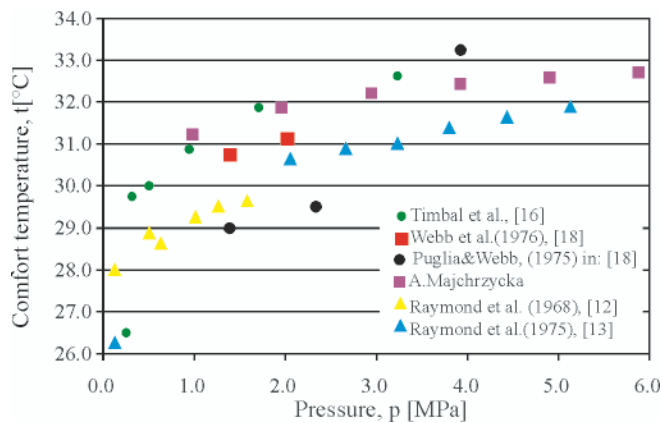


Fig. 16. Comparison between the theoretical results obtained from the thermal comfort equation and the experimental results published in [12, 16, 18]

After experimental verification, the mathematical model of thermal comfort can serve as a very useful mathematical tool in designing the environmental life support systems of the hyperbaric facilities. The derived thermal comfort equation enables to simulate different thermal conditions in the hyperbaric facility with taking into account the most important variables which influence thermal comfort.

## CONCLUSIONS

- On the basis of the mathematical model of human body thermal exchange and two basic thermal comfort conditions, the comfort equation for hyperbaric environment was derived
- The comfort equation enables to calculate all those combinations of environmental variables which would create thermal comfort in the hyperbaric facility,
- By using the comfort equation it is possible, for any type of the breathing mixture (composition, pressure), type of clothing and the diver's activity, to calculate all reasonable combinations of the gas temperature, relative humidity and velocity and mean radiant temperature,
- The comfort equation was solved for the hyperbaric breathing mixtures: HELIOX and HYDROX in the assumed range of the parameters in diving up to the depth of  $g = 590$  m,
- As follows from the solution of the comfort equation, the required comfort temperature in the hyperbaric facilities increases progressively along with increasing pressure of HELIOX and HYDROX breathing mixtures, and the comfort temperatures are similar in values for both atmospheres,  
The results obtained under the assumptions:  $\dot{q}_m = 58$  W/m<sup>2</sup>,  $I_{cla} = 0.37$  clo,  $v = 0$  m/s,  $\phi = 0.4$ ,  $t_r = 30$  °C for the pressure range of  $p = 0.98 \div 5.88$  MPa, have shown the comfort temperature range of  $t = 31.6 \div 33.6$  °C to be nearly the same for HELIOX and HYDROX.
- The theoretical results found for HELIOX are comparable with those previously experimentally determined and reported in [12, 13, 16, 18]. There are no available data concerning the relationship between comfort temperature and pressure in H<sub>2</sub>-O<sub>2</sub> mixture.
- The presented paper has concluded the first stage of the research aimed at mathematical modelling of thermal comfort in hyperbaric facility, and the second stage should be aimed at experimental verification of the derived model,
- After experimental verification, the mathematical model of thermal comfort can serve as a very useful mathematical

tool in designing and operating the environmental life support systems of hyperbaric facilities, as it enables to simulate different thermal conditions in the hyperbaric facility.

## NOMENCLATURE

$A_{Du}$	– Du Bois area, human body surface area, [m <sup>2</sup> ],
$c_p$	– specific heat of the breathing mixture, [J/kg K],
$D_{w-m}$	– diffusion coefficient of water vapour into breathing mixture, [m <sup>2</sup> /s],
$f_{cl}$	– ratio of the surface area of the clothed body and the surface area of the nude body,
$F_{pcl}$	– moisture permeation factor,
$I_{cla}$	– thermal resistance to heat transfer from skin to outer surface of the clothed body, [clo],
$I_{del}$	– diffusive resistance for water vapour through the clothing, [m <sup>2</sup> sPa/kg],
$I_{dm}$	– diffusive resistance for water vapour through the breathing mixture, [m <sup>2</sup> sPa/kg],
$N$	– external power, [N],
$p$	– total pressure of the breathing mixture, [Pa],
$p_s, p_{sg}$	– saturated water vapour pressure at skin (surface) temperature and ambient breathing gas temperature, [Pa], respectively
$\dot{q}_m$	– diver's activity level, metabolic rate, [W/m <sup>2</sup> ],
$\dot{Q}$	– flux of internal heat produced by the body, [W],
$\dot{Q}_d$	– flux of heat loss resulting from water vapour diffusion through the skin, [W],
$\dot{Q}_e$	– flux of evaporative heat loss, [W],
$\dot{Q}_{ecl}$	– flux of heat loss resulting from sweat evaporation from the skin, [W],
$\dot{Q}_{e\max}$	– flux of evaporative heat loss at skin wetness $w = 1$ ,
$\dot{Q}_m$	– flux of metabolic heat released in oxidation processes, [W],
$\dot{Q}_o$	– flux of respiration heat loss, [W],
$\dot{Q}_{oj}$	– flux of dry respiration heat loss, [W]
$\dot{Q}_{ou}$	– flux of latent respiration heat loss, [W]
$\dot{Q}_k$	– flux of convective heat dissipated from the outer surface of the clothed body, [W],
$\dot{Q}_o$	– flux of heat loss from the skin to the outer surface of the clothed body, [W],
$\dot{Q}_r$	– flux of heat loss resulting from radiation from the outer surface of the clothed body, [W],
$r$	– specific latent heat of vaporisation, [J/kg],
$R, R_w$	– gas constant of the breathing mixture, water, [J/kg K],
$t$	– comfort temperature, [°C],
$t_{cl}, T_{cl}$	– temperature of the outer surface of the clothing, [°C, K],
$t_{ex}$	– temperature of expired gas, [°C]
$t_r, T_r$	– mean radiant temperature, [°C, K],
$t_s, T_s$	– temperature of the skin surface, [°C, K],
$w$	– skin wetness,
$v$	– relative velocity of the breathing mixture, [m/s],
$\dot{V}_{O_2}$	– oxygen consumption, [cm <sup>3</sup> /min],
$x_i$	– molar fraction of breathing gas component,
$\alpha$	– convective heat transfer coefficient, [W/m <sup>2</sup> K]
$\beta$	– water vapour transport coefficient in the hyperbaric environment, [kg/m <sup>2</sup> sPa],
$\phi$	– relative humidity of the breathing mixture,
$\lambda, \lambda_a$	– thermal conductivity of the breathing mixture and atmospheric air, [W/mK], respectively,
$\eta$	– viscosity of the breathing mixture, [kg/ms]
$\eta_d$	– mechanical efficiency of diver.

## BIBLIOGRAPHY

1. Azer N.Z., S.Hsu: *The use of modelling human response in the analysis of thermal comfort of indoor environments*. Proceedings of a Symposium Held at the National Bureau of Standards Gaithersburg, Maryland, February 1977.
2. Fanger P.O.: *Thermal comfort*. Danish Technical Press, Copenhagen, 1970.

3. Lynn E. T., Vorosmarti J. Jr, Modell H. I.: *Research Report 21-73*, Navy Experimental Diving Unit, Washington, 1974
4. Gardette B., Gortan C., Delauze H.G.: *Helium in-hydrogen out. A new diving technique*. Proceedings of the 23<sup>rd</sup> Annual Scientific Meeting of the European Underwater and Baromedical Society, Bled (Slovenia), 1997.
5. Hamilton R.W. Jr.: *Breathing mixtures*. Technical Memorandum CRL-T-750, Ocean Systems and Development Laboratory, Tarrytown, New York, December 1973.
6. Kozak T, Majchrzycka A.: *The influence of pressure, temperature and kind of gas on the coefficient of water evaporation from the free surface*. Boiling and Condensation International Proceedings, Riga, 1998.
7. Kozak T., Majchrzycka A.: *The influence of pressure and temperature on rate of water evaporation from the free surface*. Advances in Engineering Heat Transfer. Proc. of Second Baltic Heat Transfer Conference, Ed. B.Sunden, E. Blums, A. Žukauskas, Computational Mechanics Publications, Southampton, Boston, 1995.
8. Majchrzycka A.: *The comfort temperature in the hyperbaric environment* (in Polish). Doctoral thesis, Technical University of Szczecin, Szczecin, 1982.
9. Moor T. O., Morlock J. F., Lally D. A., Hong S. K.: *Thermal cost of saturation diving: respiratory and whole body heat loss at 16.1 ATA*. Proc. of the Third Symposium on Underwater Physiology, Freeport, Bahamas, 1972.
10. Nishi Y., Gagge A.P.: *Moisture Permeation of Clothing - A Factor governing Thermal Equilibrium and Comfort*. ASHRAE Transactions, vol.76,1,1970.
11. Raymond L.: *Temperature problems in multiday exposures to high pressures in the sea. Thermal balance in hyperbaric atmospheres*. Proc. of the Third Symposium on Underwater Physiology, Baltimore, 1966.
12. Raymond L.W., Bell W.H. 2nd, Bondi K.R., Lindberg C.R.: *Body temperature and metabolism in hyperbaric helium atmospheres*. J. Appl. Physiol., 1968, May 24(5).
13. Raymond LW, Thalmann E, Lindgren G, Langworthy HC, Spaur WH, Crothers J, Braithwaite, W, Berghage T.: *Thermal homeostasis of resting man in helium-oxygen at 1-50 atmospheres absolute*, in: Undersea Biomed. Res., 1975, March 2(1).
14. Taylor L.: *Diving with gas mixes other than air: Mixed gas diving*, ed. Watersport, <http://www-personal.umich.edu/~lpt/mixhistory.htm>,
15. Shilling C. W., Werts M. F., Schandelmeier N. R., Ed.: *The underwater handbook: A guide to physiology and performance for the engineer*. Plenum Press, New York, 1976.
16. Timbal J., Varène P., Vieillefond H., Guenard H., L'Huillier J.: *Metabolism and heat losses of resting man in hyperbaric helium atmosphere*. Journal of Applied Physiology, 36, 4, 1974.
17. Varenne P., Timbal J., Vieillefond H., Guenard H., L'Huillier J.: *Energy balance of man in simulated dive from 1.5 to 31 ATA*. Proc. of the Third Symposium on Underwater Physiology, Freeport, Bahamas, 1972.
18. Webb P., Troutman S.J.Jr., Fratalli V., Dwyer J., Moore T.O., Morlock J.F., Smith R.M., Ohta Y.: *Energy balance in saturation diving*. Report ADA041834 Naval Medicine Research and Development Command, Bethesda, Maryland, 1976.
19. Webb P.: *Body heat loss in undersea gaseous environments*. Aerospace Medicine, 10, 1970.
20. Webb P.: *The thermal drain of comfortable hyperbaric environments*. Naval Research Review, 3, 1973.

---

#### CONTACT WITH THE AUTHOR

Anna Majchrzycka, Ph. D.  
 Faculty of Mechanical Engineering and Mechatronics,  
 Department of Heat Engineering,  
 West Pomeranian University of Technology  
 Al. Piastów 19  
 71-310 Szczecin, POLAND  
 e-mail: [anna.majchrzycka@zut.edu.pl](mailto:anna.majchrzycka@zut.edu.pl)



The Ship Handling Research and Training Centre at Ilawa is owned by the Foundation for Safety of Navigation and Environment Protection, which is a joint venture between the Gdynia Maritime University, the Gdansk University of Technology and the City of Ilawa.

**Two main fields of activity of the Foundation are:**

- Training on ship handling. Since 1980 more than 2500 ship masters and pilots from 35 countries were trained at Ilawa Centre. The Foundation for Safety of Navigation and Environment Protection, being non-profit organisation is reinvesting all spare funds in new facilities and each year to the existing facilities new models and new training areas were added. Existing training models each year are also modernised, that's why at present the Centre represents a modern facility perfectly capable to perform training on ship handling of shipmasters, pilots and tug masters.
- Research on ship's manoeuvrability. Many experimental and theoretical research programmes covering different problems of manoeuvrability (including human effect, harbour and waterway design) are successfully realised at the Centre.

The Foundation possesses ISO 9001 quality certificate.

**Why training on ship handling?**

The safe handling of ships depends on many factors - on ship's manoeuvring characteristics, human factor (operator experience and skill, his behaviour in stressed situation, etc.), actual environmental conditions, and degree of water area restriction.

Results of analysis of CRG (collisions, rammings and groundings) casualties show that in one third of all the human error is involved, and the same amount of CRG casualties is attributed to the poor controllability of ships. Training on ship handling is largely recommended by IMO as one of the most effective method for improving the safety at sea. The goal of the above training is to gain theoretical and practical knowledge on ship handling in a wide number of different situations met in practice at sea.

For further information please contact:

**The Foundation for Safety of Navigation and Environment Protection**

Head office:  
36, Chrzanowskiego Street  
80-278 GDAŃSK, POLAND  
tel./fax: +48 (0) 58 341 59 19

Ship Handling Centre:  
14-200 ILAWA-KAMIONKA, POLAND  
tel./fax: +48 (0) 89 648 74 90  
e-mail: office@ilawashiphandling.com.pl  
e-mail: office@portilawa.com

## GDANSK UNIVERSITY OF TECHNOLOGY

is the oldest and largest scientific and technological academic institution in the Pomeranian region. The history of Gdansk University of Technology is marked by two basic dates, namely: October 6, 1904 and May 24, 1945.

The first date is connected with the beginning of the technical education at academic level in Gdansk. The second date is connected with establishing of Gdansk University of Technology, Polish state academic university. Gdansk University of Technology employ 2,500 staff, 1,200 whom are academics. The number of students approximates 20,000, most of them studying full-time. Their career choices vary from Architecture to Business and Management, from Mathematics and Computer Science to Biotechnology and Environmental Engineering, from Applied Chemistry to Geodesics and Transport, from Ocean Engineering to Mechanical Engineering and Ship Technology, from Civil Engineering to Telecommunication, Electrical and Control Engineering. Their life goals, however, are much the same - to meet the challenge of the changing world. The educational opportunities offered by our faculties are much wider than those of other Polish Technical universities, and the scientific research areas include all of 21st Century technology. We are one of the best schools in Poland and one of the best known schools in Europe – one that educates specialists excelling in the programming technology and computer methods used in solving complicated scientific, engineering, organizational and economic problems.

### THE FACULTY OF OCEAN ENGINEERING AND SHIP TECHNOLOGY

The Faculty of Ocean Engineering and Ship Technology (FOEST) as the only faculty in Poland since the beginning of 1945 has continuously been educating engineers and doctors in the field of Naval Architecture and Marine Technology.

The educational and training activities of FOEST are supported by cooperation with Polish and foreign universities, membership in different international organizations and associations, as well as participation in scientific conferences and symposia. Hosting young scientists and students from different countries is also a usual practice in FOEST.

The activities of Faculty departments are related to: mechanics and strength of structures, hydromechanics, manufacturing, materials and system quality, power plants, equipment and systems of automatic control, mostly in shipbuilding, marine engineering and energetic systems.

FOEST is a member of such organizations like WEGEMT; The Association of Polish Maritime Industries and the co-operation between Nordic Maritime Universities and Det Norske Veritas. The intensive teaching is complemented and supported by extensive research activities, the core of which is performed in close collaboration between FOEST staff and industry. We take great care to ensure that the applied research meet both the long term and short term needs of Polish maritime industry. FOEST collaborates with almost all Polish shipyards. Close links are maintained with other research organizations and research institutions supporting the Polish maritime industry, such as Ship Design and Research Centre and Polish Register of Shipping, where several members of the Faculty are also members of the Technical Board.

The Faculty of Ocean Engineering and Ship Technology is a unique academic structure, which possesses numerous highly qualified and experienced staff in all above mentioned specific research areas. Moreover, the staff is used to effective co-operation and exchange of ideas between specialists of different detailed areas. This enables a more integrated and comprehensive treatment of research and practical problems encountered in such a complicated field of activity as naval architecture, shipbuilding and marine engineering.

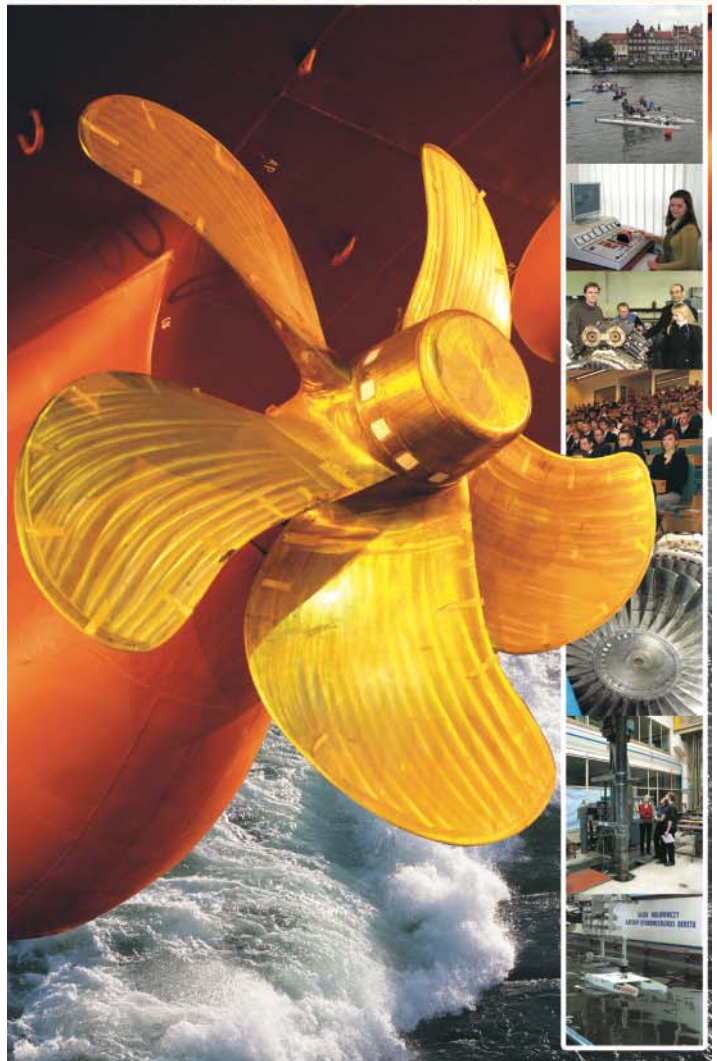
The staff of the Faculty has strong international links worldwide, being members or cooperating with international organizations like International Maritime Organization IMO, International Towing Tank Conference ITTC, International Ship and Offshore Structures Congress ISSC, International Conference on Practical Design of Ship and other floating Structures PRADS just to name a few.

GDANSK UNIVERSITY OF TECHNOLOGY  
Faculty of Ocean Engineering and Ship Technology  
11/12 Narutowicza Street, 80-952 Gdansk, Poland  
Tel (+48) 58 347 1548 ; Fax (+48) 58 341 4712  
e-mail: sekoce@pg.gda.pl



**Gdansk University  
of Technology**

**Faculty of Ocean  
Engineering  
and Ship Technology**



[www.oce.pg.gda.pl](http://www.oce.pg.gda.pl)